

Sub-Micron Indium Pillar Fabrications

by

Pantea Pervissian

A thesis
presented to the University of Waterloo
in fulfillment of the
thesis requirement for the degree of
Master of Applied Science
in
Chemical Engineering

Waterloo, Ontario, Canada, 2009

© Pantea Pervissian 2009

Author's Declaration

I hereby declare that I am the sole author of this thesis. This is a true copy of the thesis, including any required final revisions, as accepted by my examiners.

I understand that my thesis may be made electronically available to the public.

Pantea Pervissian

Abstract

The laws of classical mechanics show that mechanical properties are independent of sample sizes. However, based on extensive theoretical work and experimentation, it is believed that reducing the size of materials to the submicron scale can result in different mechanical properties than those found in bulk quantities. This size effect was explained by the strain gradient. Atomic simulations have shown that yield stress depends on size even in the absence of the strain gradient. All of the experiments done on material creep behaviour, reported in the literature, have been conducted in the presence of strain gradient.

This thesis focuses on the fabrication methods of freestanding indium pillar samples created by two unique methods; focused ion beam (FIB) and the micro-fabrication approach. The low melting point indium metal limits the application of FIB to form the sub-micron pillars. As a result, two different micro-lithography techniques, ultra-violet radiation and electron-beam lithography, were developed to fabricate these nano-pillars. In order to monitor the creep mechanism, which was dominant in this testing, the samples were then divided into two groups: polycrystalline and single-crystal pillars, each in different sizes. These pillars will later be compressed by a nano-indenter using a flat punch. Compressive stress, strain, and stiffness of the pillars will be measured to verify if the indium mechanical behavior deviates from the bulk in the absence of strong strain gradient.

Acknowledgements

I would like to express my sincere gratitude to my supervisor, Dr. Ting Y. Tsui, for the opportunity that he has given me and for his guidance, inspiration, and insight throughout this work and my studies.

I would also like to thank Arash Tajik for his invaluable suggestions throughout this work and also Gyuhyon Lee for his endless help through the experiments. I am just as grateful to Dr. Todd Simpson of the Nanofabrication Laboratory of the University of Western Ontario. His knowledge and insight in this work is appreciable.

Special thanks are due to Dr. Mark Pritzker for lending us his lab to perform our experiments and also to Jorge Vazquez for his patience during our time in the lab.

Above all, I am grateful to my parents and my sister for their endless love and continuous support in every single moment of my life.

Table of Contents

List of Tables.....	viii
List of Figures.....	ix
List of Symbols.....	xii
List of Glossary.....	xv
Chapter 1 Introduction.....	1
1.1 Theory.....	1
1.1.1 Material Strength.....	1
1.1.2 Elastic-Plastic Behaviour.....	1
1.1.3 Average Stress–Strain.....	2
1.1.4 Types of Stress-Strain.....	3
1.1.5 Tensile Deformation in Ductile Metals.....	3
1.1.6 Mechanical Failure.....	5
1.1.6.1 Excessive Elastic Deformation.....	5
1.1.6.2 Yielding.....	5
1.1.6.3 Fracture.....	5
1.1.7 Plastic Deformation of Single Crystals.....	6
1.1.8 Crystal Geometry Concepts.....	6
1.1.9 Lattice Defect.....	9
1.1.9.1 Point Defect.....	9
1.1.9.2 Dislocation.....	9
1.1.9.2.1 Burger Vector.....	10
1.1.9.2.2 Dislocation Line.....	10
1.1.9.2.3 Edge Dislocation.....	10
1.1.9.2.4 Screw Dislocation.....	11
1.1.10 Creep.....	11
1.1.10.1 Creep Curve.....	12
1.1.10.2 Types of Creep.....	13
1.1.10.2.1 Nabarro-Herring Creep.....	14
1.1.10.2.2 Coble Creep.....	14

1.1.10.2.3 Creep Activation Energy	14
1.2 Motivation of Size-Dependent Creep Behaviour of Materials.....	16
1.2.1 Indium Creep Behaviour	18
1.2.2 Indium	18
1.2.3 Indentation Size Effect.....	21
1.3 Objective of the Work.....	22
Chapter 2 Sample Design.....	23
2.1 Introduction.....	23
2.2 Sample Design	23
2.3 Fabrication Techniques	25
2.3.1 Focus Ion Beam Instrument	26
2.3.1.1 The Stage	28
2.3.1.2 Imaging Detector.....	29
2.3.1.3 Gas Injectors	29
2.3.2 Microlithography	30
2.3.2.1 Micro- Mold Fabrication.....	31
2.3.2.1.1 Micro-Mold Chips Design	31
2.3.2.1.2 Micro-Mold Fabrication Process.....	33
2.3.2.2 Electro-Depositing	34
2.3.2.2.1 Principal of Electroplating Process	35
2.3.2.2.2 Current Density	36
2.3.2.3 Revealing the Pillars	37
Chapter 3 Sample Fabrication.....	39
3.1 Introduction.....	39
3.2 Sample Fabrication	39
3.2.1 Sample Fabrication using the Focused Ion Beam (FIB)	40
3.2.2 Focus Ion Beam Fabrication Results.....	41
3.2.3 Sample Fabrication using Microlithography.....	45
3.2.3.1 Substrate.....	45
3.2.3.2 Gold & Chromium Deposition.....	46
3.2.3.2.1 E-beam Evaporation Deposition	47

3.2.3.3 Types of Microlithography	49
3.2.3.3.1 Ultraviolet Lithography.....	50
3.2.3.3.1.1 Spin Coating SU-8	52
3.2.3.3.1.2 SU-8 Soft Bake	53
3.2.3.3.1.3 Chromium Photo Mask	53
3.2.3.3.1.4 Ultraviolet Exposure on SU-8 Resist	56
3.2.3.3.1.5 SU-8 Post-exposure Baking	57
3.2.3.3.1.6 Developing SU-8.....	58
3.2.3.3.2 E-beam Lithography	60
3.2.3.3.2.1 Emulsion Photo Mask	63
3.2.3.3.2.2 Coating Gold Chips AZ Photo Resist	67
3.2.3.3.2.3 Oxygen Plasma Etch	70
3.2.3.3.2.4 PMMA Photo Resist Coating.....	70
3.2.3.3.2.5 E-Beam Writing on PMMA.....	71
3.2.3.3.2.6 Developing PMMA.....	72
3.2.3.3.2.7 Oxygen Plasma Etching	75
3.2.3.4 Electroplating.....	77
3.2.3.5 Stripping Photo Resist.....	79
3.3 Some of the Fabricated Pillars	81
Chapter 4 Result of Micro-Lithography Fabrication	85
4.1 Introduction.....	85
4.2 Effect of Ultraviolet Dosage	85
4.3 Effect of Air Gap between the Photo Mask and Photo Resist	90
4.4 Pulse Plating.....	96
4.5 Oxygen Plasma Etch.....	101
Chapter 5 Summary	104
5.1 Recommendations.....	105
REFERENCES.....	106
APPENDIX A: Best Known Method for Fabricating 0.25 μ m Pillars.....	115

List of Tables

Table 1.1 Atomic density (No. atoms/ \AA^3), crystallographic directions in indium, reproduced from [53]	19
Table 1.2. Atomic density (No. atoms/ \AA^3), crystallographic directions in indium, reproduced from [53]	20
Table 3.1 Milling condition of 10 μm pillar with FIB	42
Table 3.2 Milling condition for 3 μm with FIB	43
Table 3.3 Cr/Au deposition conditions	48
Table 3.4 Supplementary conditions for Cr/Au deposition	49
Table 3.5 Omni coat spin coating conditions.....	51
Table 3.6 SU-8 Spin coating conditions	52
Table 3.7 SU-8 soft bake Conditions	53
Table 3.8 SU-8 post exposure bake conditions.....	57
Table 3.9 Plating condition for the UV-10 μm micro-mold	81
Table 3.10 Plating condition of the E-Beam-500nm micro-mold.....	82
Table 3.11 Plating condition for E-Beam-250nm micro-mold	83
Table 3.12 Plating condition for E-beam-250 micro-mold.....	84
Table 4.1 PMMA etching rates corresponding to the applied	102
Table 5.1 Oxygen etch condition for removing AZ residues.....	118
Table 5.2 Oxygen Etch condition for removing PMMA residues	120

List of Figures

Figure 1.1 Tension stress-strain curve	4
Figure 1.2 Simple cubic structure	7
Figure 1.3 (a) Body-Centered cubic structure (b) Face-Centered cubic structure	8
Figure 2.1 Schematic of sample overall design	24
Figure 2.2 Summary of sample design.....	25
Figure 2.3 Basic Focus Ion Beam instrument, reproduced from [54].....	27
Figure 2.4 General steps in fabrication of pillars via microlithography: (1) micro- mold fabrication (2) indium deposition (3) revealing the pillars	30
Figure 2.5 (a) Overall view of the Micro Mold chip (b) SEM image of the controlling surface side wall (c) SEM image of the patterned area side wall.....	32
Figure 2.6 Steps for fabrication of micro-mold	34
Figure 2.7 Schematic of plating bath	35
Figure 2.8 SEM image of fabricated pillars via micro lithography	38
Figure 3.1 I-Beam image of 10 μm pillars. Crater size is 30 μm . Current was 2000 pA, and dosage was 500 $\mu\text{C}/\text{cm}^2$	42
Figure 3.2 Top view I-beam image of 30 μm crater and 5 μm island.....	43
Figure 3.3 I-beam image of FIB fabricated pillar having a diameter of 2.85 μm	44
Figure 3.4 Schematic over view design of chromium mask fabricated at University of Alberta	54
Figure 3.5 (a) Schematic of 0.5 μm photo mask on chromium mask (b) batch of 0.5 μm circular pattern (c) controlling surface pattern.....	55
Figure 3.6 SEM image of a SU-8 holes side wall, developed for less than 6 min.....	58
Figure 3.7 SEM image a SU-8 holes side wall, developed for 6 min.....	58
Figure 3.8 (a-b) SEM image of controlling surface side wall on a UV-micro-mold chip	59
Figure 3.9 (a-b) SEM image of holes side wall on a UV Micro–mold chip	60
Figure 3.10 (a-e) Steps for patterning the controlling area using an emulsion mask a) blank gold chip b) AZ-photo resist coating c) patterning controlling area d) gold and chrome etch e) stripping the resist to reveal the gold surface for the next step.	62
Figure 3.11 Schematic steps in fabrication of pillar growth site: a) tapping the controlling surface, b) spin coating PMMA, c) writing the patterned area with E-beam	63

Figure 3.12 Schematic of emulsion mask	64
Figure 3.13 Schematic of mylar design	65
Figure 3.14 Schematic of categorized area using the UV lithography.....	68
Figure 3.15 Schematic design of the pillar growth site.....	71
Figure 3.16 E-Beam write map with the applied dosage in each location.	72
Figure 3.17 Schematic of overall design of the E-beam micro – mold chip.....	73
Figure 3.18 (a-b) SEM image of processed E-Beam micro-mold chip: (a) Pillar growing site (b) controlling surface	74
Figure 3.19 Schematic of the side wall mold design	74
Figure 3.20 Schematic of DC circuit	77
Figure 3.21 SEM image of one of the pillar site batches in E- beam micro-mold chip samples	79
Figure 3.22 SEM images of 10µm pillars	81
Figure 3.23 SEM image of plated pillar diameter 0.5 µm height of 1.5 µm.....	82
Figure 3.24 SEM image of the 0.5 µm plated indium. [10min deposition time was high so the over plating indium forms these mushrooms	82
Figure 3.25 SEM image of 250 nm indium pillar	83
Figure 3.26 SEM images of 250nm fabricated pillars	84
Figure 4.1 Different film thicknesses of SU-8 absorbance vs. UV wavelength, reproduced from [65]	86
Figure 4.2 ((a)-(d)) SEM image of fabricated mold (a) – (b) dosage 1000 mJ/cm ² , (c)-(d) dosage 1800 mJ /cm ²	87
Figure 4.3 SEM image of the side wall as well as the holes on the micro-mold chip according to the applied condition.....	88
Figure 4.4 SEM image of the side wall as well as the holes on the micro-mold chip according to the applied condition.....	89
Figure 4.5 SEM image of the side wall as well as the holes on the micro-mold chip according to the applied condition.....	89
Figure 4.6 SEM image of developed 10 µm chip after post exposure bake.....	90
Figure 4.7 Schematic illustration of UV-light deviation due to the air gap	91
Figure 4.8 Schematic illustration of photo resist exposed and unexposed area under photo-mask black patterns.....	92

Figure 4.9 Intensity distribution of Fresnel diffraction for different air gap thickness: L_{fx} Fresnel diffraction intensity, L_{inc} intensity of incident vs. the photo mask distance from photo resist surface, reproduced from [69]	93
Figure 4.10 Intensity distribution of Fresnel diffraction before and after injecting Glycerol: L_{fx} Fresnel diffraction intensity, L_{inc} intensity of incident vs. the photo mask distance from photo resist surface, reproduced from [69]	94
Figure 4.11 SEM image of developed micro-mold side wall after Glycerol inject	94
Figure 4.12 SEM image of micro-mold side wall corresponding to the applied condition, before Glycerol inject.....	95
Figure 4.13 SEM image of micro-mold side wall corresponding to the applied condition, after Glycerol inject.....	95
Figure 4.14 Applied pulse plating wave form current density vs. time	97
Figure 4.15 Favored wave form for plating the micro-mold chips using potentiostat current density vs. time	98
Figure 4.16 SEM image of plated 250 nm micro-mold chip using potentiostat by applying 0.2 second 10.4 mA /cm ² and 10 min of 1.04 mA/ cm ² current density.	99
Figure 4.17 The applied wave form using Dc Power supply, current density mA /mm ² vs. time(s).....	100
Figure 4.18 SEM images of 250 nm pillars using Dc Power supply with 3.5 second 10.4 mA/cm ² current density and 10 min of 1.04 mA/cm ² current density.....	101
Figure 4.19 SEM images of 250 nm pillars using Dc Power supply with 3.5 second 10.4 mA/cm ² current density and 10 min of 1.04 mA /cm ² current density and oxygen plasma etch	103
Figure 5.1 E-Beam write map with the applied dosage in each section.....	119

List of Symbols

$\dot{\epsilon}$	Creep rate
θ	Angle change
A	Current
a	Distance between the planes
A	Area
b	Creep mechanism exponent
C	Constant depending on the material
D	Grain size
E	Young's module
F	Faraday constant
h	Height
H	Hardness
i	Current density
k	Boltzmann's constant
L	Length
L ₁	Initial length

L_{fx}	Fresnel diffraction intensity
L_{inc}	Intensity of incident
m	Transferred mass from the anode to cathode
M	Molecular weight
m	Creep mechanism exponent
n	Number of transferred electrons
P	Load
Q	Creep activation energy
R	Gas constant
t	Time period
T	Temperature
V	Voltage
γ	Shear strain
δ	Length change
ε	Average strain
η	Efficiency
ρ	Density

σ Average stress

τ Shear stress

List of Glossary

Climb: Motion of dislocation to the slip plane

Cross Slipping: transfer of glide of a screw dislocation from one slip plane to another during deformation or thermal recovery.

Dielectric Constant: degree of polarization or charge storage capability of a material when subjected to an electric field.

Dislocation Line: the intersection of the extra half-plane of atoms with the slip plane.

Dislocation Starvation: a state at which the crystal structure is free of dislocations

Dislocation: a linear crystalline defect.

Elastic Limit: stress at which the material starts to behave in a non-elastic manner.

Eucentric Position: eucentric implies, in specimen stage, that tilting the specimen can be achieved without the field of view moving. This is a highly desirable attribute of a microscope stage.

Failure: when a material loses its ability to satisfy the original design function.

Fresnel Diffraction: a process of diffraction which occurs when a wave passes through an aperture and diffracts in the near field.

Glide: motion of dislocations on the slip plane

Grain Boundary: zone formed at the junction of individual crystals in a polycrystalline material.

Hardness: resistance of materials surface to abrasion, scratching and indentation.

Jog: a step of atomic dimensions in a dislocation line. The Jog that lays in the glide plane of the dislocation known as a kink. Jogs may be formed by thermal activation at high temperatures and may also be formed at low temperatures by the intersection of dislocations.

Lattice: a lattice is the set of points upon which a crystal may be built by placing an identical basis, in the same orientation, on each of the lattice points.

Melting Point: temperature at which a material turns suddenly from solid to liquid.

Microstructure: the structural features of an alloy that is subject to observation under a microscope.

Necking: reducing the cross sectional area of the metal in an area by stretching.

Notches: V-shaped cut.

Perfect Crystal: crystal contains no defect.

Pinning: dislocations may get pin at points along their length by various objects including particles, grain boundaries and intersecting dislocations. Once pinned, a dislocation cannot glide.

Poisson's Ratio: negative ratio of the thickness decrease divided by the length increase as a result of a tensile stress applied to a material.

RCA Clean: standard wafer cleaning steps.

Real Crystal: crystal contains no defect.

Resistivity: intrinsic materials property that describes the ability of a material to resist, or oppose, the transport of electrical charge in response to an external electric field

Shear Modulus: ratio of shear stress divided by the shear strain in the elastic region. It can also be referred to as modulus of rigidity or torsion modulus.

Slip Displacement: the process which allows plastic flow to occur in metals, where the crystal planes slide past one another.

Slip Line: one part of the crystal slide as a unit across the neighboring side part along the slip direction on the surface of the plane, the line intersection of this surface with the outer surface of the crystal is called slip line.

Taylor Cone: cone observed in electro spinning and electro spraying process

Tensile Strength: maximum tensile stress a material can withstand before failure.

Thermal Expansion: term used to describe the change in dimensions that occurs with most materials as the temperature is increased or decreased

Un slipped Area: area where no planed have been slipped.

Young's Modulus: the proportionality constant of solids between elastic stress and elastic strain and describes the inherent stiffness of a material.

Chapter 1

Introduction

1.1 Theory

1.1.1 Material Strength

Material strength is expressed as the relationship between the internal forces, external load, and deformation in the material. The internal forces are defined as the stress acting over a certain area and are equal to the integral of the stress multiplied by the differential area upon which the stress acts. Since stress distribution cannot be physically measured, it can be substituted by strain distribution because these two qualities are proportional to each other.

1.1.2 Elastic-Plastic Behaviour

All solid materials deform when subjected to external loads. When the applied load is small, a solid will recover to its original shape after the load is removed. This behaviour is called *elastic deformation* and the limit beyond which the material no longer behaves elastically is called the *elastic limit*. If the load exceeds the elastic limit of a material, the deformation will be permanent. This permanent deformation is also known as *plastic deformation*. For most materials, deformation is linearly proportional to the load within the elastic limit. This relationship is expressed by Hook's Law but and is more commonly referred to as the stress-strain relationship [1].

1.1.3 Average Stress–Strain

As an example of how average stress-strain is expressed, consider a uniform cylindrical bar of a certain gage length (L_1) subjected to an axial tensile load. The average strain (ε) is the ratio of the changes in the bar length relative to its initial length.

$$\varepsilon = \frac{\delta}{L_1} = \frac{L - L_1}{L_1} \quad 1-1$$

Strain is dimensionless since both L and δ are measured in units of length. The load (P) being applied to the bar is balanced by the internal resisting force ($\int \sigma dA$):

$$P = \int \sigma dA \quad 1-2$$

Where P is the load, σ is the stress and A is the area upon which the stress is acting. Although the stress is not uniformly distributed over the surface, the average stress is defined as:

$$\sigma = \frac{P}{A} \quad 1-3$$

Hook's Law can then represent the strain and stress relationship as follows:

$$\sigma = E \times \varepsilon \quad 1-4$$

E is known as the module of elasticity, or Young's module.

1.1.4 Types of Stress-Strain

The stress acting upon a surface can be divided into two components: the nominal stress (σ) which is perpendicular to the surface and shear stress (τ) which is parallel to the surface:

$$\begin{aligned}\sigma &= \frac{P}{A} \cos \theta \\ \tau &= \frac{P}{A} \sin \theta\end{aligned}\tag{1-5}$$

Therefore, shear stress and normal stress can be defined for any plane. The strain can be divided in two elements for the acting force: the natural strain (ϵ) and the shear strain (γ). Natural strain is defined as the change in a linear dimension divided by the instantaneous value of the dimension.

$$\epsilon = \int_{L_1}^L \frac{dL}{L} = \ln \frac{L}{L_1}\tag{1-6}$$

Shear strain is the angle of rotation. If the angular change is assumed to be θ , the displacement due to shear stress must be equal to a and the distance between the planes be h , The shear strain will then be the ratio of a/h or the tangent of angle change θ :

$$\gamma = \frac{a}{h} = \tan \theta\tag{1-7}$$

1.1.5 Tensile Deformation in Ductile Metals

In tension tests, specimens are subjected to an increasing load until they fracture. This process allows the basic mechanical property of materials to be determined. Load and elongation

are measured at frequent intervals during the test. The average stress and the average strain are plotted in a stress-strain diagram.

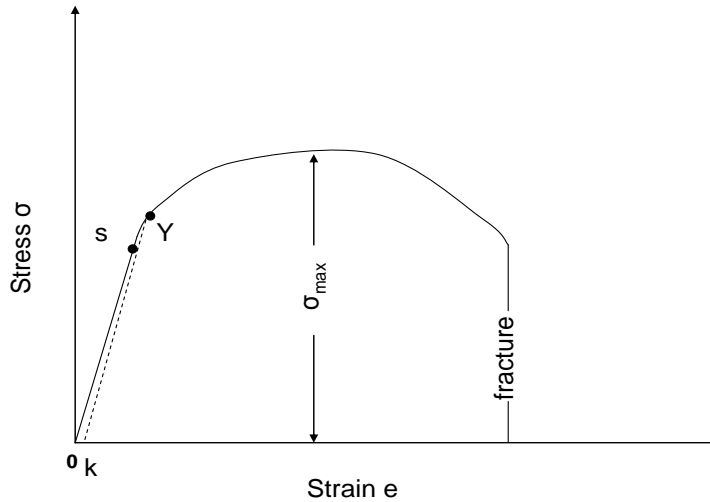


Figure 1.1 Tension stress-strain curve

The curve OS in Figure 1.1 is the elastic region in which Hook's Law is obeyed. Point S is the elastic limit. The slope of this curve gives the elastic module E. Point Y is the yield stress which will produce a small amount of permanent deformation. The permanent strain (O-k) corresponding to this stress is about 0.01-0.02 percent of the initial length. At the stress beyond the yield point, plastic deformation increases and metals become stronger so that the load required for deforming the specimen increases. The flow stress will reach a maximum value and

is called the *ultimate tensile strength*. The diameter of the specimen will decrease from this point while the stress required for further deformation will decrease until the specimen fractures.

1.1.6 Mechanical Failure

Mechanical failures may be categorized into three areas: (1) excessive elastic deformation, (2) yielding, and (3) fracture.

1.1.6.1 Excessive Elastic Deformation

Materials can experience excessive elastic deformation under conditions of equilibrium when a load is gradually applied, or under the conditions of unstable equilibrium. Excessive elastic deformation can result in fracture for brittle materials such as glass.

1.1.6.2 Yielding

Yielding is a permanent deformation at which point the elastic limit is exceeded. Due to strain-hardening at room temperature or under constant loading, yielding rarely results in fracture. Metals deforms continually under a constant stress at higher temperatures, and do not show a strain hardening. This time-dependent yielding is called creep. Failure prediction is complicated by the fact that a mechanical property of a material can change during loading, and also that stress at this point is not proportional to strain.

1.1.6.3 Fracture

Fracture can occur in three general ways: (1) brittle fracture, (2) fatigue, (3) delayed fracture.

(1) Fracture will occur in brittle materials when the applied stress is greater than their elastic limit. Decreases in temperature, increases in load rate, or the presence of notches may cause ductile metals to experience brittle fracture.

(2) Fatigue occurs in metals when the applied load is smaller than the yield stress and the applied load fluctuates or is alternating. Minute cracks will progress gradually until catastrophic failure.

(3) Delayed fracture will occur when a constant load is applied to a part for a long period of time. Fracture can occur without any significant sign of yielding, depending upon the temperature and the stress that is being applied.

1.1.7 Plastic Deformation of Single Crystals

Many experiments have been conducted on metallic crystals since the discovery of X-rays, to reveal the relationship between plastic behaviour and the atomic structure of metals. To investigate this relationship in the absence of the effect of the grain boundaries and neighboring grain boundaries, most of these studies have been carried out on single-crystal specimens.

1.1.8 Crystal Geometry Concepts

The atoms in metal crystals have a regular, repeated three-dimensional pattern. This arrangement appears as a crystal lattice in which the atoms are placed in a particular location. The crystallographic plane and direction are used to address the atoms in the crystals more easily. For example, the atoms in a simple cubic lattice crystal structure are located at the edge of the cubic lattice, as illustrated in Figure 1.2.

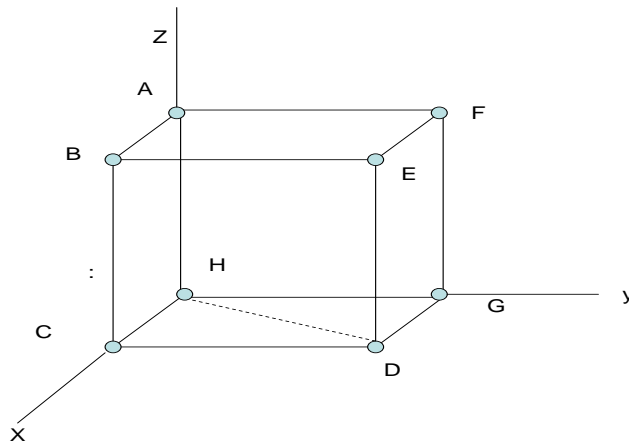


Figure 1.2 Simple cubic structure

After specifying the three axes (x, y, and z) through one corner of the crystal, the crystallographic plane and directions can be defined with respect to these axes. The plane BCDE in Figure 1.2 is parallel to the y and z axes and intersects with the x axis, so it will be designed as (100). There are six crystallographic planes to a cubic crystal: (010), (001), (100), ($\bar{1}00$), ($0\bar{1}0$), and ($00\bar{1}$). The bar indicates the plane's interaction with the axes in the negative direction. Crystallographic direction (110) represents the direction of HD, as this direction is obtained by moving from H to C and from C to D.

Many metal crystals have either a body-centered cubic (BCC) structure or a face-centered structure (FCC). As shown in Figure 1.3, the body-centered cubic structure has one atom in the

body of the crystal, and 8 atoms in each corner. Each atom is surrounded by eight atoms, so the number of atoms per crystal structure will be two: $(8/8+1) = 2$. In face-centered crystals, there is an atom in the center of each cubic face in addition to the corner atoms, making four atoms per structure. This is because the atoms in the center of the cubic face belong to two units: $(8/8+6/2) = 4$. In order to modify the planes and directions in the hexagonal close-packed structure (HCP), four axes should be used. Plastic deformation in this case is mainly limited to low-index planes that have a higher atom density.

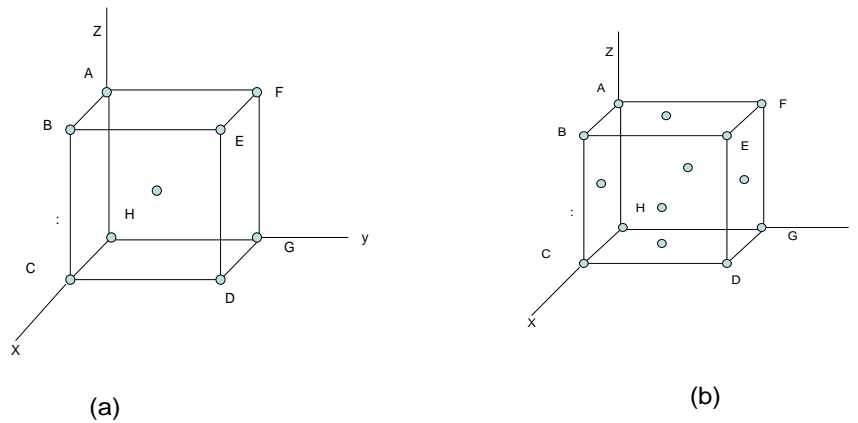


Figure 1.3 (a) Body-Centered cubic structure (b) Face-Centered cubic structure

1.1.9 Lattice Defect

As is to be expected, the arrangement of real crystals is imperfect. Instead, their structures deviate from perfect crystals due to the presence of some defects. Studying lattice defects is crucial because they directly affect the mechanical behaviour of materials. Any deviation from the ordinary crystal structure is called a defect. When this deviation is related to only a few atoms it is called a point defect. However, when defects increase they can be divided into three different categories: line, surface, and plane defects.

1.1.9.1 Point Defect

There are three types of point defects:

- I. Vacancy defects occur when an atom is missing from the normal lattice; these can be created by thermal excitation. Bombardment by high-energy particles can also result in increasing vacancy concentration [1]. If the density of vacancies increases they will cluster together and voids may be formed.
- II. Interstitial defects are the results of an atom being trapped inside the normal lattice. This type of point defect is the result of bombardment with high-energy particles rather than thermal activation.
- III. The presence of impurities at the interstitial positions or in the lattice positions is another type of point defect.

1.1.9.2 Dislocation

The most important line defects are dislocations, which are responsible for the slip phenomenon. Dislocations can also be defined by the line that separates the slipped and

unslipped areas in the crystals. Dislocations can move through the crystal in the absence of obstacles in response to the applied load, and the slips occur in the area over which they move. This can explain why real crystals deform much more easily compared to perfect crystals. The existence of dislocations can also clarify plastic deformation (strain hardening). Understanding dislocation is important not only for explaining the slip of crystals but also for studying all mechanical behaviour.

1.1.9.2.1 Burger Vector

The Burger vector is a vector whose magnitude is equal to the magnitude of the slip displacement and its direction, thus giving the direction of the slip. It can also be defined by the Burger circuit, which is a circuit that starts at one atomic position and traverses the same number of atoms on each side of the lattice until it reaches the starting point once again. If the circuit fails to close itself, the closure defect is called the Burger vector.

1.1.9.2.2 Dislocation Line

The plane that contains the dislocation is called the slip plane, and the dislocation line is the line that separates the slipped from the unslipped region. It never ends in the crystal unless it reaches the surface, forms a loop, or joins the other dislocation lines.

1.1.9.2.3 Edge Dislocation

Edge dislocation is one of two types of dislocations. This defect is usually a half-plane of atoms inserted into a portion of crystal as a response to an applied stress; thus, the Burger vector will be perpendicular to the dislocation line for edge dislocation. The climb of the edge

dislocation can occur due to the existence of vacancies. The vacancies change the atomic position so that the dislocation will climb the dislocation line and a jog will form at that point. Applying stress in a certain direction which is not in the direction of jog dislocations will pin the dislocation at the jog locations and the stress will bow them out in the form of loops. These loops can no longer be characterized as the edge dislocation and are called either screw or mixed dislocations.

1.1.9.2.4 Screw Dislocation

The slip in the screw dislocation occurs while the top and bottom of the crystals are being subjected to shear stress. The upper half of the crystal is displaced with respect to the bottom half in a helical motion. The Burger vector and dislocation line are parallel. The slip plane is different in every type of the crystals. For example, in face-centered cubic metals the slip occurs on the $\{111\}$ planes since their vertical separation distance is great and they are also the densest planes. The slip direction is $\langle 110 \rangle$ type direction. Screw dislocation can overcome this obstacle in crystals by cross slipping.

In reality, crystal dislocations are not straight lines and do not lie in a single crystal plane. However the character of most of the dislocations is formed partly of edge dislocations and partly of screw dislocations, which is called the mixed dislocation [2].

1.1.10 Creep

Creep is defined as a plastic deformation that occurs under a constant load at high temperature during a long period of time. Industry seems to be having difficulty successfully using metals at elevated temperatures because the strength of metal decreases as temperature

increases. The deformation mechanisms of metals change at high temperature and have a strong effect on the dislocation mobility, equilibrium concentration of vacancies, slip systems, grain boundary deformation, as well as other important factors [2]. Thus, it is important to investigate the mechanical properties of materials at elevated temperatures.

The duration that materials bear stress also plays an important role in determining their strength at the high temperatures. The creep test measures the dimensional change of material with respect to time. Some other high-temperature tests such as stress-rupture, relaxation, and thermal-shock resistance tests can be used to measure some other special properties of materials [2].

1.1.10.1 Creep Curve

Applying a constant stress greater than the elastic limit, materials show three stages of creep deformation, as illustrated in the creep curve in Figure 1.4. The primary stage of the creep, in which the strain rate decreases, can be the result of the dislocation climb, thermally-activated atom mobility, or additional slip plane, all of which enhance the deformation mechanism. The secondary stage, in which the strain rate is constant, can result from the balance between the increment of the slip plane and the increment of resistance to this increment due to the buildup of dislocations and other micro-structural barriers. In the final stage, the strain rate increases due to necking or internal cracking.

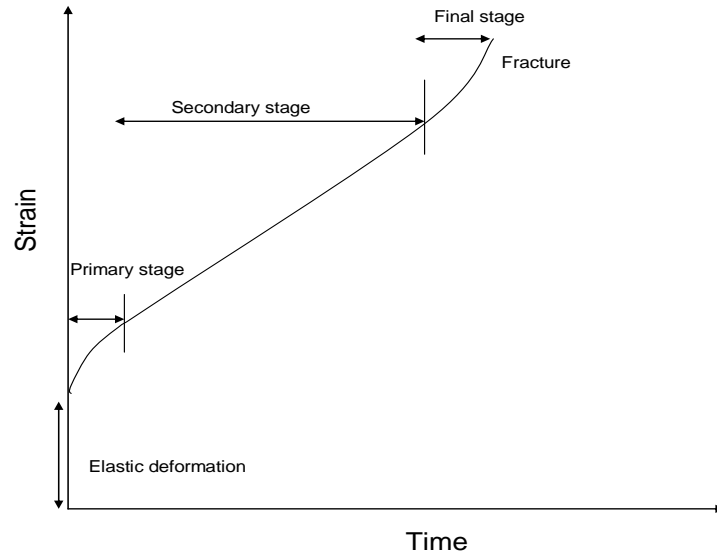


Figure 1.4 Creep Curve, reproduced from [3]

1.1.10.2 Types of Creep

There are two types of creep: Nabarro-Herring, and Coble. Creep occurs because of dislocation motion over time. When materials are subjected to constant stress greater than their elastic limit at high temperature, the vacancies of the crystals diffuse to the locations where the dislocations exist. This allows the dislocations to move more easily through the slip planes and cause deformation. The time dependency of creep can be explained by the fact that vacancies diffuse within the crystal gradually. The grain boundaries also play a dominant role in creep happening.

1.1.10.2.1 Nabarro-Herring Creep

In Nabarro-Herring creep, atoms diffuse throughout the lattice. This kind of creep depends strongly on temperature but not on grain size. For lattice diffusion of atoms to occur, there should be free sites in the crystals. The atoms must also overcome the barrier energy to move from their current site to the neighboring site. At temperatures near the melting point, vacancy concentration and thermal energy of atoms increase, which promotes this type of plastic deformation [2].

1.1.10.2.2 Coble Creep

Coble creep is dominated by grain boundary atomic diffusions. This kind of plastic deformation depends strongly on grain size rather than on temperature and can occur at the low temperatures. Since the number of boundaries along the surface of the grain is limited, the generation of the vacancies becomes less significant.

1.1.10.2.3 Creep Activation Energy

Creep activation energy (Q) can be extracted from the slope of the $\ln(\dot{\epsilon})$ versus $1/T$, as shown in Figure 1.5, where $\dot{\epsilon}$ is the secondary stage creep rate, T is the absolute temperature, and R is the gas constant.

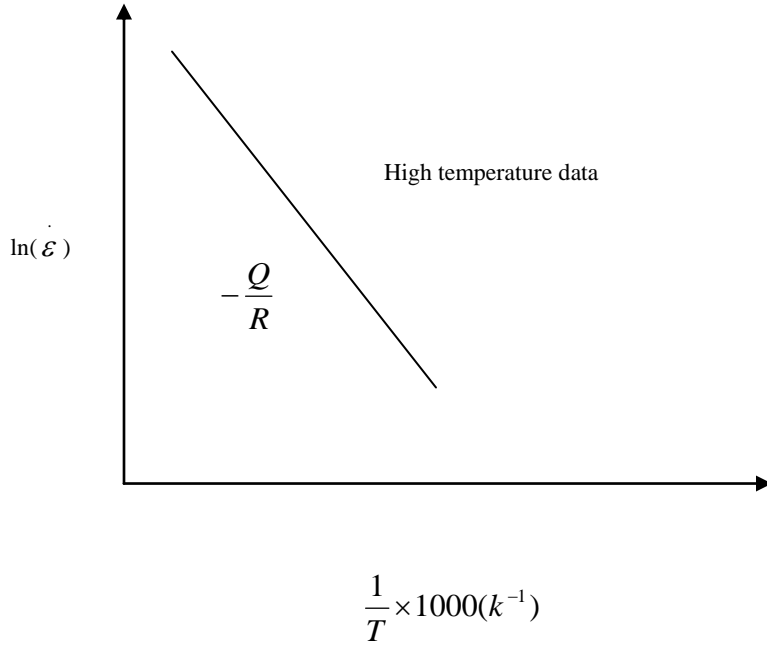


Figure 1.5 Plot of $\ln \dot{\epsilon}$ versus $1/T$ where $\dot{\epsilon}$ is the strain rate, T is the absolute temperature, Q is creep activation energy, reproduced from [3]

Creep rate can be expressed by the following equation:

$$\frac{d(\epsilon)}{dt} = \frac{C \sigma^m}{D^b} e^{\frac{-Q}{kT}} \quad 1-8$$

Creep strain is represent by ϵ while C is a constant dependent on the material, m and b are exponents dependent on the creep mechanism, Q is the activation energy of the creep mechanism, σ is the applied stress, k is the Boltzmann's constant, D is the grain size of the material, and t is the time period [3].

1.2 Motivation of Size-Dependent Creep Behaviour of Materials

Although the laws of classic mechanics seem to be applicable to predicting the mechanical behaviour of materials in all dimensions, many investigations during the past decade at the micron and sub-micron scales indicate that materials behave differently in their bulk than when they are broken down to a certain characteristic length scale [4-8]. An example of this divergence between the mechanical behaviours at the bulk and sub-micron scales was demonstrated in the work of researchers at Penn State University who created carving patterns on brittle materials such as glass and ceramics. They have affirmed that these brittle materials can be cut smoothly at the micron level because they behave like malleable materials [9].

While the dependency of material strength on dimension was neglected in studies of microscopic structures, many investigations indicate that size plays a central role in the strength of submicron-scale materials. The work done by Fleck et al [10] on a series of copper wires indicates that the diameter of the copper wires affects their flow stress during torsion testing. The smaller-diameter wires experience higher flow stress.

In order to understand the possible differences in the mechanical behaviour of micron-scale and bulk-size materials, the mechanical behaviour and properties of sub-micron materials must be directly measured rather than interpreted from the results of the bulk material.

Device size is a limiting factor in many current technologies. For example, micro-machined accelerometers constantly find more applications in vehicle airbags. In medical applications, using micron-sensors seems to be more efficient, less time-consuming, and less invasive for patients when compared with larger-scale traditional devices. Applying micro-

fluidic pumps in drug delivery appears to be safer and easier to administer than syringe methods [11-12].

Solar cell research is another area where reducing the scale of devices is crucial. The solar panels available today only convert 6% of the sun's radiant energy to electricity. Utilizing nanostructures, such as quantum dots made with semiconductor crystals, can capture a wider spectrum of light [13].

These applications of micron and nano devices in industry imply a great demand for understanding the physical properties of materials at the sub-micron scale. This understanding will have a direct impact on the efficacy and applicability of materials and can result in tuning the devices for specific applications. There is a great scientific motivation for studying the effect of length-scale at the sub-micron scale on creep behaviour, as this is one of the main mechanical behaviours of materials and is related to device lifetime.

Testing the creep behaviour of materials at the submicron scale has its own challenges. Conventional indentation testing cannot be used for probing the mechanical behaviour of materials at the submicron scale [14]. A new depth-sensing indentation technique must be applied with displacement resolution measured in nanometers and load resolution at the micron-Newton scale [15]. Material properties, such as hardness and elastic modulus, can be obtained by analyzing the depth-load data collected during the experiment [16]. Time-dependent tests done by depth-sensing indentation can be performed by pushing the micron-size indenter tip against the sample surface at a constant loading rate. Once the indenter reaches a pre-set load, the hardness of the sample can be calculated from the applied load and contact depth.

The stress exponent for the creep is then calculated from the slope of the plot $\ln \dot{\epsilon}$ versus $\ln H$ where $\dot{\epsilon}$ is the strain rate and H is the hardness for each loading rate and depth [17-21].

The other method of determining time-dependent plasticity is to ramp at a constant loading rate on the sample and then monitor the displacement of the indenter as the indenter tip penetrates the sample [17-21].

1.2.1 Indium Creep Behaviour

Testing the creep behaviour of materials with a sharp indenter tip presents the problem of flow stress, which causes creep to decrease as the experiment progresses. Therefore, no steady-state loading can be achieved. To avoid this problem, Chu and Li substitute the sharp indenter with a flat cylindrical tip [22-24]. The problem associated with this method is that the radius of the indenter tip defines the volume of the deformed material. In order to limit the plastically-deformed volume to a shallow depth, the tip size has to be reduced, which magnitudes the errors associated with the contact area of the punch and the sample [25-26].

1.2.2 Indium

Indium is the forty-ninth element of the periodic table. It has a face-centered tetragonal crystal structure with a melting point of 156.6 °C [27]. Its hardness is 0.9 HB, and at 20°C has elastic module of 12.74 Mpa in tension, a Poisson ratio of 0.4498, and density of 7.31g /cm³ [28]. The lattice parameter of indium at room temperature is a=4.5993 Å and c=4.9507 Å, which deviates slightly from the FCC structure. Like other metallic crystals, the plastic deformation of

indium occurs along the densest atomic row. Some of the atomic density crystallography directions of indium were measured as indicated in Table 1.1.

Direction	Atomic density	Relative Atomic density
[110]	0.30791	1
[101]	0.29685	0.9640
[100]	0.21780	0.7073
[001]	0.20260	0.6579
[211]	0.17556	0.5701
[112]	0.16935	0.5499

Table 1.1 Atomic density (No. atoms/ \AA^3), crystallographic directions in indium, reproduced from [53]

The glide plane which passes through the glide direction has also been observed to be the plane with the highest atomic density. Table 1.2 lists the relative and absolute atomic densities of some crystallographic planes in indium.

plane	Atomic density	Relative Atomic density
(110)	0.10431	1
(001)	0.09488	0.9606
(100)	0.08830	0.8465
(101)	0.06464	0.6196
(012)	0.06269	0.6009
(110)	0.06244	0.5985

Table 1.2. Atomic density (No. atoms/ Å^3), crystallographic directions in indium, reproduced from [53]

Van Der Biest et al [53] have reported that at 77 °K the (111) plane, which is the densest, operates as the glide plane and the [110] and [011] are the glide directions with the highest-packed atomic density. The critical shear stress was measured to be around 20g/mm², which decreases as temperature increases. The (001) and (101) planes have been found to be the glide planes at room temperature.

Indium ductility and softness can be retained at temperatures around absolute zero. Indium has a number of significant characteristics, making it ideal for use in a wide range of applications, including cold welding, metal vitamin, improved resistance, thermal fatigue, reduced gold scavenging, and low melting point alloys [28].

1.2.3 Indentation Size Effect

A possible explanation of the indentation size effect (ISE) in materials was introduced by Nix and Gao [29]. They declared that due to the strong strain gradient, which can either be caused by loading geometry or inhomogeneous deformation in materials themselves, the “geometrically necessary” dislocation density will be more pronounced in smaller-sized materials [30]. Their model for strengthening smaller-sized materials was on the continuum basis and could not predict the discrete displacement burst of materials at the very initial stage (less than 100nm) of indentation depth sensing [31-36].

Constraining effects were present in most of the research that was conducted on the effect of size on either bulk or thin film materials [36-41]. In order to exclude the constraining effect, Greer et al [42] prepared some unconstrained freestanding gold pillars on which they conducted a compression test. Using a uniaxial compression test in which a flat indenter tip was substituted with the sharp Berkovich tip in the depth-sensing equipment, they were able to study strain hardening in micro-pillars without the presence of a strong strain gradient. As a result, they have stated that material strengthens inversely to its size even in the absence of a strong strain gradient. In their approach they have related this strengthening to the dislocation starvation condition, which is limited to small-volume samples. The nucleation of new dislocation seems to be the most challenging for plastic mechanisms after the dislocation starvation condition [42-45]. Some other compression tests have been conducted on micro pillars of Ni, Al, Ni₃Al, Cu, and Mo alloy, all of which stated that the yield strength of material increased with decreasing in pillar diameters [46-52].

Although the “dislocation starvation” theory explains the existence of discrete displacements at the first stage of the indentation test, there is no unified theory that can explain this size effect [42-45]. For example, while dislocation starvation seems to be the dominant mechanism for plasticity in the FCC single crystals, it cannot be the central mechanism for the BCC single crystals [51] or in metallic glasses, where size effect plasticity is also observed even though they do not contain any dislocations [52].

1.3 Objective of the Work

Unlike most of the research that was limited to the study of monotonic deformation in materials, the present work intends to investigate the effect of size on the creep behaviour of materials at the submicron scale in the absence of strong strain gradient and the constrain effect.

To conduct ambient temperature compression testing, and skip the small displacement associated with elevated temperatures, and also to reduce the testing time of the time-dependent creep phenomenon, indium was selected as the testing metal.

Samples have been fabricated by two different methods in order to account for the effect of fabrication method. To monitor the creep mechanism that is dominant in our testing, samples have been characterized in two general ways: as single crystalline and polycrystalline samples. The polycrystalline samples have been differentiated in such a way that they contain different grain boundary sizes.

Further more to observe the creep behaviour of materials in the absence of strain gradient plasticity a compression test was chosen in which the sharp Berkovich tip was substituted by a flat diamond tip.

Chapter 2

Sample Design

2.1 Introduction

In order to gain insight into the deformation mechanism that leads to plasticity at the micron and submicron scales, the present work developed the submicron indium samples to test their creep behaviour in the absence of a strong strain gradient. The test methodology consisted of fabricating the single-crystalline and poly-crystalline freestanding indium cylinders at submicron dimensions. This chapter will introduce the sample design and also the techniques that have been applied for fabricating the samples.

2.2 Sample Design

As mentioned above, the present work fabricates submicron-scale indium samples to test their creep behaviour in the absence of strain gradient plasticity. To fulfill the objectives of the mentioned topic, the sample design should satisfy three essential criteria outlined below.

First, the sample design should provide unconstrained geometry with a flat top. This minimizes the effect of the strain gradients in the compression test. Based on this fact, the overall view of the samples should be a flat top cylindrical unconstrained shape. Compared to other shape features, cylinders have less strain gradient deformation during compression testing. A schematic overall view of the sample was illustrated in Figure 2.1.

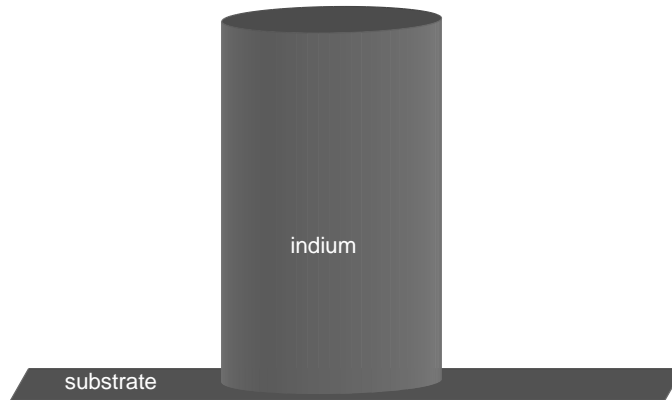


Figure 2.1 Schematic of sample overall design

The second parameter is sample diameter. A reasonable range of diameters provides a more realistic analysis of the effect of size in creep behaviour. For this reason, a range of diameters from 100nm-10 μ m have been considered to provide reasonable data.

The third factor for categorizing the samples was the creep mechanism. The dominant creep mechanism is dissimilar in single crystals and poly-crystals, so each sample size was categorized into these two major groups. The poly-crystal pillars have also been grouped by different grain boundary sizes in order to gain insight into their effect on creep behaviour at the submicron scale. Figure 2.2 summarized the sample categorization based on the aforementioned factors.

D(μm)	0.1	0.25	0.5	1	2	5	10
Crystal							
Single crystal							
Poly crystals	Single crystal						
	50						
	500						
	3000						

Figure 2.2 Summary of sample design

2.3 Fabrication Techniques

Having the samples designed, the most difficult challenge is to then fabricate them. Many researchers use focus ion beam (FIB) in their studies to fabricate freestanding submicron pillars [42-52], meaning that the FIB is used as the first approach. This instrument is equipped with a focused Ga⁺ ion beam and a high-resolution field emission scanning electron column; both of these features propagate a submicron precision etch on the sample surface.

Unfortunately, fabricating the indium submicron pillars using the FIB was not an appropriate technique in this project because the indium metal was melted away by high-energy Ga^+ ions before forming the submicron diameter pillars. Therefore, the low melting point indium metal limited the application of the FIB.

As a result, the microlithography and electroplating approach that is widely used in the industrial fabrication of integrated circuits (ICs) was applied. A large number of indium pillars with a predesigned diameter can be fabricated on a silicon substrate by this technique.

2.3.1 Focus Ion Beam Instrument

The focus ion beam (FIB) instrument resembles the secondary electron microscope (SEM), with one major difference. In FIB, the ion beam is applied for analysis whereas an electron beam is applied in SEM.

The main parts of the Focus Ion Beam instrument consist of liquid metal ions, an ion column, a gas injector, and a sample stage, as illustrated schematically in Figure 2.3.

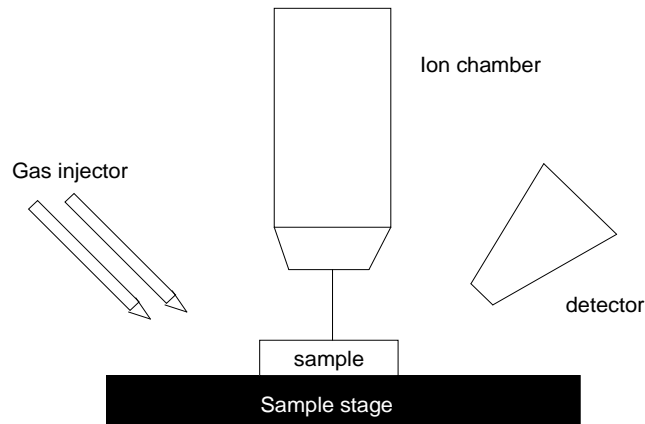


Figure 2.3 Basic Focus Ion Beam instrument, reproduced from [54]

The main parts of the FIB instrument are the column ion and liquid metal ion source (LMIS), where a gallium metal is attached to a tungsten needle and then heated. The gallium can be replaced by different metals. However, some of the characteristics of gallium make it the best choice for the LMIS. Some of these characteristics are [54]:

- i) Low liquid volatility, which preserves the chamber longer
- ii) Low melting point (29.8°C) and low free-surface tension, which facilitate the formation of the Taylor cone at the tungsten needle
- iii) Low vapor pressure, which ensures the formation of a pure form of vapor rather than the alloy component

The gallium ion is emitted through two steps; first, the gallium is heated and wets the tungsten needle with a typical tip radius of 2-5 μm ; second, an electric field of 108V/cm at the tip causes the molten gallium to form a 2-5nm diameter Taylor cone. Once the electrostatic and surface tension forces are in balance, the extraction voltage pulls the gallium off the needle and ionizes it at the cone end. Once the Ga^+ has left the tip, it will accelerate through the potential down the ion column. The continuation of this process will increase the current density. A typical accelerating voltage is about 5-50 kv.

The ion column consists of two lenses; (1) a condenser lens, which is probe-forming, and (2) an objective lens, which focuses the ion beam onto the target (sample surface). The current range can be varied from a few pA to 20-30 nA for various applications by various diameter apertures in the ion column.

When the Ga^+ strikes the sample surface, many species will be generated, including sputtered atoms, molecules, secondary electrons, and secondary ions [54].

2.3.1.1 The Stage

The sample stage has the ability to move in five axis directions. It is important to ensure that the large stage (>300mm samples) is thermally stable and that no heat will be generated because of its mechanical motion. This will avoid thermal drift in the sample during FIB imaging or deposition.

2.3.1.2 Imaging Detector

Two types of detectors are used for imaging the sample surface. One is a multichannel plate and the other is a multiplier that can be set for detecting either the secondary electrons or the secondary positive ions.

2.3.1.3 Gas Injectors

The FIB instrument can also be applied to micromachining applications and thin-film deposition. This ability of FIB systems was facilitated by the existence of gas injectors. Gas direction will be applied in conjunction with ion beams to produce a specified site for material deposition or insulator to enhance etching capability. Additionally, the sputtering rate can be facilitated by introducing specific species to the chamber [54].

Commercial FIB systems are equipped with some other analytical equipment such as the secondary ion beam (SIB), energy dispersive spectrum (EDS), integrating electron backscatter diffraction (EBSD) and secondary ion mass spectrometer (SIMS) and secondary electron microscope (SEM). The FIB/SEM is the most common dual platform out of all the aforementioned equipments [54].

2.3.2 Microlithography

The lithography-governed approach to the fabrication of indium pillars, as demonstrated in Figure 2.4, contains three general steps: (1) micro-mold fabrication, (2) indium deposition utilizing electroplating, and (3) stripping the fabricated mold to reveal the plated indium.

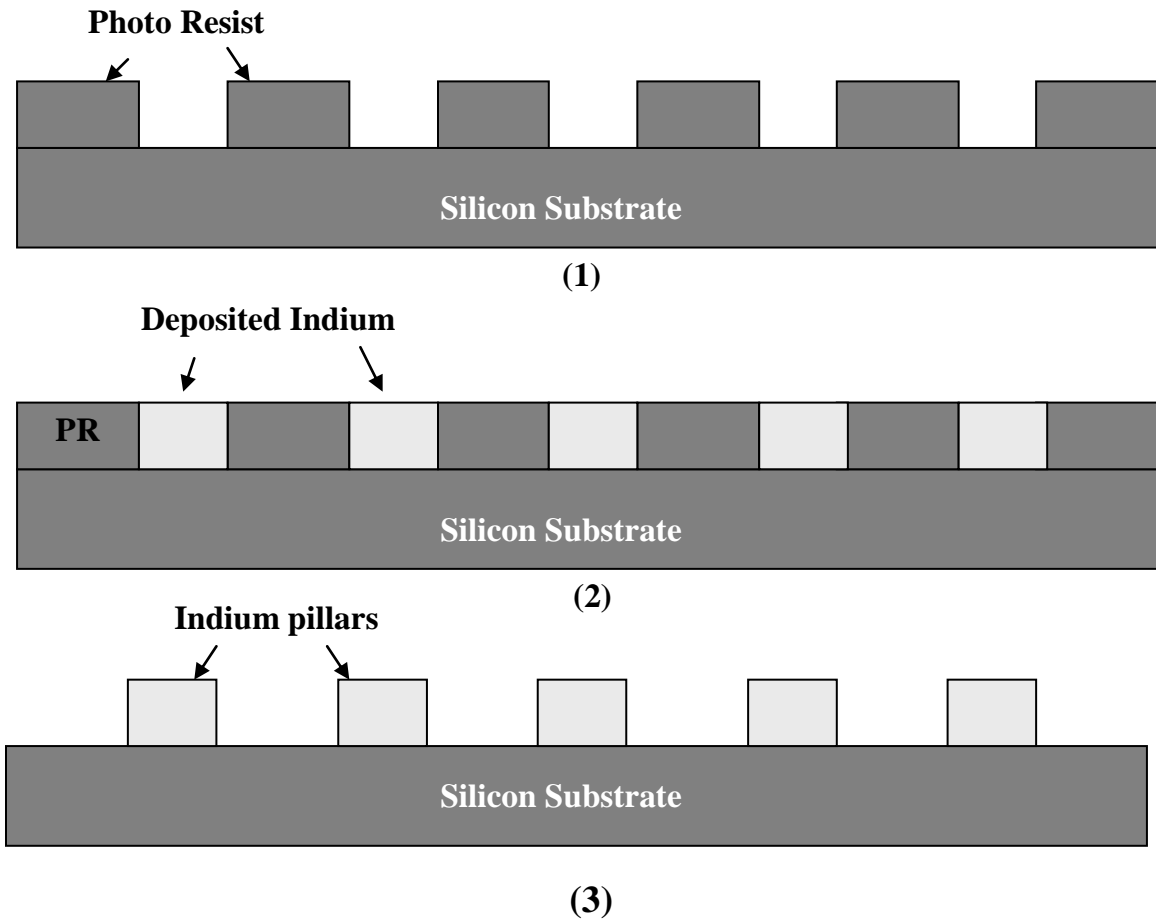


Figure 2.4 General steps in fabrication of pillars via microlithography: (1) micro- mold fabrication (2) indium deposition (3) revealing the pillars

2.3.2.1 Micro- Mold Fabrication

The first step in the fabrication of micro-mold chips is to design the mold pattern, followed by the development of a fabrication process for the desired pattern.

2.3.2.1.1 Micro-Mold Chips Design

The design pattern of micro-mold chips consists of a patterned mold with a controlling surface and a conductive surface. The patterned mold section consists of circular shape features whose diameters correspond to the diameters of the pillar samples. A fixed controlling surface was considered for the chips in order to provide a steady-state current density during the electroplating deposition process. The controlling surface was arranged in an array form having sub-micron width, which is in approximate with the indium growing pillars diameter. This improves current distribution during the plating process. A conductive surface was designed for the chips in order to pass the current to the indium deposition sites during the electrodeposition process. The size of the mold-chip was chosen 2.54 x 2.54 cm in accordance with the available photo-masks. The bottom surface of all the mentioned patterns must be coated with a good conductor, such as gold, in order to pass the current for indium deposition. The overall design of the mold is illustrated in Figure 2.5.

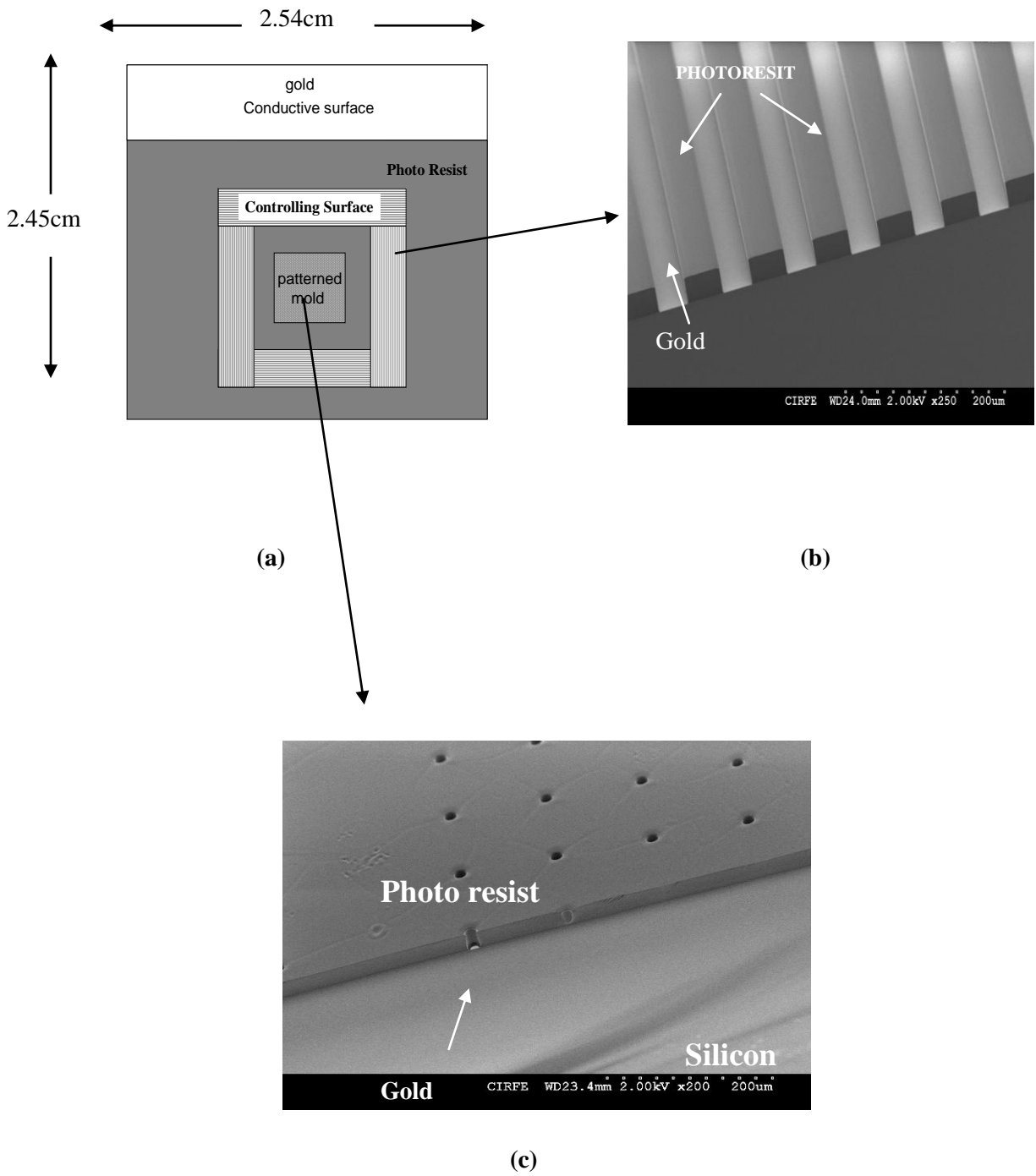


Figure 2.5 (a) Overall view of the Micro Mold chip (b) SEM image of the controlling surface side wall (c) SEM image of the patterned area side wall

2.3.2.1.2 Micro-Mold Fabrication Process

The micro-mold is a shaped mold upon which the indium is filled. Photolithography is applied to project the designed pattern onto the chip surface. In this process, a light-sensitive material known as a photo resist, usually in liquid form, is spun on the wafer surface by spin coating. Spinning the photo resist will form a film whose thickness depends directly on the spin speed and the duration of spinning. The wafers are heated through a process, known as the soft bake. The soft bake step drives the solvent off of the photo resist and leaves a solid photo resist layer on the wafer. The wafer is then exposed to an appropriate dosage of ultraviolet (UV) light, or electron-beam for higher resolution patterning. The exposure process causes a chemical reaction in the photo resist which alters its solubility in the developer. The photo resist can either be positive or negative. Chemical reactions cause the negative photo resist to become less soluble in the developer while they make the positive photo resist become more soluble in the developer. The wafer is then developed, and the unwanted resist is removed while the desired patterns remain.

The main steps for fabricating the mold are:

1. Coating the substrate with gold as the conductor medium
2. Spin coating the chrome/gold surface with a photo resist
3. Lithographically patterning the photo resist
4. Developing the photo resist in a developer

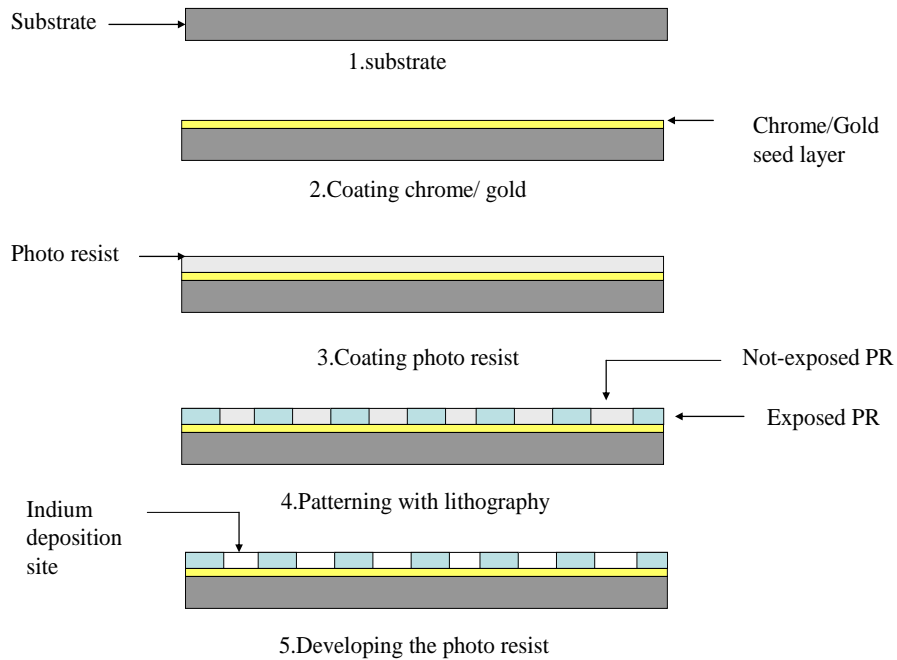


Figure 2.6 Steps for fabrication of micro-mold

The detailed procedure of micro-mold fabrication will be discussed in the next chapter.

2.3.2.2 Electro-Depositing

Electroplating, which is widely used in microelectromechanical systems (MEMS) fabrications, was applied for indium deposition. Electroplating was chosen for use in the deposition process because it provides excellent characteristics such as refined grain structure, smoothness and low residual stress, to the deposited material [55-60]. In addition to the quality of the plating, the ability to coat thin layers using low-cost procedures means that electroplating is preferred over other methods of deposition [59].

2.3.2.2.1 Principal of Electroplating Process

Electroplating systems basically contain an anode (the metal that is to be plated) a cathode (the substrate upon which the metal will be deposited) and an electroplating bath. The bath is usually a saline solution responsible for improving the solution conductivity, anode solubility, and ionic strength. Some additional agents may be added to the solution to enhance the quality of deposition and prevent powdering or irregular coating [61].

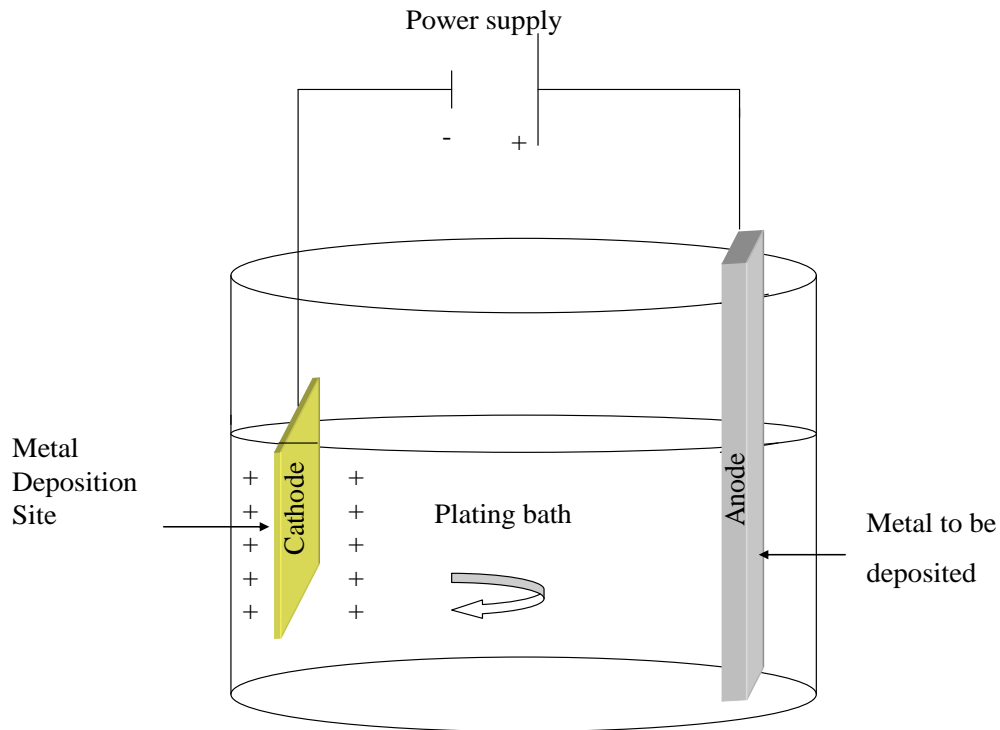


Figure 2.7 Schematic of plating bath

During electroplating, some variables such as current density, agitation, temperature, and pH affect the physical characteristics of the deposited material and also the deposition rate of the plating [61].

2.3.2.2.2 Current Density

Current density, which is the amount of current passing through 1cm^2 of area, can be examined from two points of view: (1) diffusion control, or (2) cathode potential [61].

- 1) Diffusion control refers to the movement of ions in the solution as a result of concentration gradient. Diffusion is the consequence of random molecular motions which distribute the various specimens uniformly throughout the solution. Depletion ions in the anode will produce ion gradient concentration in the solution, resulting in the movement of these specimens from the anode towards the cathode.
- 2) Potential control is established when both the anode and cathode are connected to an external power supply and an electric field is established in the bath. This field will lead the ions, having a positive charge, towards the cathode. The electrical current will then reduce the anode and coat the material on a conductive object (cathode) in the form of a thin layer.

The effect of current density on the deposition rate is very much dependent on the plating system, and can be altered by agitation, changing the pH, temperature, and some other factors. Therefore, there is no universal rule for measuring its influence on the deposition rate.

Indium was applied as the anode in the plating system and the micro-mold chip as the cathode. A range of different values for the current density was tested and the optimal current

density which satisfies the high-quality deposition for the plating system chosen. Deposition rates can be calculated from the deposited thickness and the duration of plating.

Using the Faraday's Law equation [62], thickness can be estimated by the current density applied and the duration of the plating process. Faraday's equation is:

$$m = \frac{AtM}{nF\eta} \quad 2-1$$

Where m is the transferred mass from the anode to cathode (g), A is current (A), M is molecular weight (g), n is the number of the transferred electron, F is Faraday constant and η is efficiency.

2.3.2.3 Revealing the Pillars

After plating the indium, the next step is to remove the sacrificial layer to reveal the pillars. In this step, depending on the kind of resist that was applied, a resist remover is chosen to strip unwanted surfaces. Freestanding indium pillars will be released during this step. Figure 2.8 illustrates some of the pillars fabricated using the microlithography approach.

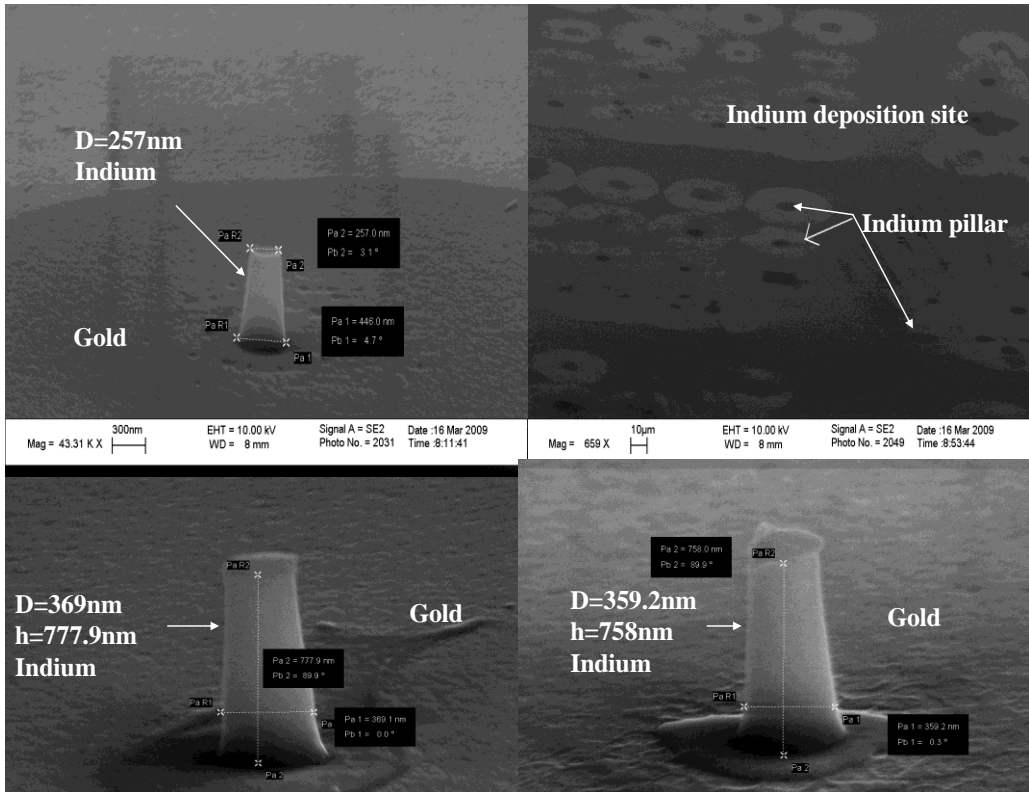


Figure 2.8 SEM image of fabricated pillars via micro lithography

Chapter 3

Sample Fabrication

3.1 Introduction

Sample preparation is one of the greatest challenges in this work because a versatile sample diameter and category must be considered. Equipment availability was also a limiting parameter. The fabrication procedure was conducted in the MEMS facility of the Centre for Integrated RF Engineering (CIRFE) at the University of Waterloo. Fabrication of the designed samples was performed based on the available equipment and facilities.

Although the micro-fabrication method was widely applied during the past decade, there is no unified procedure to be followed in the fabrication of each sample design. As a result, processes need to specifically develop for each design.

This chapter shares invaluable experience that was achieved during the development of a microlithography process for making freestanding submicron pillars. The process is based on using indium as our testing metal. This chapter will also cover the results and the detailed development procedure and the related characterizations in fabrication of different pillar diameter.

3.2 Sample Fabrication

As mentioned in section 2.3, the first approach to FIB was applied in the fabrication of the pillars. The low melting point of indium limited its fabrication using FIB therefore

microlithography was developed. The following two sections will present the results of the two fabrication techniques.

3.2.1 Sample Fabrication using the Focused Ion Beam (FIB)

To fabricate the patterns of interest, a Leo/Zeiss 1540XB SEM/FIB Crossbeam at the Nanofabrication Laboratory of the University of Western Ontario was used. The ion dose, expressed in $\mu\text{C}/\text{cm}^2$, controlled the amount of material sputtering from the surface. A deeper mill can be achieved by employing a higher dose of beam, which irradiates a larger number of high-energy ions onto the sample surface. This will cause more ions to sputter from the surface. The ion current (C/sec) controls the rate at which the required dose of ions are transmitted to the specimen. Although a higher current gives faster milling which requires less time and lower operating costs, it causes less focus in the beam by adding a tail to it which decreases the precision in the milled area. The applied accelerating voltage and beam angle are based on previous experience in the lab and were not changed. The applied accelerating voltage was 30kV and the beam angle was 90° throughout the experiment.

The FIB process was conducted on well-annealed single-crystal indium. The indium slab was first annealed at 100°C for two hours in an oven and polished by electro-polishing.

The applied electropolishing solution was a 3:1 mix of methanol and nitric acid with a voltage of 32v at 0°C [24]. The anode was a 3.8 x 2.54 cm indium slab with the thickness of ~2 mm and the cathode was a 14 cm x 3 cm graphite bar.

For any further polishing, another solution with a lower voltage and better quality of surface polishing was applied. This polishing condition was based on the work of Schoeller and

Cho. With a 1:3 mix of nitric acid and ethanol and a voltage of 4v [63], Based on this recipe, the polishing rate was calculated to be 100nm/sec.

3.2.2 Focus Ion Beam Fabrication Results

The first step in the fabrication process was selecting an appropriate section of the sample for machining. It is important to ensure that the selected surface has very few particles and is smooth, as any surface roughness will result in non-uniform etching.

In the FIB instrument, the stage and sample are adjusted to the eucentric position, where the ion beam and the electron beam are focused with the same working distance that usually equals 6mm. The sample is then tilted to 52.7° with respect to the electron detector.

When milling the surface to the desired geometry, it is required that the pillars be surrounded by a crater. As a result, the crater is milled first and then the pillar is created in its centre by sequential etching of concentric circles with smaller and smaller inner diameters. Having the pillar in the crater helps to prevent the indenter tip from misaligning and coming into contact with other features, such as the edges, during the compression test [52].

Current of Ga^+ ion of 2000 pA with $500 \mu\text{C}/\text{cm}^2$ dosages was applied to mill out the $30 \mu\text{m}$ crater in the material and then leave a $10 \mu\text{m}$ diameter pillar in the center, as illustrated in Figure 3.1.

Table 3.1 Milling condition of 10 μm pillar with FIB

Current PA	Voltage Kv	Crater diameter μm	Tilt angle	Diameter μm	Dosage $\mu\text{C}/\text{cm}^2$
2000	30	30	52.7	10	500

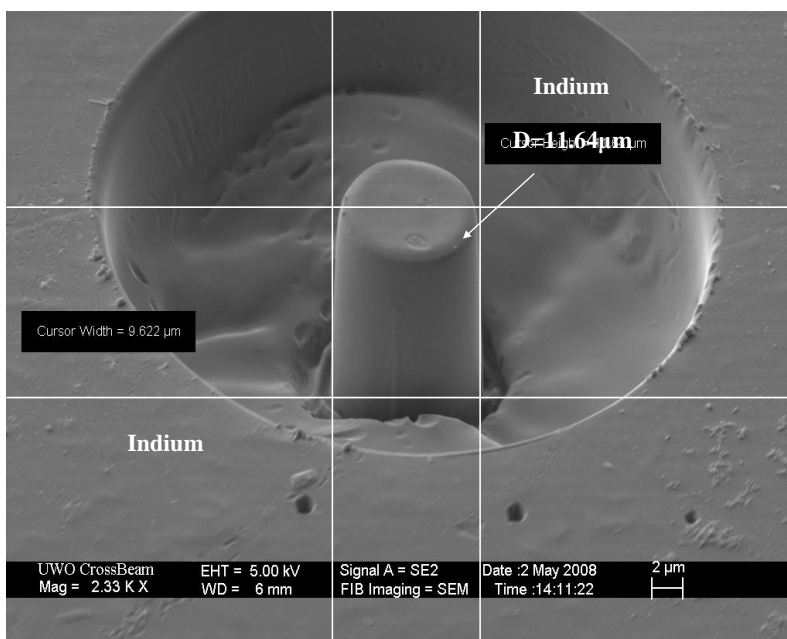


Figure 3.1 I-Beam image of 10 μm pillars. Crater size is 30 μm . Current was 2000 pA, and dosage was 500 $\mu\text{C}/\text{cm}^2$

During fabrication of the smaller-diameter samples, two sets of dosages were applied; first, from 30 μm to 5 μm diameter, a dosage of 500 $\mu\text{C}/\text{cm}^2$ with 1000 pA ion current was applied, and then from 5 μm to 3 μm a lower dosage of 100 $\mu\text{C}/\text{cm}^2$ with 1000 pA Ion current was used.

Table 3.2 Milling condition for 3 μm with FIB

Current PA	Voltage kv	Crater diameter μm	Tilt angle	Diameter μm	Dosage $\mu\text{C}/\text{cm}^2$
1000	30	30	52.7	5	500
1000	30	30	52.7	3	100

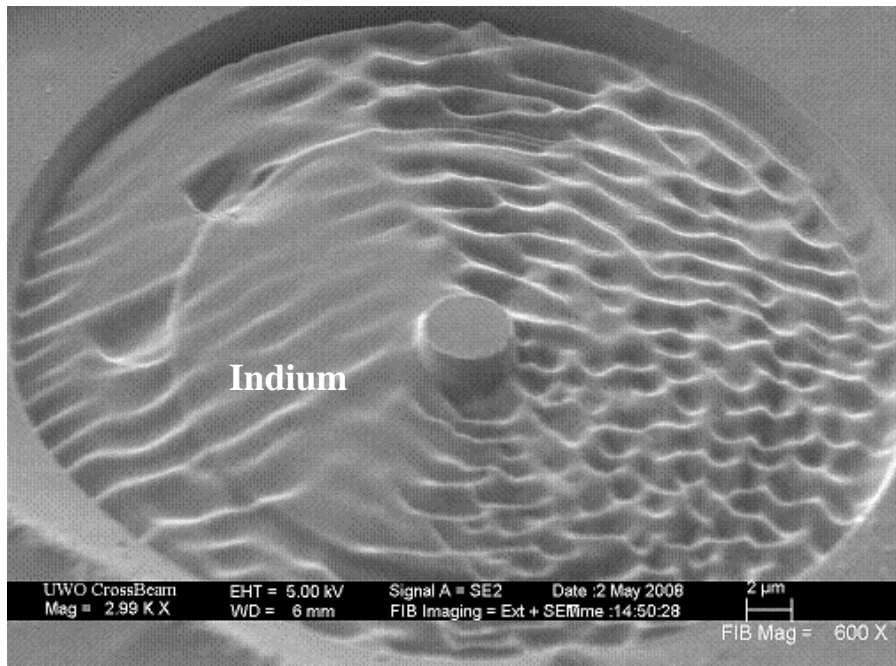


Figure 3.2 Top view I-beam image of 30 μm crater and 5 μm island

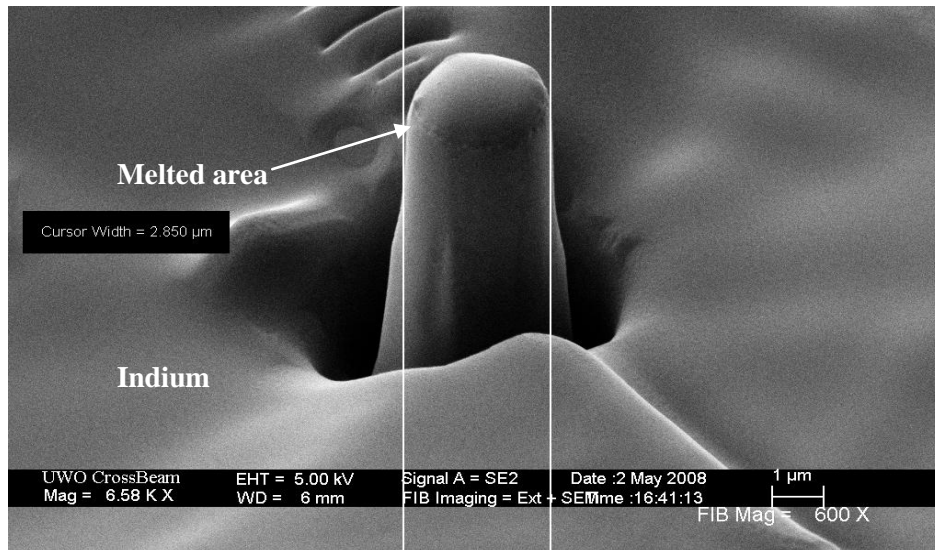


Figure 3.3 I-beam image of FIB fabricated pillar having a diameter of 2.85 μm

As can be seen in Figure 3.3, during the fabrication of finer feature samples even a low dosage of Ga^+ will melt away the indium metal before forming it, which is due to the low melting point of indium. Some other challenges were also observed, such as base trench formation, pillar tapering, and also possible Ga^+ implantation into the indium samples. As the diameter of the concentric circles becomes smaller, the pillars become more tapered. This tapering is mainly due to the I-beam imaging that causes some inevitable etching which is negligible for larger features but becomes an important concern for the smaller-diameter pillars ($<3\mu\text{m}$). Although applying a set of different currents and dosages may improve the structure of the formed pillars, the cost of fabrication and the unavailability of these facilities on campus limited led the use of an alternative technique which is essentially based on lithographic micro fabrication.

3.2.3 Sample Fabrication using Microlithography

Having failed to create samples using FIB, the micro-lithography, which is widely used for the industrial production of ICs, was developed in the fabrication of low melting point indium samples. All of the equipment used belongs to the CIRF Lab at the University of Waterloo unless stated otherwise.

In this method, the substrate, a standard <100> Si, is coated with chromium and gold and then the wafers are processed by electro-deposition for growing the indium pillars.

3.2.3.1 Substrate

Choosing the substrate is the first step in the micro-fabrication process. In the present work, because the substrate was coated with other materials, some common properties such as electrical insulation, orientation, and resistivity become unimportant. Therefore, silicon, as the cheapest and most available substrate, was used in 2.54 x 2.54 cm diameter chips.

Contaminants must be removed from the surface prior to processing in order to achieve high-quality film deposition on the substrate. RCA cleaning was used for this purpose [64]. This cleaning method usually contains three steps in which the organic residue, native oxide layer, and inorganic residue are removed.

In RCA 1, 5:1:1H₂O/H₂O₂/NH₄OH solution at 75°C is used.

The procedure is as follows:

1. Add 100 mL, NH₄OH to a 500 mL, DI water to the RCA beaker and place a thermometer in the beaker.
2. Heat the beaker to 70 °C on a hotplate.

3. Clean the sample wafers with DI water and/or acetone and dry them with a nitrogen gas gun. Place them in a wafer holder.
4. At 70 °C, pour 100 mL of hydrogen peroxide into the solution while a magnetic stirrer is stirring it.
5. Submerge the wafer with a wafer holder in to the beaker and heat it for 15 minutes.
6. Prepare 700ml of DI water in the hot water bath beaker and heat it to ~ 80-90°C on a separate hotplate. Cover the beaker with a lid.
7. After 15 minutes, remove the wafer holder. put it in a hot bath beaker, and heat it for another 15 minutes.
8. Wash the beaker under running DI water.
9. Blow dry the wafer with nitrogen gas.

In the RCA1, heating the wafers in a high-pH solution will remove organic contaminants by oxidative dissolution while heavy metals dissolve, form a complex, and are rinsed away with DI water. In the RCA2, the inorganic contaminants can be removed in the low-pH solution using $\text{H}_2\text{O}/\text{H}_2\text{O}_2/\text{HCL}$. In the RCA3, submerging the silicon wafers in the dilute HF solution will remove the thin oxide layer. As the effect of inorganic contaminants and the oxide layer are negligible, only RCA1 was applied.

3.2.3.2 Gold & Chromium Deposition

The next step is to coat the substrate with a highly conductive metal. Gold was chosen as a conductive medium because it does not adhere to silicon. Silicon must be the first to be deposited, with chromium as a middle layer, followed by gold. The thickness of each layer must be large enough to give a uniform surface.

The Cr/Au deposition took place in a Nanochrome™ DC sputtering system (Intelvac, Canada). In this vacuum sputter chamber, the E-beam gun, having a power range from 6 to 208 kW, focuses and accelerates the E-beam towards the target (the metal). A certain percentage of the kinetic energy from the E-beam is converted into thermal energy, which melts the metal ingot. Since the chamber is under a highly-vacuum the metal will evaporate and be deposited on the substrate. Following deposition, a shutter blocks the E-beam gun and the metal cools to room temperature, which takes approximately ten to fifteen minutes.

3.2.3.2.1 E-beam Evaporation Deposition

Substrate

Substrates are fixed manually in the substrate holder at six spots. The maximum size of the substrate should be less than five inches in diameter. The substrate face on which deposition is being performed should face down.

Material deposition

The materials that get deposited are placed in a copper crucible in the form of an ingot. A pocket controller controls a shaft and places the metal under the E-Beam gun. It is important to mix the ingot before each deposition to bring up the fresh metals from the underneath

Vacuum chamber

Cryogenic pump is used to create the vacuum in the chamber by using helium as a refrigerant. The cryogenic temperature has to reach 10.9°K and the vacuum pressure must be at

3.26E-6 Torr before starting the deposition. The total time required to reach that pressure is approximately forty-five minutes.

Thickness Detector

A thickness detector is placed in the chamber to report the deposited thickness, deposition rate, and time remaining. The life expectations of this thickness detector should not be less than thirty percent or else it has to be replaced.

Table 3.3 Cr/Au deposition conditions

Metal	Deposition rate (Å/sec)	Run time (min)	Power %	Thickness (nm)	Read thickness (nm)
Cr	2.9	2	14	40	41.5
Au	30	3.14	30	60	61.3

The process takes place according to the following steps:

1. Load the E-beam recipe by clicking/file-load-E-beam recipe.
2. Make sure that the chamber door is closed.
3. Set the step number to zero.
4. Check that the crayon temperature is below the 20°K.
5. Open the crayon pump knob.
6. Open the chamber. Use the vacuum cleaner to clean the chamber and wipe it with paper.

Place the substrates on the holder and ensure that all the samples can rotate easily.

7. Close the chamber tightly.

8. Press the pump command in the software. Wait for approximately forty minutes for the chamber to be vacuumed.
9. On the chamber machine, press menu-review-process, go to edit-change to change steps, thickness, and depositing material. Correspondingly set step 1, thickness: 40nm, material: chromium and step 2, thickness of 60nm, material: gold.
10. Press status to check the life of the thickness detector, it should be more than thirty percent.
11. If the pressure is around 3.26E-6 torr and the crayon temperature is around 10.9°K. Turn on the power supply and then press the on (green) button so that the deposition will start.
12. After the deposition is complete, wait for approximately fifteen minutes for the material to cool down and then remove the samples.

Table 3.4 Supplementary conditions for Cr/Au deposition

Life of thickness detector	Chamber pressure (Torr)	Vacuum time (min)	Crayon temperature (°K)
69%	6.26E-6	45	11.2

3.2.3.3 Types of Microlithography

As discussed earlier, the samples of the present work were characterized by diameter. As sample diameters decrease, the resolution and accuracy of the process become more crucial and directly affect the developing process. From this point, the samples have been fabricated by two

different lithographic procedures - Ultraviolet and E-beam - in order to meet the required resolution and limitation.

3.2.3.3.1 Ultraviolet Lithography

For fabricating the larger pillars, size ranges from 1-10 μ m diameter, Ultraviolet lithography was applied. The height of the samples should be high enough to ensure that the pillars bear a uniform stress during the compression test. On the other hand, the aspect ratio of the samples cannot be higher than two or three because this makes the pillars buckle at a very low stress.

Since the aspect ratio is a limiting factor in the fabrication of samples thicker than 10 μ m, a common resist such as Az-resist could not be used. Hence the SU-8 25 photo resist (MicroChem Corporation, USA) which could provide a versatile range of thicknesses was used. The SU-8 consists of an epoxy, Epon SU-8, available from Shell Chemicals, a solvent gamma-butyrolactone (GBL) and a photo acid generator - from the family of the Triarylium-Sulfonium salts [66].

SU-8 25 is a negative photo resist which is sensitive to UV light and able to provide sufficient thickness of interest. Due to the cross-linking reaction of the SU-8 epoxy material, it has an excellent mechanical property which limits its roughness.

Since SU-8 is a difficult-to-remove photo resist, a thin layer of Omni coat ingredient, cyclopentanone 70-90%, propylene glycol monomethyl ether 10-20%, proprietary polymer <1%, Proprietarysurfactant <1% (MicroChem Corporation, USA) was spin coated onto the surface prior to the SU-8 coating. A spin coater, model Ws-400A6Npp/Lit Laurell

Technologies Corporation, USA) was applied for spin coating the Omni coat. After this process, the wafers were heated for three minutes at 200°C in a Lindberg/blue Man Del High Temperature Bake Oven (Thermal Product Solution (TPS) Company, USA). This allows for the fast and easy removal of SU-8 during the developing process.

Here are the steps for coating the wafers with Omni coat:

1. Shake the Omni coat solution.
2. Clean the spin coater and holder as well as all the edges.
3. Clean the chips in a dilute acetone, blowing nitrogen gas to dry them. Hold the chips tight.
4. Place the silicon wafer on the chip holder.
5. Press the vacuum button to vacuum hold the wafers.
6. Place 3-4 droplets of Omni coat onto the wafers with a 10 mL syringe.
7. Based on previous experiments in which the device setting could coat 17nm thickness at 4000rpm/sec speed and twenty-second duration. A spin speed of 2000 rpm and duration of twenty seconds should take in approximately 30nm of thickness.

Table 3.5 Omni coat spin coating conditions

Acceleration rate(rpm/sec)	Time (s)	Thickness (nm)	Speed (rpm)
1215	20	30	2000

3.2.3.3.1.1 Spin Coating SU-8

The next step is to spin coat the chips with SU-8. To dispense the SU-8 onto the wafers, a vacuum system dispenser, EFD Ultra 870 Fluid Dispenser, (Nordson Corporation, Canada) was applied. The dispenser is equipped with a control pedal and a different-sized syringe. By setting the pressure to $p=5$ psi, the SU-8 is dispensed onto the chips from a 25mL syringe. The amount of dispensed SU-8 should be enough to coat the surface. Based on the SU-8 data sheets, the best value for a uniform coating is around 1mL per square inch [65].

To spin coat the SU-8, a spin coater, Model Ws-400A6Npp/Lit (Laurell Technologies Corporation, USA) was used. The rotating speed and total spin time was chosen from the SU-8 25 formulation data sheet [65]. The speed has ramped up in order to spread the photo resist more uniformly on the surface.

Table 3.6 SU-8 Spin coating conditions

Acceleration rate (rpm/sec)	Time (s)	Thickness (μm)	Speed (rpm)
1215	10	-	500
1215	30	27	3000

After spin coating with SU-8, the top edge of the chip is removed using a cutter to reveal enough conductive area for the alligator clip in the plating process.

3.2.3.3.1.2 SU-8 Soft Bake

The chips are heated up to 95°C using a hotplate1000-1 (Electronic Micro System Ltd, UK). The soft baking process lets the solvent of the SU-8 evaporate at the surface. As a result, the SU-8 becomes more sensitive to the UV light and also makes the SU-8 stick firmly to the substrate. Over-baking the samples will stiffen the SU-8 in such a way that developing it becomes difficult.

Baking SU-8 on the hotplate is important because the heat will increase from bottom to top, in contrast with the oven where a firm surface layer will form prior to the bottom parts therefore the solvent cannot escape at the surface. The temperature ramp will slow down the solvent evaporation, which improves the quality of surface and resists adhesion [65].

Table 3.7 SU-8 soft bake Conditions

Temperature (°C)	Time (min)
65	3.30
95	5.30

3.2.3.3.1.3 Chromium Photo Mask

To pattern the SU-8 resist, its surface is exposed to Ultraviolet light through a photo mask. Because the black-and-white spectrum of opaque material in the chromium mask gives a superior patterning resolution when compared with an emulsion mask, the chromium photo mask

was preferred over the emulsion photo mask, even though its fabrication equipment was unavailable at UW.

The original pattern of the mask was designed using the Corel Draw software and then sent out to the University of Alberta for fabrication. Figure 3.4 illustrates the design pattern of chromium mask ranging from 1-40 μm diameter size, corresponding to the size of the pillars.

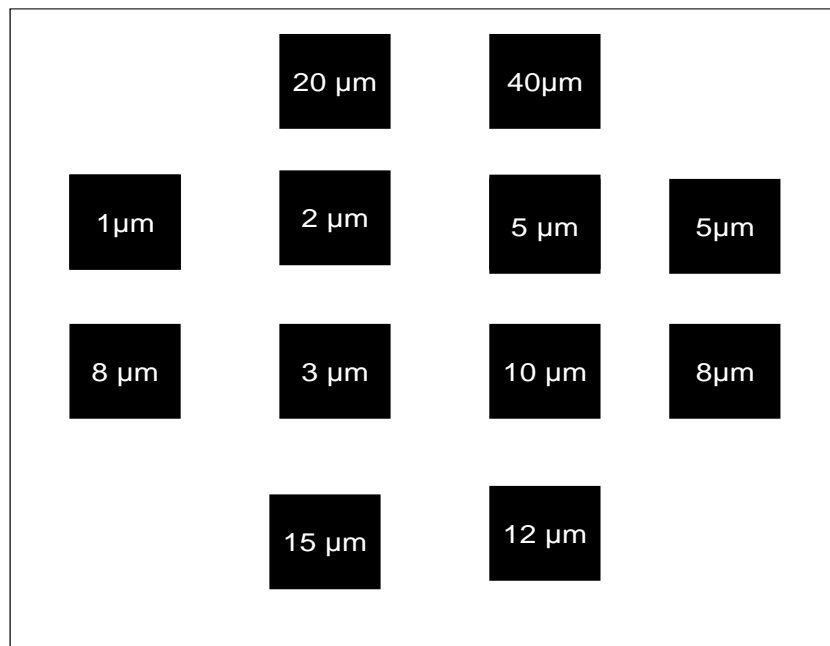


Figure 3.4 Schematic over view design of chromium mask fabricated at University of Alberta

Chromium Photo Mask Batches

Each of the illustrated black patterns on the chromium mask contains circular shape patterns whose diameter corresponds with the diameter of the pillars and the controlling surface

pattern for electroplating. The schematic of the patterned batches on the Cr - mask is shown in the Figure 3.5.

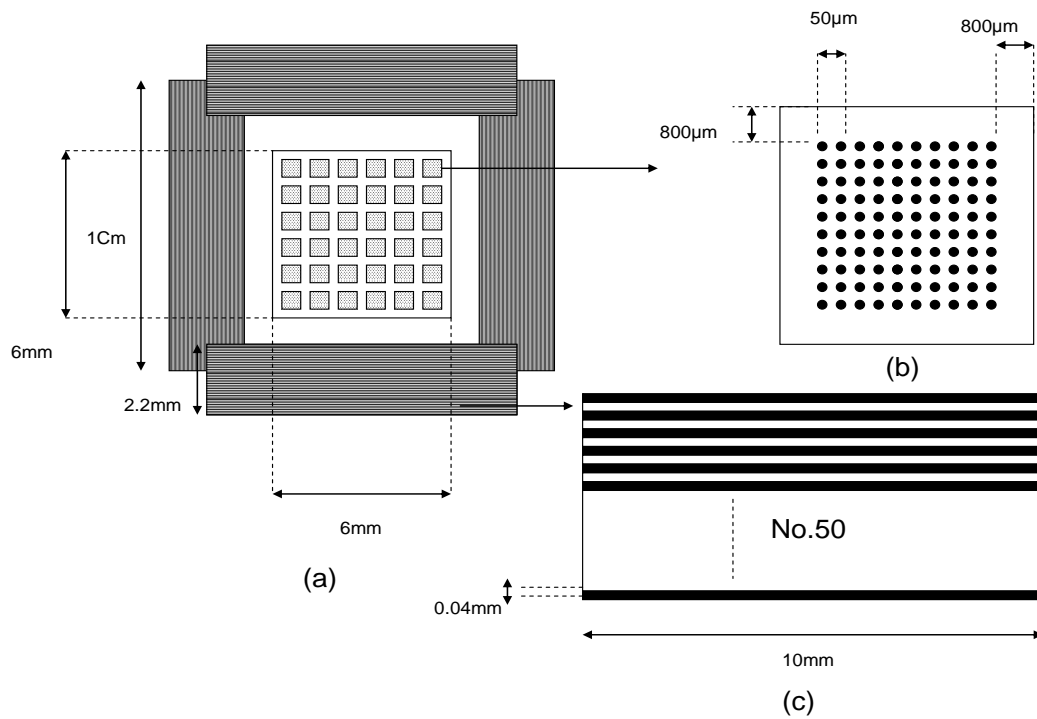


Figure 3.5 (a) Schematic of 0.5 μm photo mask on chromium mask (b) batch of 0.5 μm circular pattern (c) controlling surface pattern

As illustrated in Figure 3.5, the pitch patterns' centre-to-centre distance is 50 μm. The controlling surface in the edge side was designed in an array form of 0.4 mm x 10 mm. There are

fifty arrays each side. The total number of circular pattern batches is thirty-six, each of which have one hundred circular patterns.

3.2.3.3.1.4 Ultraviolet Exposure on SU-8 Resist

SU-8 is patterned by exposing Ultraviolet light through a chromium photo mask. In SU-8 as a negative photo resist, the exposed parts will be insoluble in the SU-8 developer.

An Oriel mask aligner (Newport Corporation, USA) was used for exposing Ultraviolet light. This aligner is equipped with a 500W ultra-filtered mercury lamp with 41 mW/cm² intensity. The optimized dosage of 1800 mJ/cm² was discovered experimentally through trial-and-error. During this process, glycerol was injected into the gap between the photo mask and the wafers to improve the quality of patterning. A brief explanation of its effect will be provided in the following chapter.

Here are the steps for exposing the UV light in the aligner:

1. Place the Cr mask in the photo mask holder and fasten it.
2. Cut a piece of a blank Mylar and place it on the substrate wafer holder where the chips will be placed; this will prevent vacuum leakage.
3. Place the chip in a manner to be aligned with the desired pattern on the chromium mask. This can be done either manually or by the aligner adjustments.
4. Dispense four or five drops of glycerol with a 3 ml syringe.
5. Adjust the mask on the chips. Fasten it firmly until the glycerol spread on chip surfaces.
6. Vacuum the mask with a vacuum pressure of ~5 inHg.
7. Place the mask holder under the UV lamp.
8. Place i/liner filters to filter the wavelength below 360 nm.

9. Set dosage to 1800 mJ/cm² and expose UV light
10. Spin coat chips in the spin coater at 2500 rpm for twenty seconds to remove the glycerol from the SU-8 surface.

3.2.3.3.1.5 SU-8 Post-exposure Baking

Post-exposure baking on a hot plate will promote a cross-linking reaction in the SU-8 polymer resin. Since SU-8 is a negative photo resist, the cross-linking polymers will not be soluble in the SU-8 developer. The temperature ramp is preferred in order to reduce stress and cracking [65].

Table 3.8 SU-8 post exposure bake conditions

Temperature (°C)	Time (s)
65	3.5
95	6.5

3.2.3.3.1.6 Developing SU-8

Following the post-exposure bake, samples will be left to cool for fifteen minutes and then placed in SU-8 developer at room temperature. Developing time is relative to the SU-8 thickness. For a 30 μm photo resist thickness the most favorable time was six minutes.

Shorter developing time did not fully etch away the SU-8 from the surface, as illustrated in Figure 3.6.

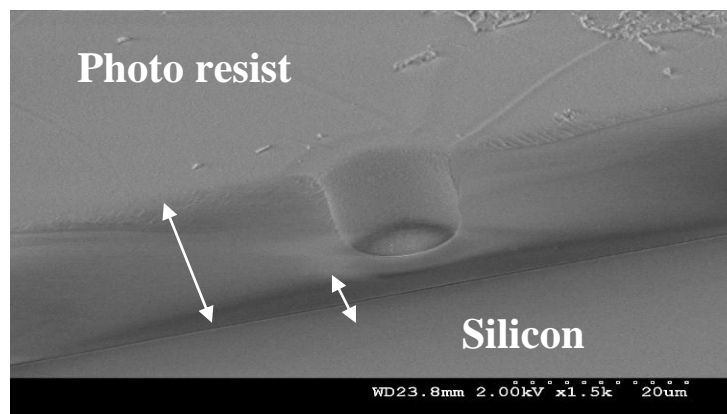


Figure 3.6 SEM image of a SU-8 holes side wall, developed for less than 6 min

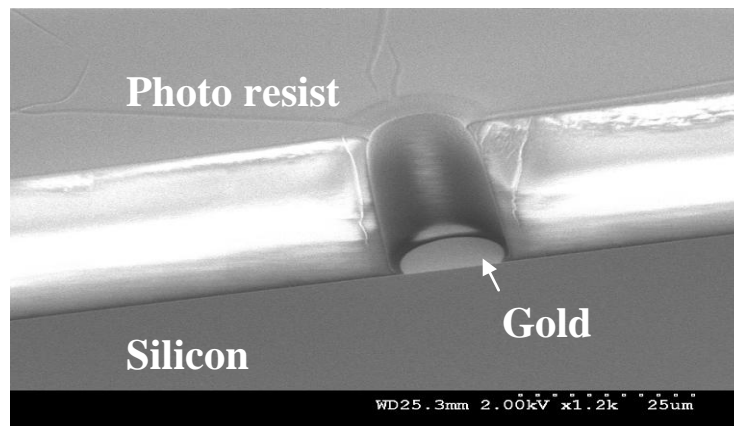


Figure 3.7 SEM image a SU-8 holes side wall, developed for 6 min

After patterning the SU-8, the Omni-coat was etched from the surface by oxygen plasma etching using a Trion Orion plasma-enhance chemical vapor deposition (PECVD) system (Trion Technology, USA). The total applied time was sixty to ninety seconds at inductive coupled plasma (ICP) of 20 watts, reactive ion etch (RIE) of 20 watts, pressure of 20mtorr, oxygen flow of 40 sccm, and RIE reflect of 3 watts.

Figure 3.8 illustrates the SEM image of the controlling surface and Figure 3.9 illustrates the patterned area in the UV lithography micro-mold chips.

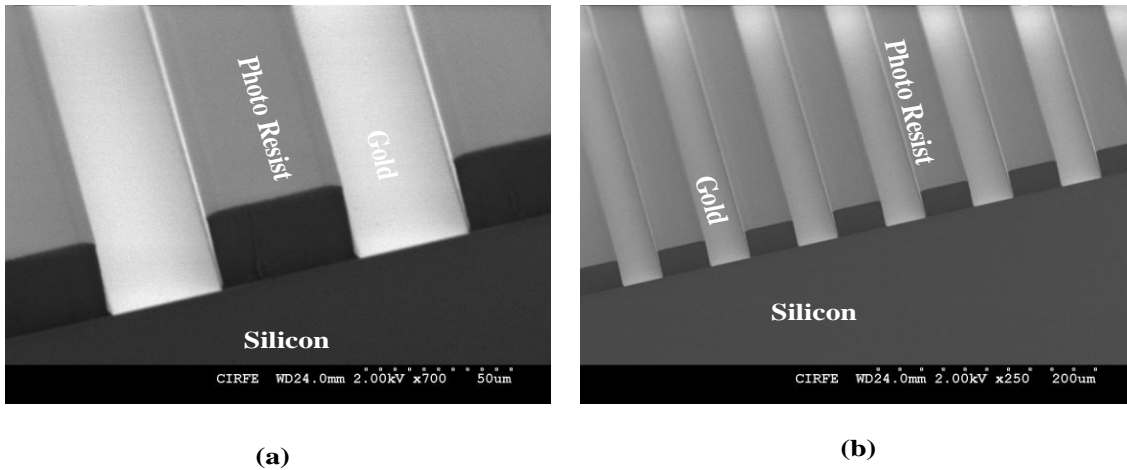
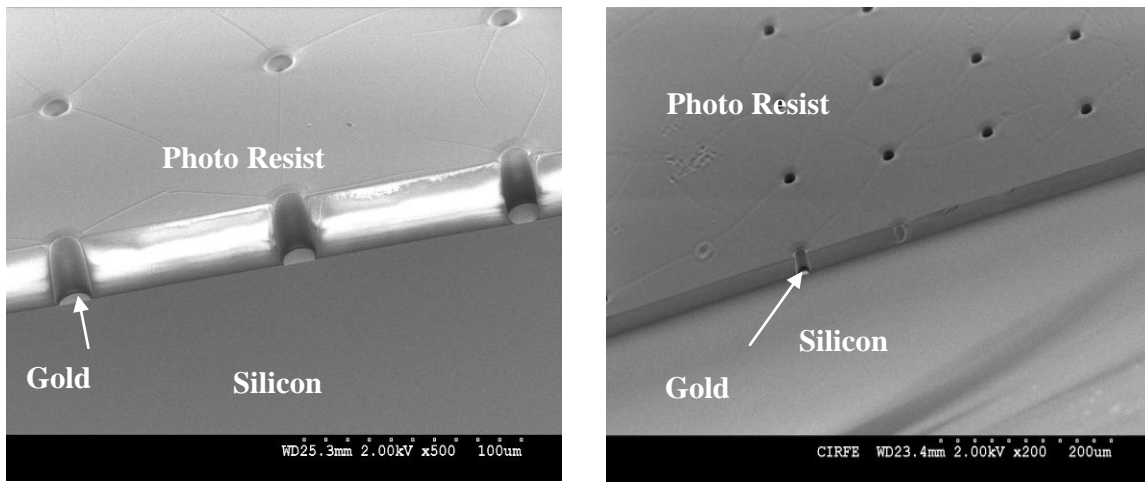


Figure 3.8 (a-b) SEM image of controlling surface side wall on a UV-micro-mold chip



(a)

(b)

Figure 3.9 (a-b) SEM image of holes side wall on a UV Micro-mold chip

3.2.3.3.2 E-beam Lithography

During the fabrication of 100nm to 1 μ m diameter holes, E-beam lithography with a high-resolution lens system to pattern the photo resist was used. Since E-beam lithography is a maskless form of lithography, the problem of light diffraction caused by the inevitable gap between the photo mask and the resist is resolved. Patterns are written directly onto the resist, which will result in nm-resolution patterning.

The design of patterns for E-beam lithography were made using design CAD software and were written on the resist surface using NPGS software.

To fabricate the E-beam samples, the fabrication process was divided into two steps: (A) patterning the controlling surface, and (B) patterning the pillar growth section.

1. Patterning the Controlling Surface

As the controlling surface can be patterned easily via simple lithography procedure, the E-beam micro-mold chips were first designed with controlling surfaces and were then processed with E-beam writing. Here are the overall steps in patterning the controlling surface of E-beam micro-mold chips:

1. Coat the gold chips with photo resist
2. Pattern the photo resist using photolithography through an emulsion photo mask
3. Develop the photo resist
4. Etch the gold/chromium
5. Strip the photo resist

Figure 3.10 shows these steps schematically.

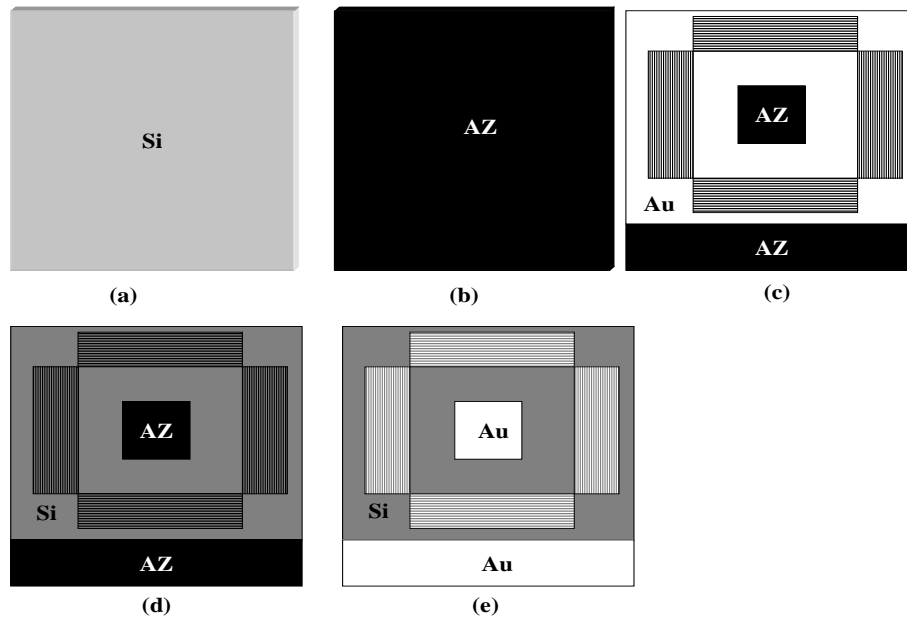


Figure 3.10 (a-e) Steps for patterning the controlling area using an emulsion mask a) blank gold chip b) AZ-photo resist coating c) patterning controlling area d) gold and chrome etch e) striping the resist to reveal the gold surface for the next step.

2. Patterning the Pillar Growth Site

The controlling surfaces will be taped and E-beam photo resist which is PMMA 950 KMW A4 (MicroChem Corporation, USA) will be spin coated on the surface. Patterns will be written onto the photo resist using E-beam lithography as the steps have been illustrated in Figure 3.11.

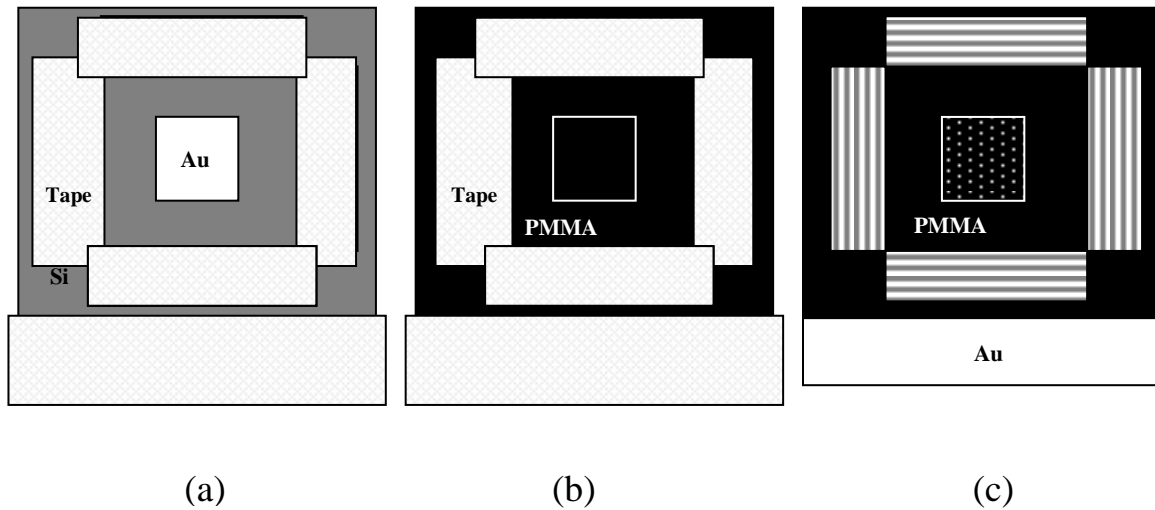


Figure 3.11 Schematic steps in fabrication of pillar growth site: a) tapping the controlling surface, b) spin coating PMMA, c) writing the patterned area with E-beam

3.2.3.3.2.1 Emulsion Photo Mask

In order to pattern the controlling surface wafers, an emulsion mask was utilized instead of a chromium mask since fabrication facilities were available on campus and because the array pattern was large enough that the emulsion mask resolution provided good-quality patterning. The original design of the mask was designed using the Corel Draw software and contained the controlling surface with a diameter similar to those of the chromium mask, 0.4 x 10 mm. The only difference was that the number of total arrays was sixty instead of fifty. Figure 3.12 illustrates a schematic of the emulsion mask.

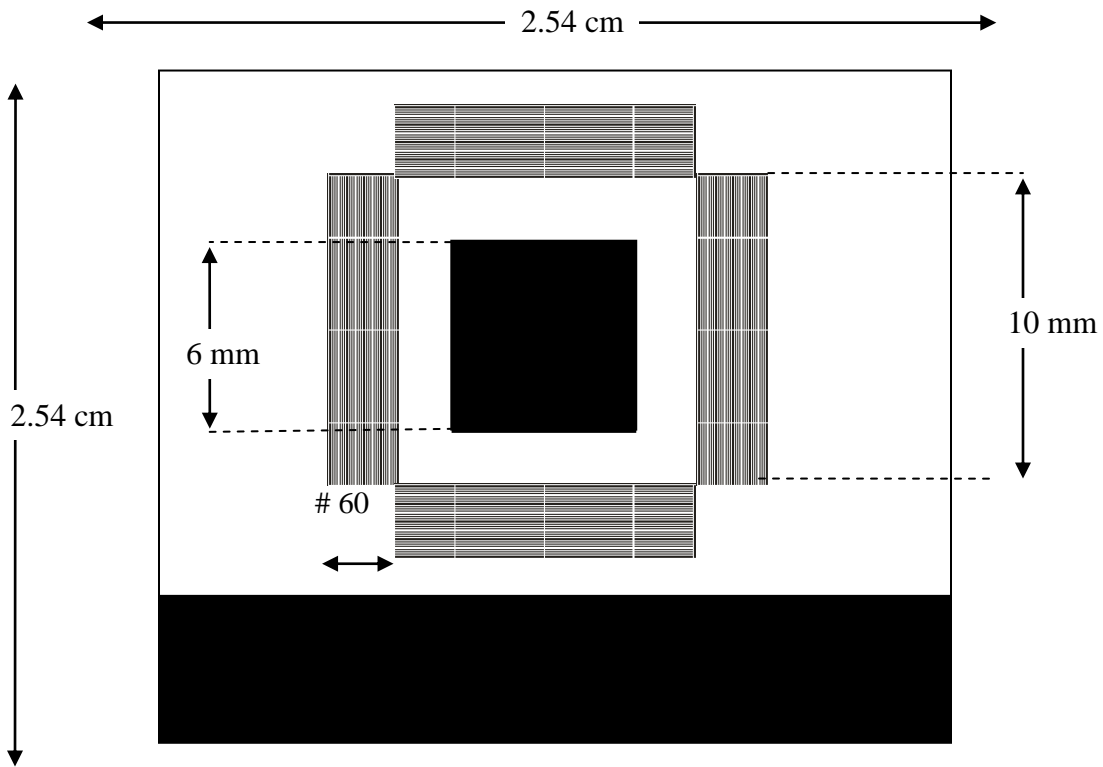


Figure 3.12 Schematic of emulsion mask

The emulsion mask, an AGHD high-definition photo plate mask, with a high-contrast silver halide, (Micro Chrome Technology, USA) was patterned using a 10x Mylar sheet. The schematic design of the Mylar sheet is illustrated in Figure 3.13.

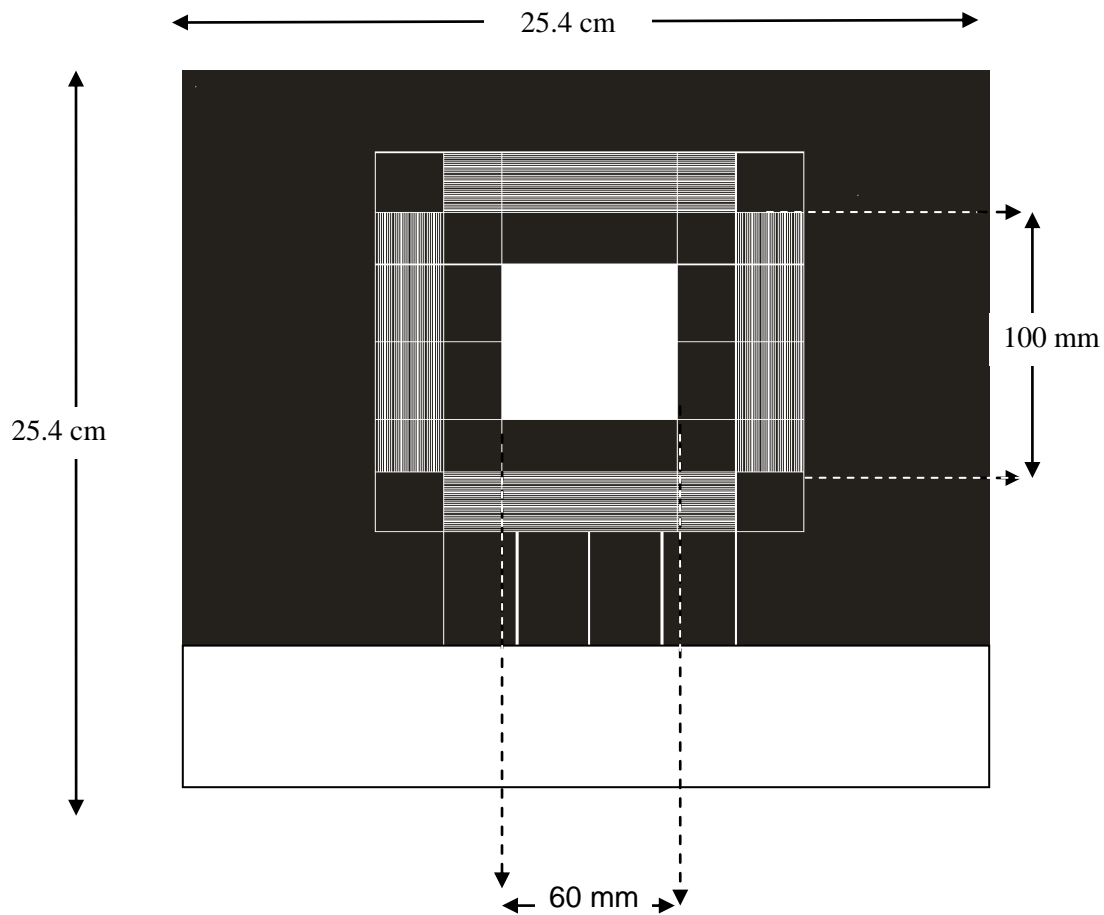


Figure 3.13 Schematic of mylar design

Emulsion Mask Fabrication

White light was exposed through the Mylar sheet in the UW dark room. A twelve second exposure time was controlled by the equipment timer. Since the emulsion masks are highly-sensitive to white light, it is important to ensure that there is no white light contamination during the procedure. The procedure for fabricating the emulsion mask was as follows:

1. Place the Mylar sheet on the bottom holder.

2. Prepare the developing solution in 4:1 mixture of de-ionized water/developer solution (640 ml DI water/160 ml developer)
3. Prepare the fixer solution in a 4:1 mixture of DI water/fixer (640 ml de-ionized water /160 ml of fixer solution)
4. Ensure that there is no white light contamination and remove the emulsion mask
5. Place the emulsion mask in a photo mask holder
6. Expose to light for 12 seconds
7. Develop the mask for 3 minutes and 30 second with 5 seconds of dry time for every 25 seconds of developing
8. Rinse the mask with DI water for 3 minutes
9. Submerge the mask in the fixer solution for 3.5 minutes with 5 seconds of dry time for every 25 seconds of fixing.
10. Rinsing the mask with DI water

Both the developer and fixer solutions are from Micro Chrome Technology, USA. Agitation was applied during the developing and fixing process and the entire procedure was carried out at room temperature.

3.2.3.3.2.2 Coating Gold Chips AZ Photo Resist

For patterning the controlling area with the emulsion mask, an AZ 3330 positive photo resist (AZ Electronic Materials, USA) was dispensed onto chips using an Ultra 870series EFD dispenser (Nordson Corporation, Canada). This resist is thermally stable up to 125°C and coats the surface smoothly. AZ photo resists are widely used in industry. The resist was spin coated in a Model Ws-400A-6Npp/Lit spin coater (Laurell Technologies Corporation, USA) at 4000 rpm for 45 seconds to take in 2.3µm thickness. The samples are then soft-baked at 90°C for 5 minutes on an EMS Precision Electronic Hot Plate Model 1000-1 (Electronic micro system ,UK) followed by exposure through the emulsion photo mask to the UV light in the Oriel mask aligner (Newport Corporation, USA) with a 500W unfiltered mercury lamp with a nominal 41 mW /cm² power density.

The exposure time of twenty seconds, based on previous research experience in the lab, was applied. The samples received post-exposure to improve the cross-linking reaction in the photo resist, thus increasing its resistance to higher temperatures from reflowing. The optimum post-exposure baking time for the samples was one minute at 110°C.

An AZ 300 MIF developer (AZ Electronic Materials, USA) was used to develop the resist. The developing time was found through a trial-and-error process. Although sixty seconds of developing time is sufficient for a fresh developer solution, it was found that older developers may require developing times up to ninety seconds.

The AZ photo resist in this step basically covers the gold surfaces on the controlling area where the indium will be deposited on the gold surface of the pillar growth site (middle part),

and also the edge part of the chips where the alligator clip will conduct the electricity during the plating procedure, as shown in Figure 3.14. The remaining chromium/gold surface was etched away until the silicon substrate was revealed.

For etching the Cr/Au surface, chips are submerged in the gold etchant, type TFA (Transene Company, USA), for ten seconds and then the wafer is submerged in the Chromium Etchant Type 1020 (Transene Company, USA) for another 20-25 seconds. The native silicon oxide will form on the silicon substrate at room temperature and will act as a resist for indium deposition during the electro-deposition process. Having patterned the chip surface with AZ photo resist, the chips are submerged in AZ-Stripper, Kwik stripper (AZ Electronic Materials, USA) for at least fifteen minutes. The covered gold surface was then exposed for the next process, as shown in Figure 3.14.

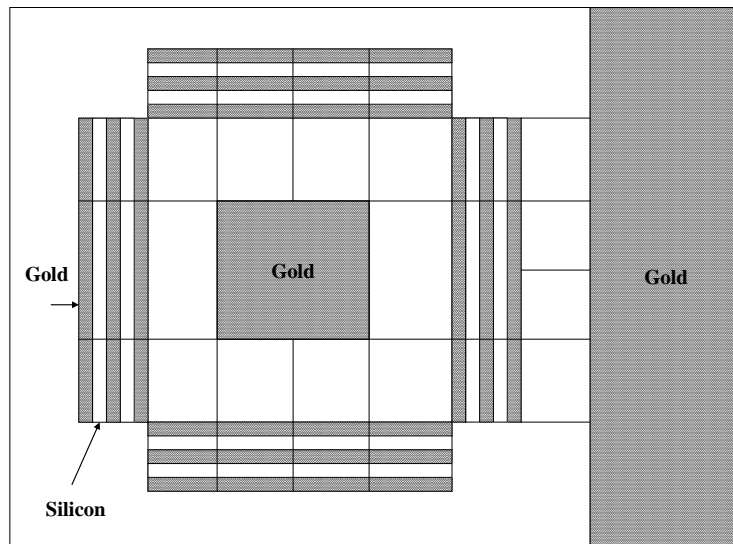


Figure 3.14 Schematic of categorized area using the UV lithography

The steps for patterning the controlling surfaces are as follows:

1. Place a needle on top of the AZ (3330) photo resist syringe and fill the needle with the pedal of the resist dispenser to expel any bubbles.
2. Mount the wafer and the press vacuum in the spin coater.
3. Gently apply the resist to the wafers and close the lid.
4. Set the spin coater to 4000 rpm and spin coat the sample for 45 seconds at a 1215 rpm/sec acceleration rate.
5. Bake the sample on the hotplate at 90°C for 5 minutes.
6. Change the mask aligner (holder) and/or the wafer holder, if necessary.
7. Mount the mask. Turn on the mask vacuum to hold it securely.
8. Align the sample and close the lid. Ensure that they are in good contact. Turn on the chamber vacuum and place the sample under the shutter.
9. Set the timer to 20 seconds at $41\text{mW}^2/\text{m}^2$ intensity
10. Turn off the chamber vacuum
11. Bake the patterned samples on the hotplate at 110°C for 1 minute.
12. Use AZ MIF 300 developer to develop. Pour the developer into the labeled beaker and prepare DI water. Place the samples into the developer for approximately 70-80 seconds and then into DI water for 5-10 seconds. Wash them with DI water and dry them.
13. Check the samples under a microscope to verify whether or not the AZ has been fully developed.
14. Place gold and chromium etchant into designated beakers and DI water into a DI water beaker. Place the samples in the gold etchant for about 10 seconds, then into the DI water, then the chromium etchant for 25 seconds and finally into the DI water.
15. Dry the samples and examine them under the microscope to ensure that the gold and chromium have been fully etched away from the arrays.

16. Place the wafers in warm (60°C) Kwik stripper for ~15 minutes.
17. Wash the samples with DI water.
18. Blow dry the samples with nitrogen gas.

3.2.3.3.2.3 Oxygen Plasma Etch

After stripping the AZ photo resist from the surface, the wafers are oxygen plasma etched to remove any possible AZ residue. A Trion Orion PECVD System (Trion Technology, USA) was used with RIE power of 50 watts, ICP power of 50 watts, pressure of 20mtorr, oxygen flow of 40 sccm, and RIE and ICP reflect of 4 watts. The detailed procedure for performing the oxygen plasma etches with different conditions is discussed below

3.2.3.3.2.4 PMMA Photo Resist Coating

E-beam lithography was applied for higher-resolution patterning. Poly methyl methacrylate (PMMA) 950 KMW A4 (MicroChem Corporation, USA) was applied as E-beam resist. PMMA is a positive resist that contains a special poly methyl methacrylate grade to provide high-contrast and high-resolution patterns in the processes [67]. Since fabrication facilities for E-beam lithography were not available on campus, the chips were sent to the University of Western Ontario to be processed there. The wafers were spin coated for 3 seconds at 500 rpm and the speed was then ramped up to 1500 rpm and spun for an additional 1 minute. The sample was then vacuum baked at 50°C for 10min. The second layer of PMMA was spin coated similarly. The thickness of the resist for creating 250 nm pillars is measured to be 750nm.

3.2.3.3.2.5 E-Beam Writing on PMMA

The pillar site was written on the resist using NPGS software and an appropriate E-beam dosage. Pillar site design is illustrated in Figure 3.15, which shows that the total number of pillar batches was 225, upon each of which 16 pillar growing sites were situated. Each of these batches was identified by an address according to its location. The diameter corresponded with the pillar diameters. The center-to-center distance of the cavities was $50\ \mu\text{m}$.

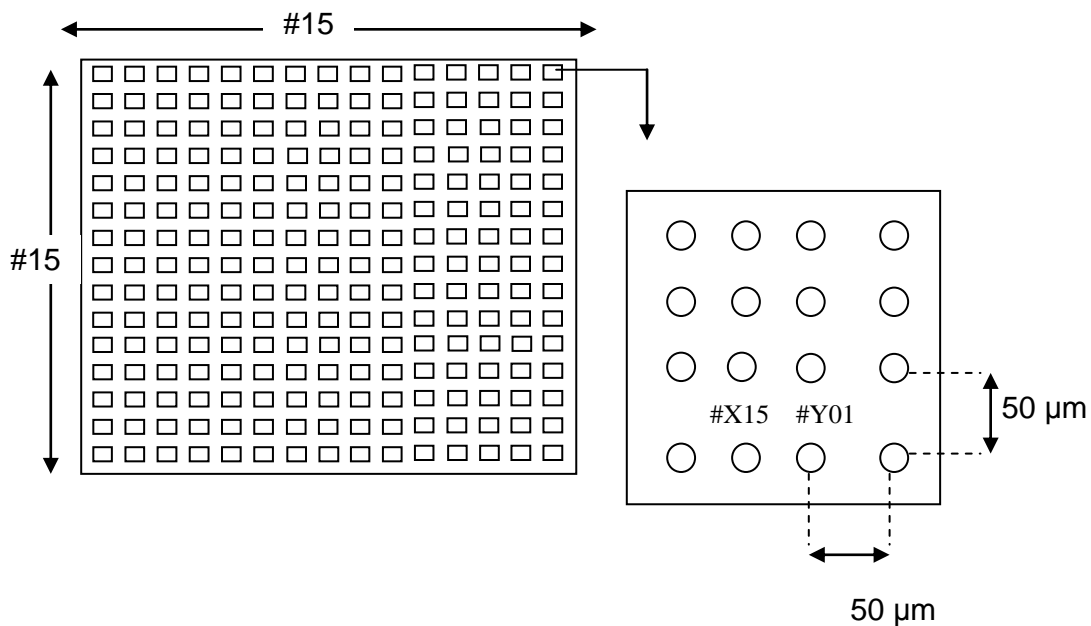


Figure 3.15 Schematic design of the pillar growth site

A range of E-beam dosages from 50% to 254% were applied in 0.9% increments of $500\ \mu\text{C}/\text{cm}^2$. Writing started at the (1,1) location with the lowest dose and followed a serpentine path to (1,14), (1,15), (2,15), (2,14), (2,13), and so on. The size of the circular pattern was 250 nm, as demonstrated in Figure 3.16.

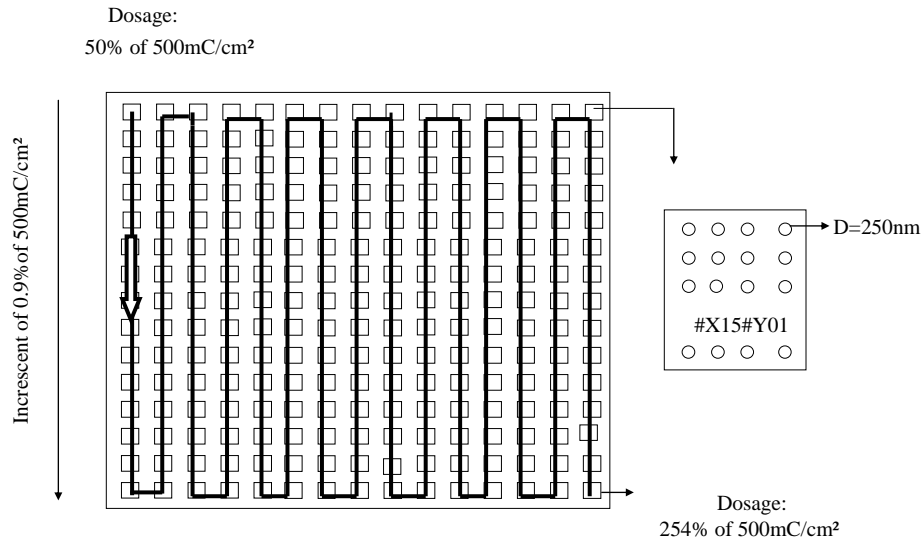


Figure 3.16 E-Beam write map with the applied dosage in each location.

Having the pattern written on the PMMA, the tapes were removed and the wafers were baked at 180°C for 90 seconds.

3.2.3.3.2.6 Developing PMMA

PMMA was developed in three steps. While the wafers were spun at 500 rpm, the resist was developed in a 1:3 mixture of methyl isobutyl ketone (MIBK) and isopropyl alcohol (IPA) in an atomized spray developer for 90 seconds before being rinsed with IPA spray for sixty seconds, and then blown dry with nitrogen gas.

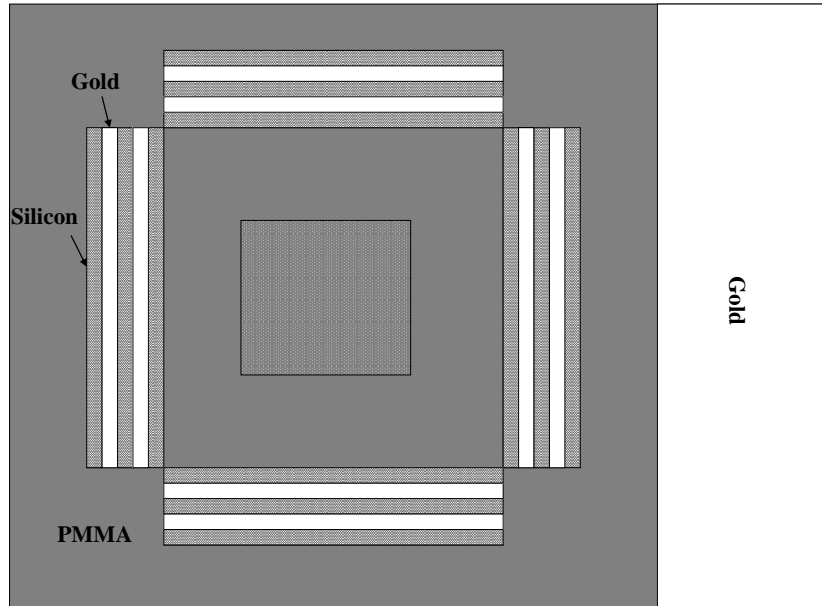
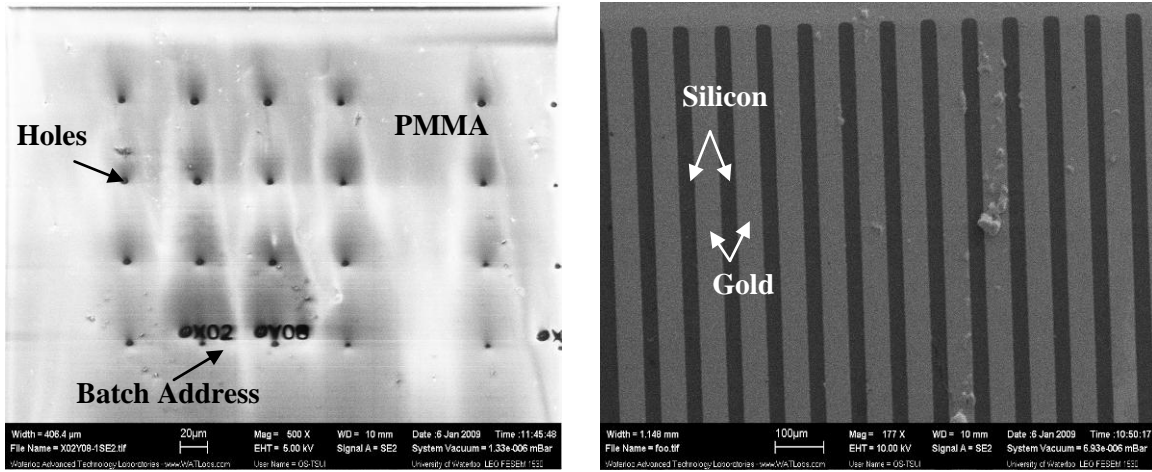


Figure 3.17 Schematic of overall design of the E-beam micro – mold chip



(a)

(b)

Figure 3.18 (a-b) SEM image of processed E-Beam micro-mold chip: (a) Pillar growing site (b) controlling surface

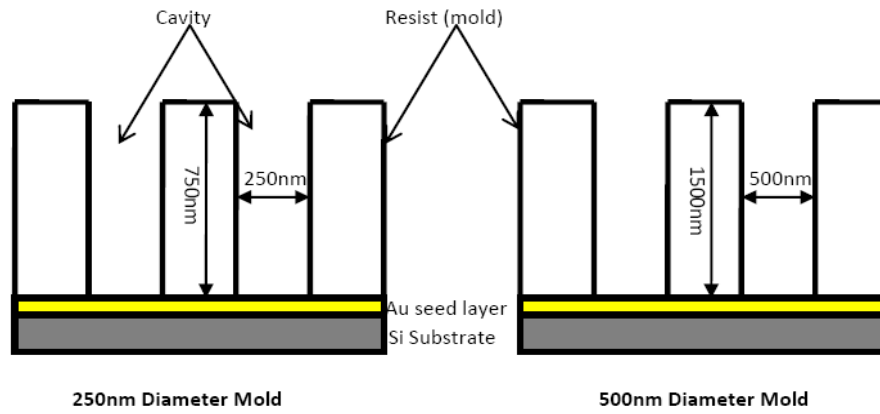


Figure 3.19 Schematic of the side wall mold design

3.2.3.3.2.7 Oxygen Plasma Etching

The fabricated micro-mold chips were etched with oxygen plasma to ensure that the PMMA residues were fully removed from the gold surface. It is important to use an appropriate etching rate to ensure that the written photo resist is not etched in the process. By testing a range of etching rates under different conditions, the best etching rate was calculated to be approximately 100 nm /min. The samples were etched for fifteen seconds in 20 watt RIE and 0 watt ICP with 102 mtorr pressure and 40 sccm oxygen flows.

The steps of the etching process were as follows:

1. Prepare isopropyl alcohol and acetone in glass Petri dishes.
2. Use a cotton swab to clean the edge of the gold chip where it is patterned to control the current. This is an important process to eliminate residues that were created from tapes prior to spin coating.
3. First, apply acetone on a cotton swab and then carefully wipe one edge of the pattern. Do this for the other three edges. Then use isopropyl alcohol to wipe the edges. This process requires extreme caution because it is easy for either of the solutions to contaminate the pillar growing site and remove the patterned PMMA.
4. Before placing the gold chip into the Trion Phantom Reactive Ion Etcher (RIE) machine, the chamber must be cleaned with oxygen.
5. Click on “Cancel” when the screen is on “Stand By” mode.
6. Press the “Manual Process Control” button on the screen.
7. Turn the vacuum on. After 5 minutes, set the pressure to 20 m Torr RIE power to 50 watts, ICP power to 50 watts, and gas flow of oxygen to 40 sccm. Turn on the pressure.
8. After 20 seconds, turn on the gas.
9. When the pressure and the gas flow are stabilized, turn on the plasma (RIE and ICP).

10. Use the knobs on the bottom of the machine to adjust RIE reflected power. Attempt to reduce the reflected power to less than 10% of the applied power.
11. Adjust the ICP reflected power using the knobs on top of the machine. Also try to make it less than 10% of the applied ICP power.
12. When the ICP and RIE powers are settled, increase the ICP power by 50 watts and wait until it is settled. Increase it again by 50 watts to 200 watts.
13. Apply the mentioned conditions for about 300 seconds and then turn off the plasma. Wait 30 seconds.
14. Turn off the gas. After 30 seconds, turn off the pressure.
15. The pressure to 102mtorr, ICP to 0watts, and RIE to 20 watts for a 100nm/min etching rate.
16. Turn on the pressure and repeat steps 8 to 11. Leave it for 30 seconds.
17. Turn off the plasma and then the gas. Wait 30 seconds. Turn off pressure and vacuum.
18. Exit from manual process control and click on "Vent Chamber."
19. When the chamber lid opens, use a paper towel to clean the edge of the chamber. Place the sample on the middle.
20. Press "Close Lid" on the screen.
21. Go to manual process control then turn on the vacuum and the pressure.
22. Repeat steps 8 and 9.
23. Ensure that the reflected RIE and ICP power are low and then apply 15 seconds for etching.
24. Repeat steps 16 to 18 to turn off the machine.
25. When the chamber lid opens, carefully remove the sample.
26. Press "Close Lid" and then "Stand-by Mode" on the screen.

3.2.3.4 Electroplating

Once the gold surface is revealed holes, indium is electrodeposited in a sulfamate plating bath that contains $(\text{NH}_2\text{SO}_3)_3$, NaNH_2SO_3 , HNH_2SO_3 , NaCl , Dextrose Triethanolamine [28], (Indium Corporation, USA). Because electroplating produces fine-grained microstructures, future annealing of electrodeposited indium is essential for producing single-crystal samples. Since plating a smooth surface is desirable, a variety of DC current densities ranging from 0.1 mA- 2 mA were tested using a dummy gold chip with an area of 25mm^2 . The most favorable current density was found to be $1.041\text{ mA}/\text{cm}^2$, at which smoothness was reasonable and at the same time deposition was carried out in an acceptable range. The deposition rate at this current density was calculated to be $83\text{ nm}/\text{min}$.

A Bk Precision power supply (Test Path, USA) was applied for plating. In order to manually control the current with higher precision, a 3Ω resistor and an ammeter were connected in series into the circuit. Figure 3.20 shows the DC circuit that was applied.

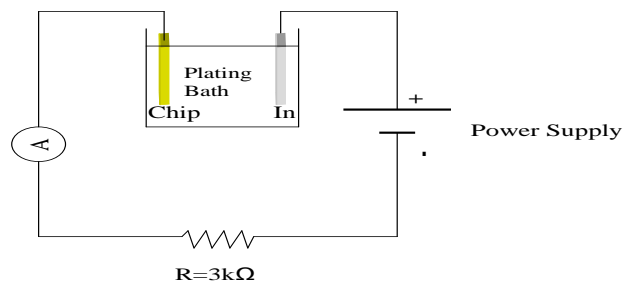


Figure 3.20 Schematic of DC circuit

The anode is an indium bar sized 4 cm x 15 cm and the cathode is a micro-mold chip sized 2.54 cm x 2.54 cm. The chip plating was carried out at room temperature according to the following process:

1. Pour 200ml of indium plating solution into a 250 mL beaker and use a magnetic stirrer to stir the bath at a constant speed.
2. Connect the gold chip as the cathode and indium bar as the anode.
3. To verify whether or not plating actually occurs and also if all of the connections are stable, a current density of $1.041\text{mA}/\text{cm}^2$ is applied to a dummy gold chip for 2 to 3 minutes.
4. Connect an alligator clip to the bottom of the gold chip where the gold surface is revealed. Place the gold chip into the solution and ensure that only the gold pad and patterned edges are in the solution.
5. Use the sonication machine to insert the indium plating solution into the patterns. This process is critical to ensure that plating occurs inside the pattern. Do this for at least 3 minutes while also agitating the chip in the solution during sonication.
6. Connect the gold chip to the cathode side of the power supply and connect the indium as the anode.
7. Apply the appropriate time of plating.
8. Turn off the DC power supply and magnetic stirrer. Pour de-ionized water into a Petri dish and insert the gold chip sample for 5 minutes.
9. Remove and blow dry the sample.
10. Inspect the gold chip under a microscope to see if it is well-plated.

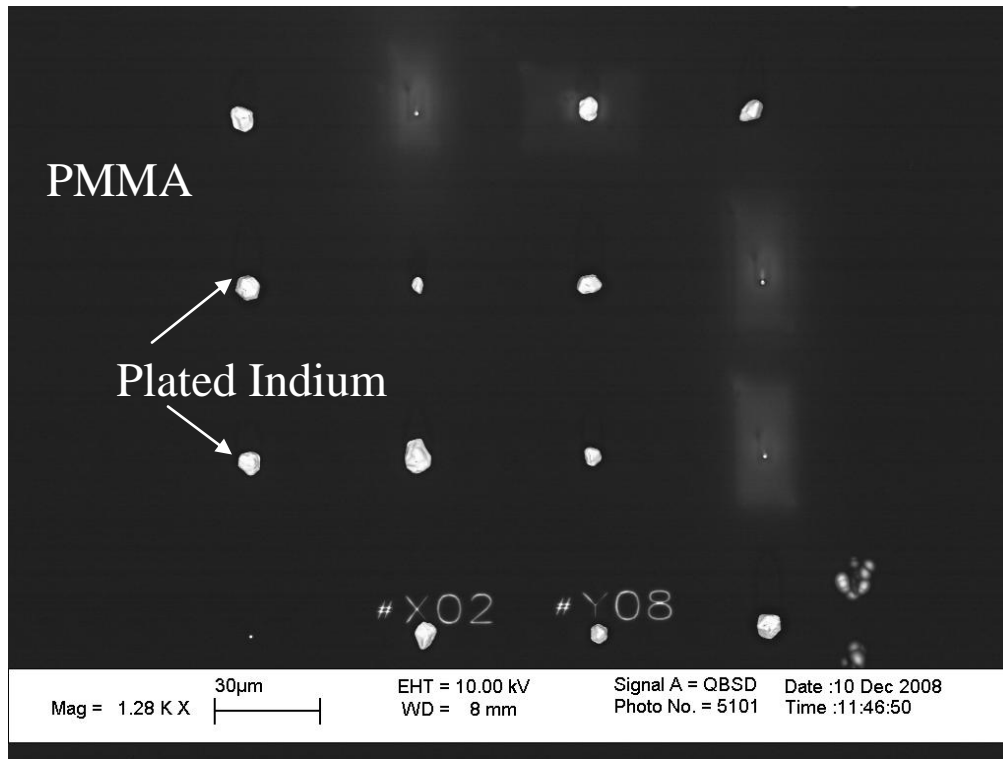


Figure 3.21 SEM image of one of the pillar site batches in E- beam micro-mold chip samples

3.2.3.5 Stripping Photo Resist

The photo resist will be stripped away from the surface after growing the indium pillar. The total time taken for stripping the samples should be sufficient to fully remove the photo resist; three days was found to be enough. A NanoTm Remover PG (MicroChem Corporation, USA) was used for stripping the SU-8 and a Kwik stripper (AZ Electronic Materials, USA), was used for stripping the PMMA.

The steps for stripping the photo resist after plating are as follows:

Stripping the SU-8 from the UV-lithography samples:

1. Pour the PG remover solution into a beaker.
2. Place the UV-lithography-processed chip into a holder.
3. Heat the beaker to 60°C in a sonicator.
4. Place the holder in the beaker.
5. Leave it for 48 hours.
6. Using extreme caution, remove the gold chip using tweezers. This must be done very carefully since the pillars are very fragile and even a small amount of quick movement can break them.
7. Pour isopropyl alcohol (99.7%) into a Petri dish and place the sample in very carefully. Leave it in there for at least 5 minutes.
8. Remove the gold chip very carefully and use the Kim wipes to dry the edges of the gold chips and let the gold pad where pillars are air dry.

Stripping PMMA from E-Beam lithography samples:

1. Pour the Kwik Strip solution into a Petri dish and insert the sample. Close the lid and leave it for at least 48 hours.
2. Using extreme caution, remove the gold chip using tweezers. This must be done very carefully because pillars are very fragile and even a little bit of quick movement can break them.
3. Pour isopropyl alcohol (99.7%) into a Petri dish and insert the sample very carefully. Leave it in there for at least 5 minutes.
4. Remove the chip very carefully and use the Kim wipe to dry the edges of the gold chips and let the gold pad where pillars are air dry.

3.3 Some of the Fabricated Pillars

The following section lists some of the fabricated pillars with their corresponding plating conditions.

Table 3.9 Plating condition for the UV-10 μ m micro-mold

Current (mA)	Area (mm²)	Voltage (v)	Duration (min)	Deposition rate (nm/min)	Height μm
0.5	44	1.56	240	83	20

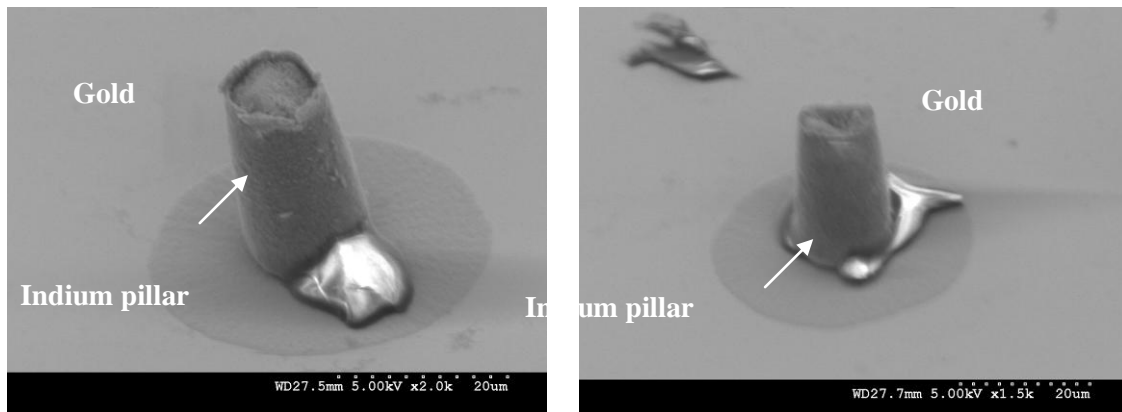


Figure 3.22 SEM images of 10 μ m pillars

Table 3.10 Plating condition of the E-Beam-500nm micro-mold

Current (mA)	Area (mm²)	Voltage (v)	Duration (min)	Deposition rate (nm/min)	Height μm
0.5	48	1.56	10	83	1.5

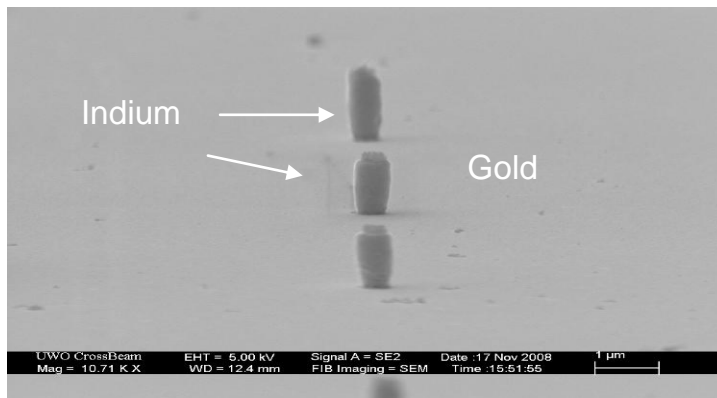


Figure 3.23 SEM image of plated pillar diameter 0.5 μm height of 1.5 μm

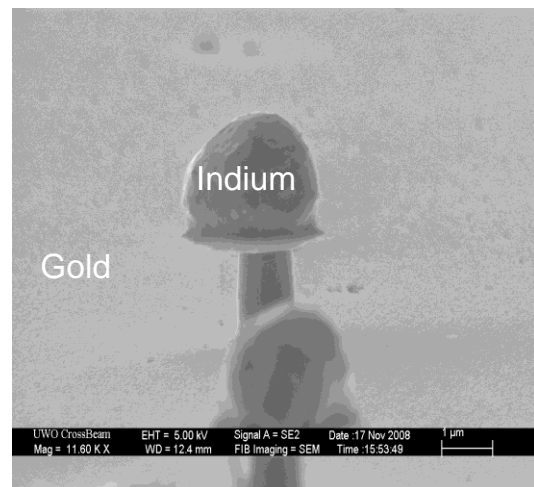
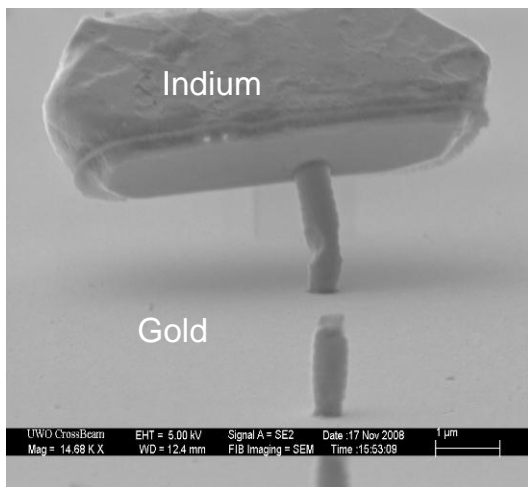


Figure 3.24 SEM image of the 0.5 μm plated indium. [10min deposition time was high so the over plating indium forms these mushrooms

Table 3.11 Plating condition for E-Beam-250nm micro-mold

Current (mA)	Area (mm²)	Voltage (V)	Duration (min)	Deposition rate (nm/min)	Height (μm)
0.5	48	1.56	6.5	83	0.75

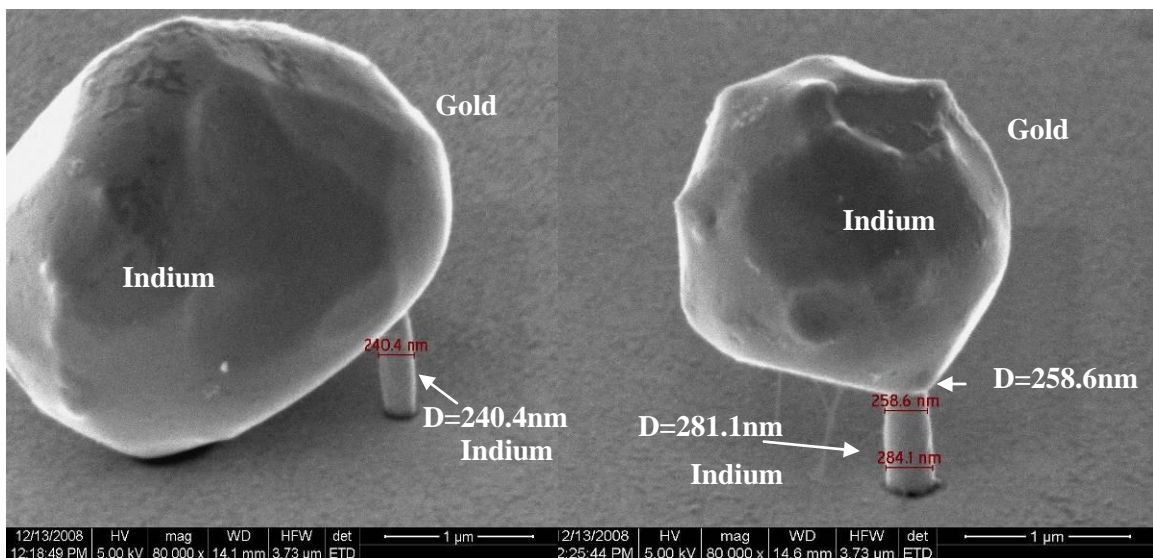


Figure 3.25 SEM image of 250 nm indium pillar

As can be seen in the Figure 3.25, the deposition duration was far higher than that required, and the samples were over-deposited. On the other hand, giving a lower deposition time prevented any plating from occurring on the chips. The application of a high current density of 10.41 mA /cm² for 3.5 seconds improved indium pillar formation. The result of the applied condition is illustrated in Figure 3.26.

Table 3.12 Plating condition for E-beam-250 micro-mold

Current (mA)	Area (mm²)	Voltage (v)	Duration (s)	Height (μm)
1.5	48	4.52	3.5	-
0.5	48	1.5	510	0.75

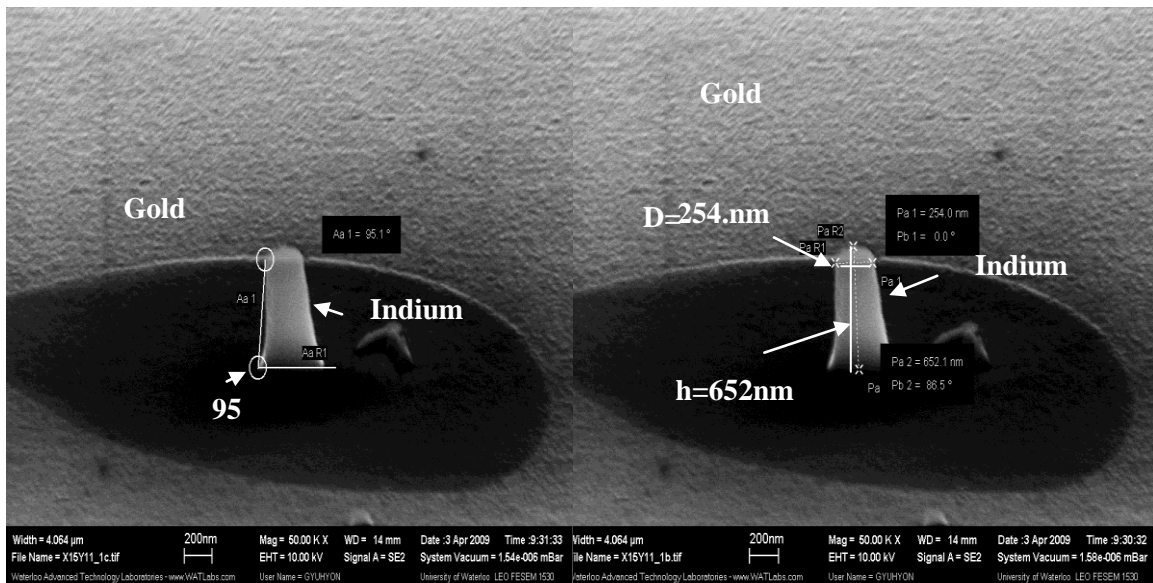


Figure 3.26 SEM images of 250nm fabricated pillars

Chapter 4

Result of Micro-Lithography Fabrication

4.1 Introduction

Two basic techniques for fabricating submicron-size indium pillars were discussed in the previous chapter. The current chapter will present the scope of fabrication results and the effects of various factors on process development. The best-known method of fabricating 250 nm pillar samples will be presented also.

4.2 Effect of Ultraviolet Dosage

SU-8 is transparent photos resist which is not sensitive to UV light above 400 nm, however, it absorbs wave lengths below 350 nm. Figure 4.1 shows the absorbance of different SU-8 thicknesses ranging from 10-50 μm .

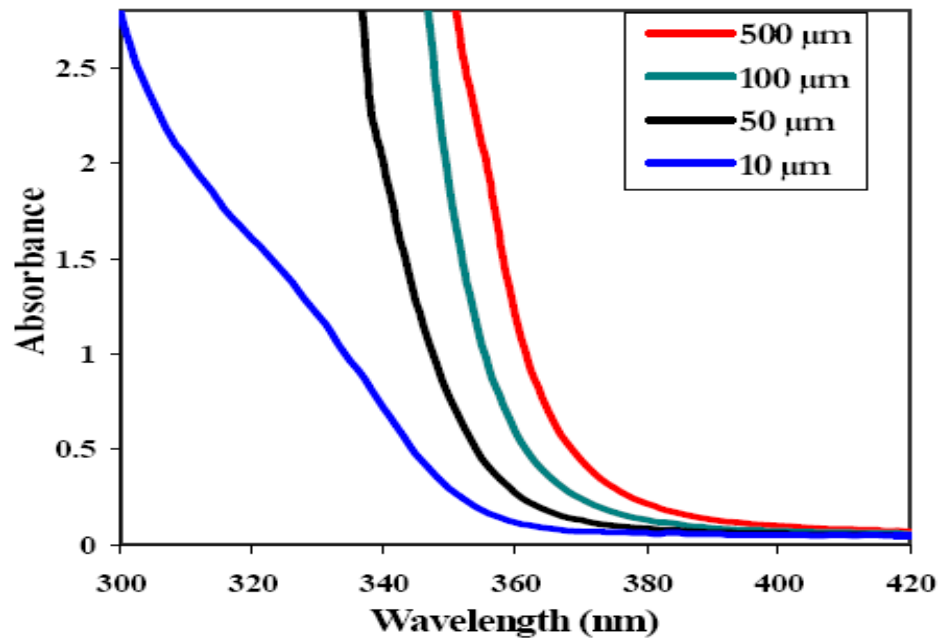
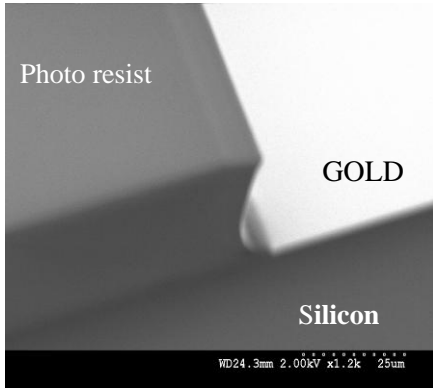
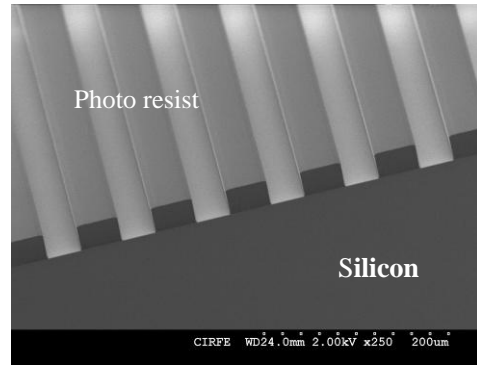


Figure 4.1 Different film thicknesses of SU-8 absorbance vs. UV wavelength, reproduced from [65]

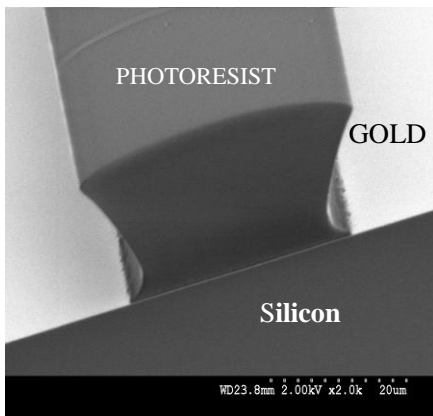
By applying an excessive dosage of UV below the 350 nm wavelength, the top part of the photo resist is overexposed. As a result, the side wall is embroidered negatively or T-topping will be formed, as illustrated in the (a) and (b) of Figure 4.2.



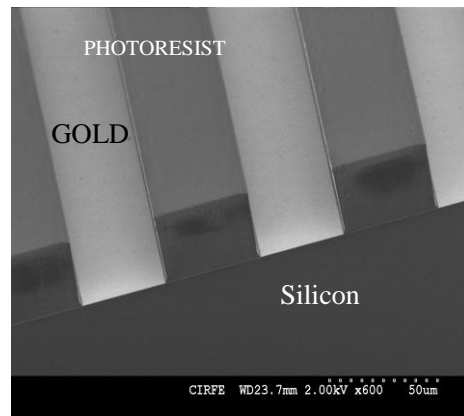
(a)



(c)



(b)



(d)

Figure 4.2 ((a)-(d)) SEM image of fabricated mold (a) – (b) dosage 1000 mJ/cm^2 , (c)-(d) dosage 1800 mJ/cm^2

By testing a range of dosages and exposure times as well as by using an i /liner filter which filters out UV light below 360 nm, the T-topping was resolved as illustrated in the (c) and (d) of Figure 4.2.

Figure 4.3 illustrates the improvement of the side walls as well as the appearance of the holes by varying the exposure time and applying I/liner. As can be seen, the applied mask and the size of the holes are indicated.

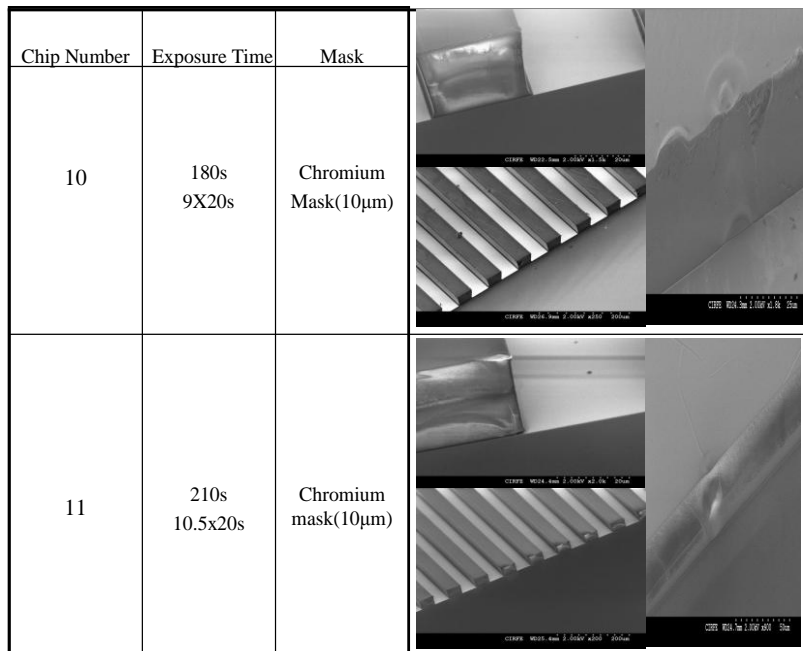


Figure 4.3 SEM image of the side wall as well as the holes on the micro-mold chip according to the applied condition

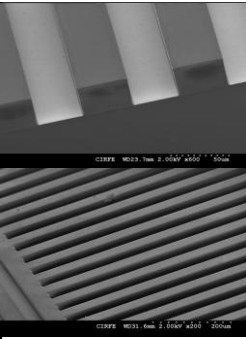

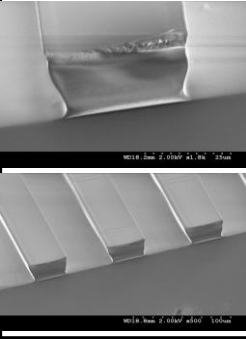
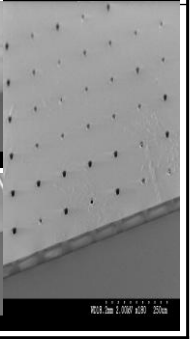
Chip Number	Exposure Time	Mask	SEM Image	
8	240s 4X60s	Chromium Mask(10μm)		
14	210s 3.5x60s	Chromium mask(15μm)		

Figure 4.4 SEM image of the side wall as well as the holes on the micro-mold chip according to the applied condition

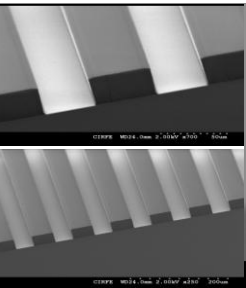
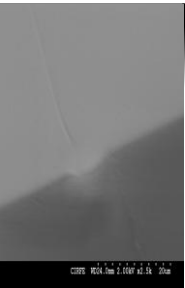
Chip Number	Exposure Time	Mask	SEM Image	
9	360s 6X60s	Chromium Mask(10μm)		
14-1	100s 5x20s	Chromium Mask(15μm)	Su-8 got developed thoroughly	
15-1	120s 6x20s	Chromium Mask (15μm)	Su-8 got developed thoroughly	

Figure 4.5 SEM image of the side wall as well as the holes on the micro-mold chip according to the applied condition

The clean room's alignment failed to operate during the development process and a new aligner had to be used. This device was equipped with a set-up for dosage and so future experiments were followed by varying dosages. A series of dosages from 1000 to 2000 mJ/cm² were tested and the optimum dosage was found to be 1800 mJ /cm².

4.3 Effect of Air Gap between the Photo Mask and Photo Resist

As illustrated in Figure 4.6, the photo resist was bumped on top of the holes after being developed in the developer during the initial attempts at the fabrication of micro-molds.

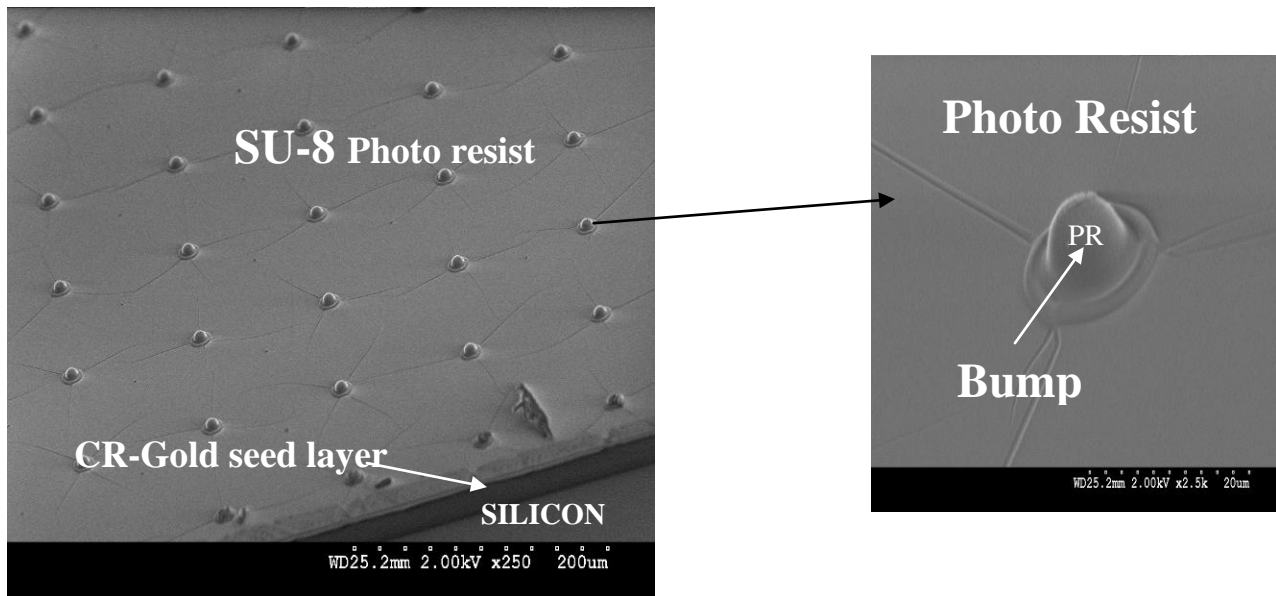


Figure 4.6 SEM image of developed 10 μm chip after post exposure bake

The appearance of bumpy surfaces can be explained by the inevitable air gap between the photo mask and thick photo resists. The uneven thickness of the photo resist surface introduces air gaps between the photo mask and resist, which result in pattern deformation. Thick photo resists usually suffer from uneven thickness due either to beading at the border of the wafers during spin coating or surface tension variation along the surface, which causes non-uniformity during the soft bake process. The air gap causes Fresnel diffraction, which is the key phenomenon in side wall enlarging during UV lithography printing [69]. The air gap causes the angle of the exposed UV light to deviate to the unwanted area that was covered by a black pattern on the photo mask, as illustrated in Figure 4.7, so some cross-linking reaction takes place on these surfaces.

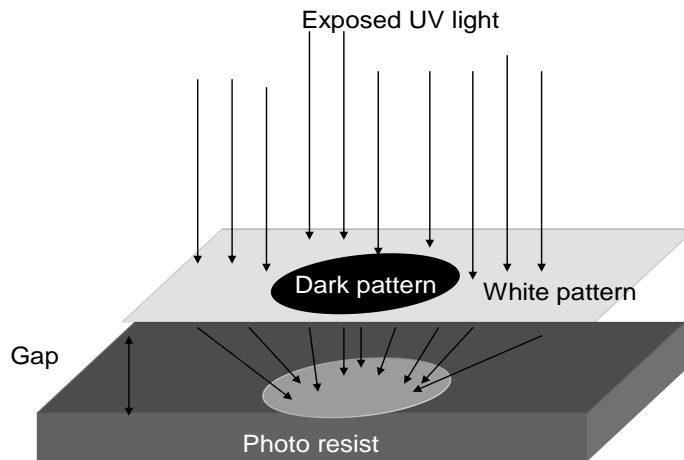


Figure 4.7 Schematic illustration of UV-light deviation due to the air gap

Some problems arise during the post-exposure bake since the exposed and unexposed areas have different thermal expansion coefficients; the area with the higher expansion coefficient will expand more in correspondence with the deeper unexposed photo resist during the post-exposure bake and the photo resist will take on a bumpy-shaped form. The exposed and unexposed parts are shown in Figure 4.8.

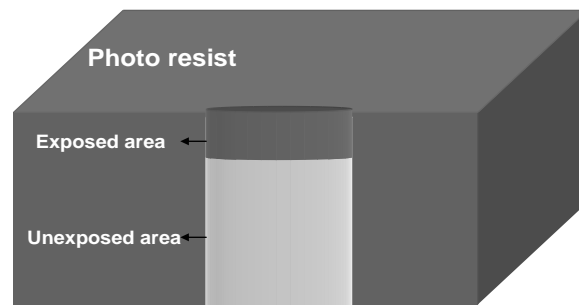


Figure 4.8 Schematic illustration of photo resist exposed and unexposed area under photo-mask black patterns

As illustrated in Figure 4.9, reducing the air gap between the photo mask and the resist will cause the intensity distribution of the Fresnel diffraction to get closer to the intensity

distribution of the perfect contact. This will directly improve the UV light exposure process and the straightness of the side walls [69].

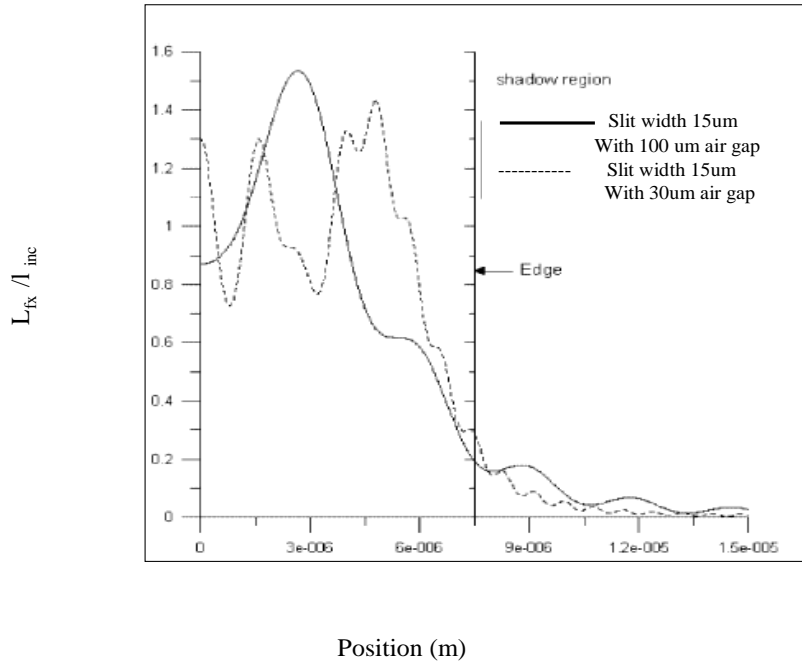


Figure 4.9 Intensity distribution of Fresnel diffraction for different air gap thickness: L_{fx} Fresnel diffraction intensity, L_{inc} intensity of incident vs. the photo mask distance from photo resist surface, reproduced from [69]

To reduce the gap between the resist and the photo mask, the gap was filled with a glycerol ($C_3H_8O_3$). As glycerol has a reflection index of 1.4729 at 20°C, which is close to the mask glass reflection index of 1.474 at 20°C, it will fill the air gap and improve side wall patterning. Figure 4.10 shows that the Fresnel diffraction has improved by injecting the glycerol into the gap.

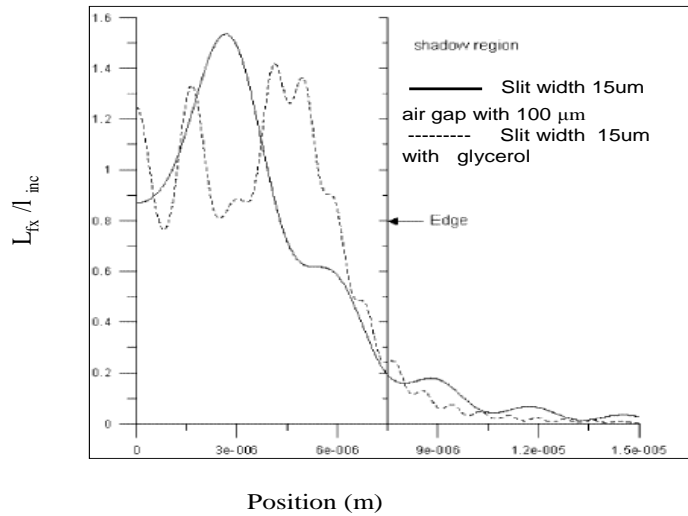


Figure 4.10 Intensity distribution of Fresnel diffraction before and after injecting Glycerol: L_{fx} Fresnel diffraction intensity, L_{inc} intensity of incident vs. the photo mask distance from photo resist surface, reproduced from [69]

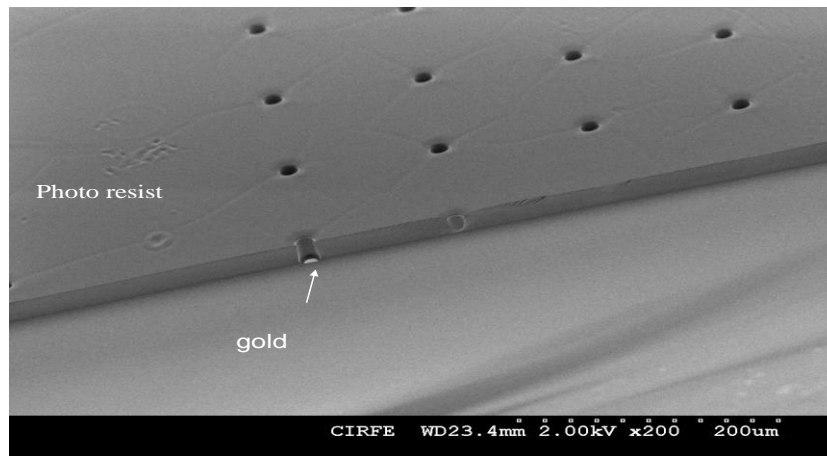


Figure 4.11 SEM image of developed micro-mold side wall after Glycerol inject

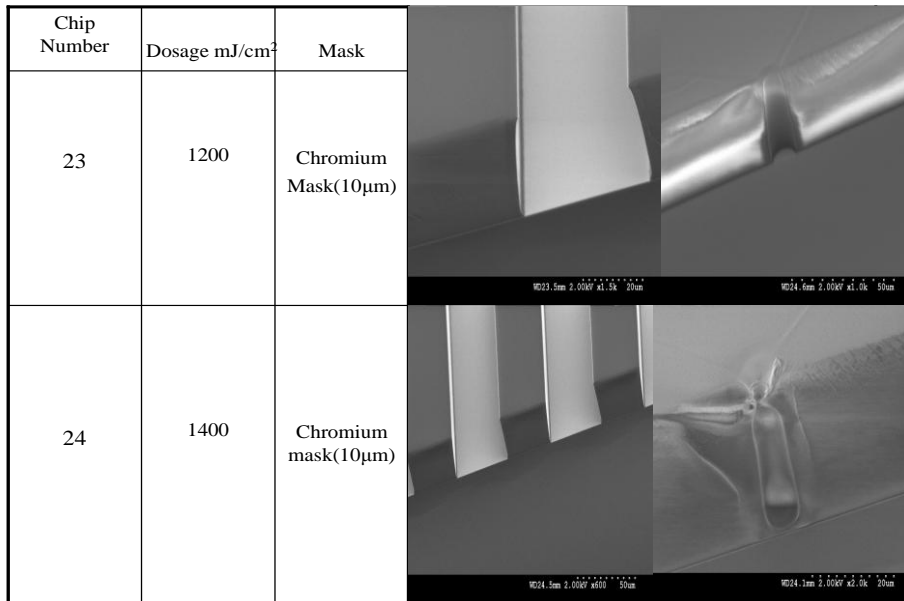


Figure 4.12 SEM image of micro-mold side wall corresponding to the applied condition, before Glycerol inject

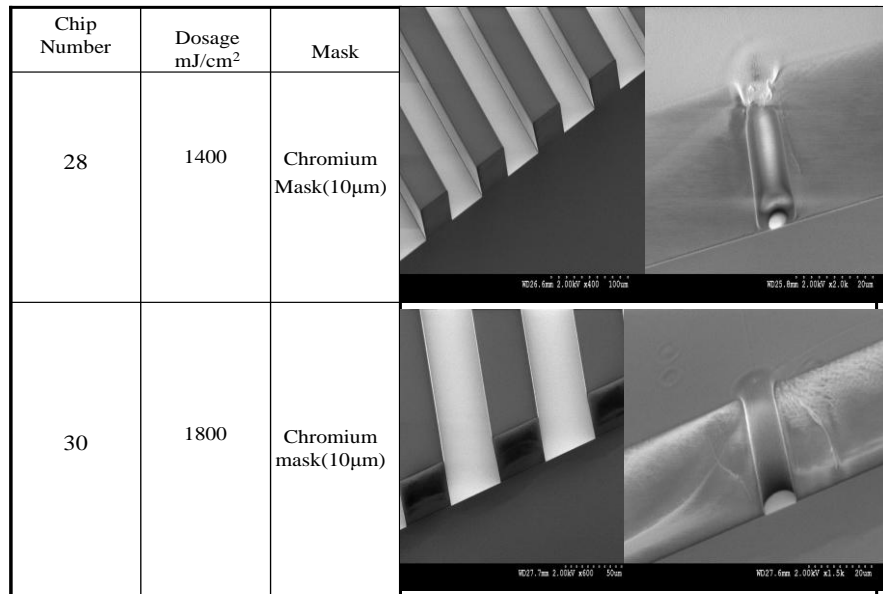


Figure 4.13 SEM image of micro-mold side wall corresponding to the applied condition, after Glycerol inject

4.4 Pulse Plating

Pulse plating experiments were conducted during the plating process. As indicated in many experiments [55-59], the morphology of the deposited material can be improved by using pulse plating. Pulse plating improves mass transport, which has an important influence on deposition rate and deposition properties. By applying the pulses during pulse plating, the ion concentration in the solution is controlled more efficiently than in DC plating. During the period in which the cathode current is applied, the reactant ions are plated onto the cathode due to the reduction reaction. During the off period, or anodic current, the plated ion species are refilled either by the transport phenomena that convey more ions from the bulk solution or by dissolution of the dendrites which have low stability in the solution [68].

The Potentiostat model EPP4000 (Princeton applied research, USA) was used. In conventional DC plating, only current density is a changeable variable, while in pulse plating at least three different parameters, such as the on-time, off-time, and peak current density, can be changed.

There are basically two types of wave form that have been tested by potentiostat. The first approach was to give a negative and positive pulse and the second was to just give a peak pulse in order to nucleate the deposition followed by application of a constant current.

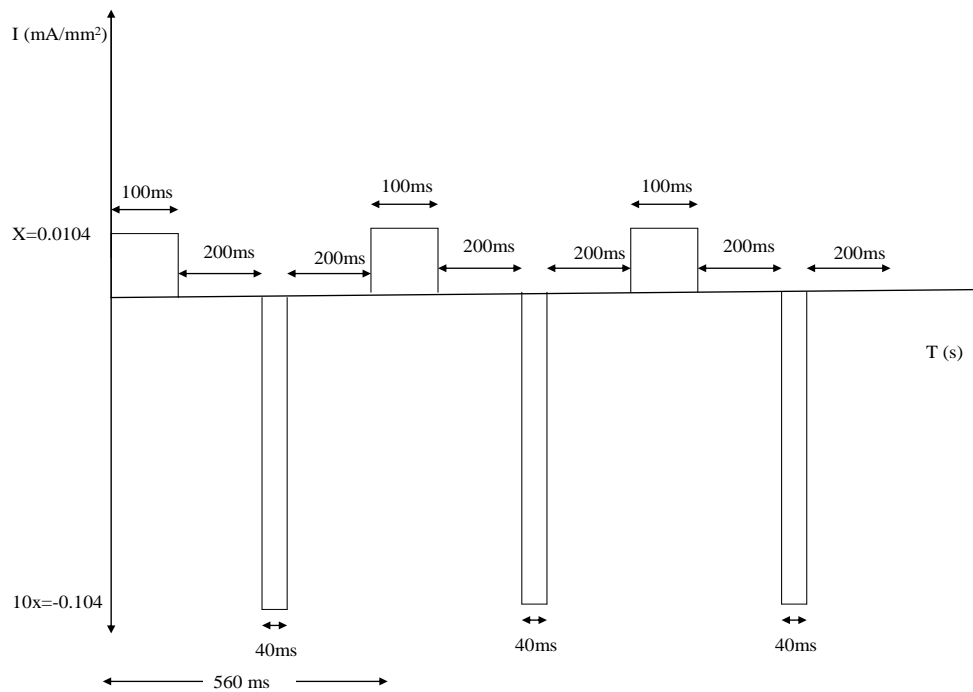


Figure 4.14 Applied pulse plating wave form current density vs. time

The dummy gold samples were dissolved into the solution during the testing of gold chips through the application of the wave form illustrated in Figure 4.14. During the second tested wave form, a range of peak periods from 0.2-1 seconds were applied to verify the best condition for high-quality deposition. From plating the gold dummy chips, the most favorable peak time turned out to be 0.2. Figure 4.15 illustrates the mentioned wave form.

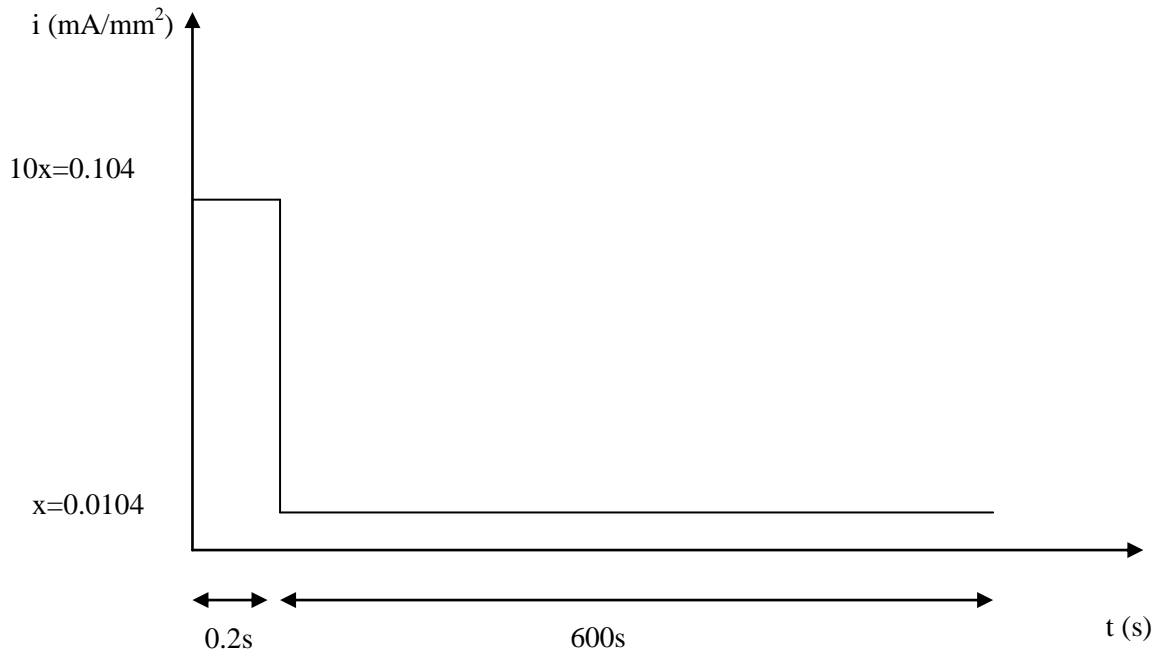


Figure 4.15 Favored wave form for plating the micro-mold chips using potentiostat current density vs. time

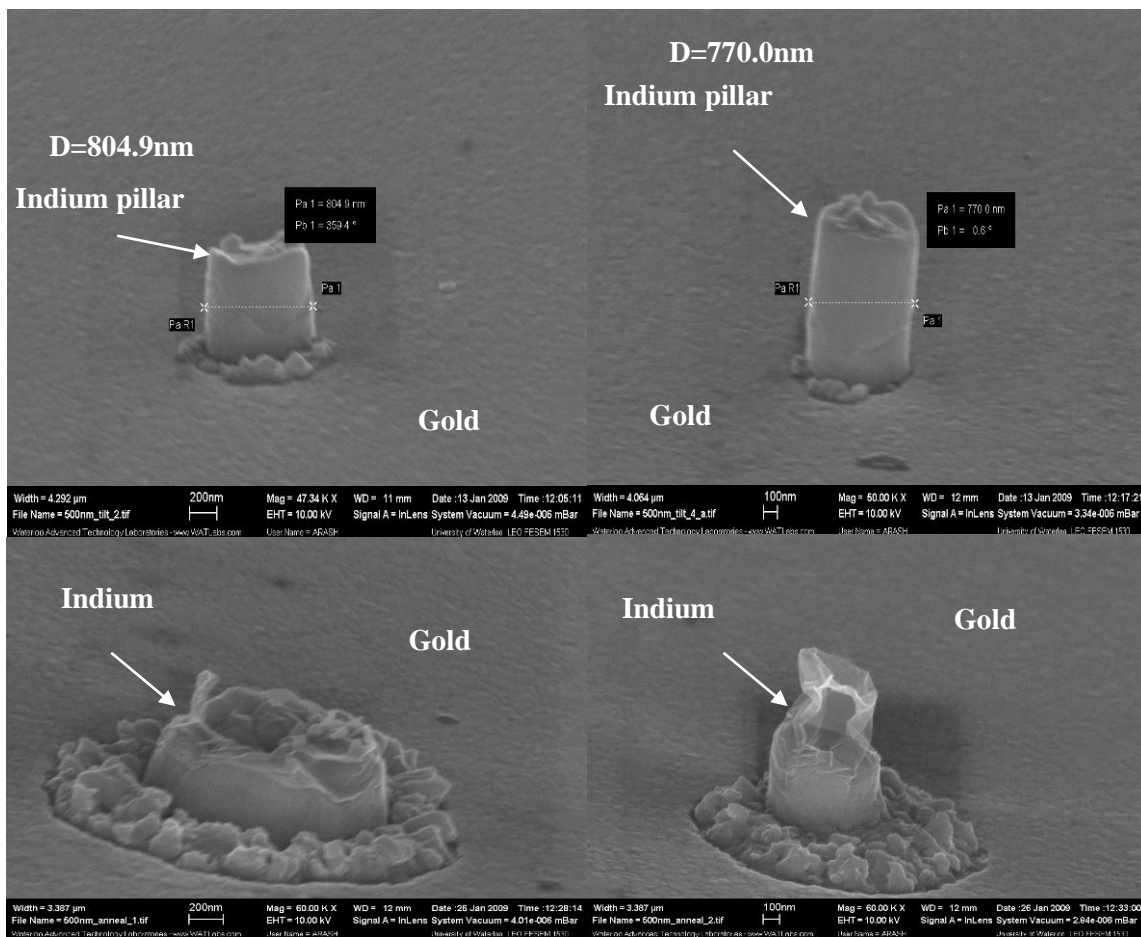


Figure 4.16 SEM image of plated 250 nm micro-mold chip using potentiostat by applying 0.2 second 10.4 mA /cm² and 10 min of 1.04 mA/ cm² current density.

As shown in Figure 4.16, using the potentiostat did not improve the formation of the indium pillars; thus, conventional DC plating was used again. A current density of 10.04 mA/cm² was applied for 3.5 seconds in order to achieve deposition nucleation, as illustrated in Figure 4.16. Applying this wave form has improved the formation of the pillars, as demonstrated in Figure 4.17.

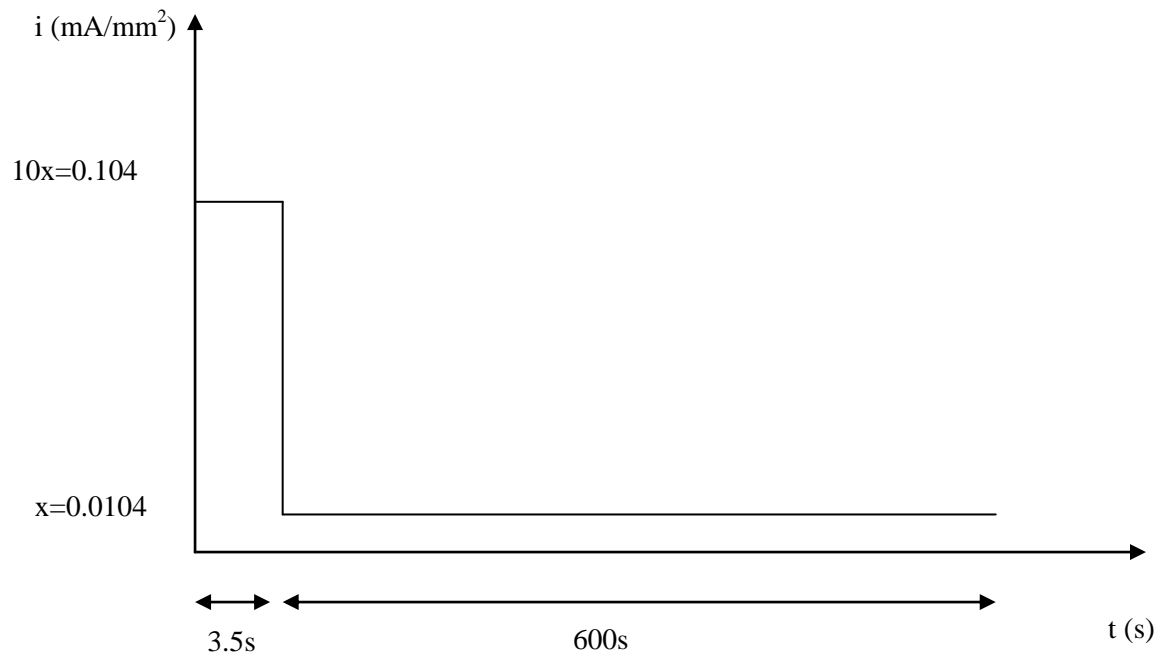


Figure 4.17 The applied wave form using Dc Power supply, current density mA /mm² vs. time(s).

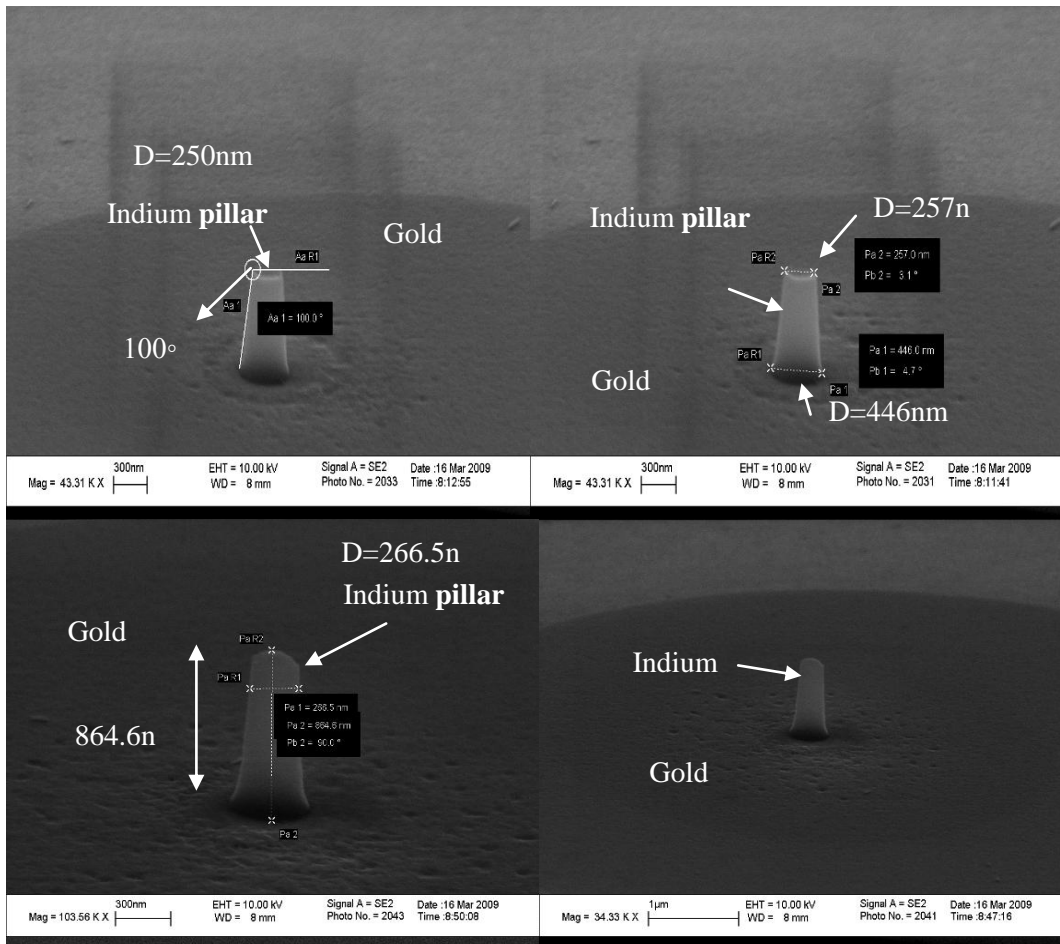


Figure 4.18 SEM images of 250 nm pillars using Dc Power supply with 3.5 second 10.4 mA/cm² current density and 10 min of 1.04 mA/cm² current density.

4.5 Oxygen Plasma Etch

Having processed E-beam micro-mold chips, oxygen plasma was applied to the E-beam micro-mold chips to remove the PMMA residue from the gold surfaces and improve the quality of plating.

To estimate the proper etching rate, the PMMA was spin coated at various speeds on dummy gold chips to achieve various thickness layers of PMMA. The PMMA samples were then

etched by applying oxygen plasma with different amount of RIE, an ICP, and pressure. Correspondingly, the condition that supplied an appropriate etching was chosen. Table 4.1 illustrates the applied condition and resultant etch rate of PMMA. The favored condition was applying 20 watts, RIE 0 watts, ICP and 102mtorr of pressure, and 40 sccm oxygen flow.

Under the aforementioned conditions, an etching rate of 1.6667 nm /sec was calculated to be reasonable for etching. The total applied time for etching was 15 seconds for 250 nm-E-beam micro-molds.

Table 4.1 PMMA etching rates corresponding to the applied etching condition, units of pressure is mTorr, RIE power is Watt, ICP Power is Watt and oxygen flow is sccm.

Set Pressure	Pressure Read	RIE Power	RIE Read	RIE Ref	ICP Power	ICP Read	ICP Ref	Oxygen Flow	Oxygen Read	Rate (nm/s)
22	19~20	50	52	2	0	1	2	40	39	5.988456
22	19~20	25	26~27	3	25	26~27	2	40	39	5.3663
22	19~20	10	10	3	20	21~22	2~3	40	39	1.95448
22	19~20	20	22	2	0	1	2	40	39	1.6667
102	99~100	50	52	4	0	1	2	40	39	6.61187
102	99~100	20	22	1	0	2	1~2	40	39	1.6667

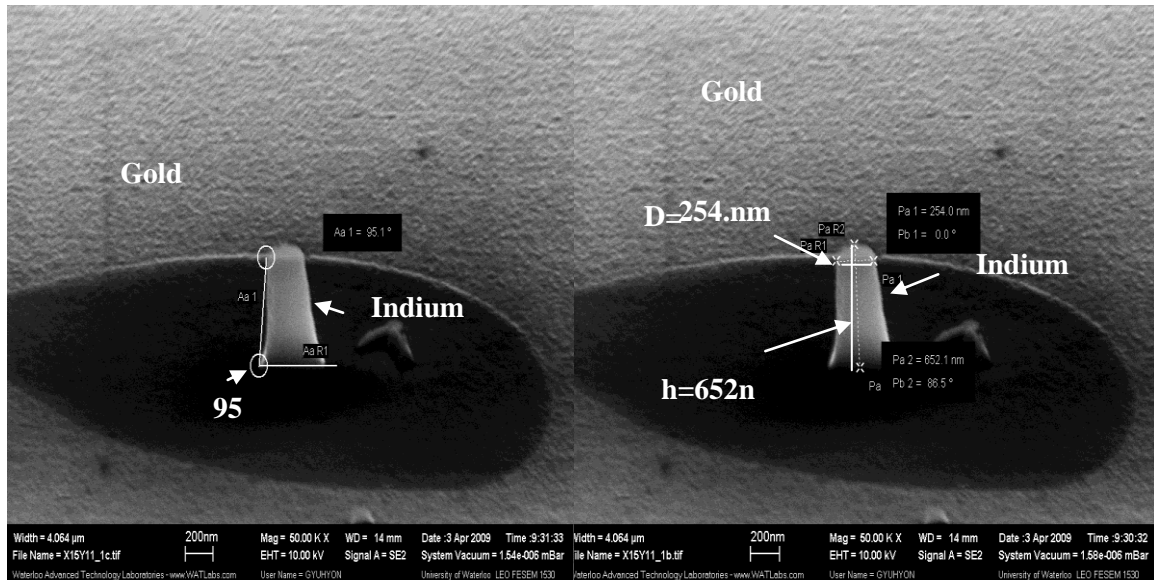


Figure 4.19 SEM images of 250 nm pillars using Dc Power supply with 3.5 second 10.4 mA/cm² current density and 10 min of 1.04 mA /cm² current density and oxygen plasma etch

Chapter 5

Summary

In the present research, a process was developed for fabricating submicron-scale indium samples for use in compression tests. The FIB was used during the process to mill the pillar samples to the desired diameter. However, the low melting point of indium limited its application for fabricating the sub-micron pillars. As a result, an alternative technique known as micro-lithography was used for fabrication. As the fabrication of finer-diameter pillars required a higher resolution patterning, E-beam lithography was employed. Versatile micro fabrication techniques were applied during the micro-mold fabrication process in order to improve the quality of features such as side wall straightness and smoothness. Pulse plating was applied for growing indium pillars; however, the result was not favorable over DC plating. The pillar was characterized by SEM and it can be seen that fabricated pillars satisfy the criteria of performing the compression test.

5.1 Recommendations

The following recommendations are made for future work:

1. Developing the E-beam lithography techniques to fabricate sub-100 nm diameter indium pillars.
2. Manufacture different grain sizes pillar samples by annealing them or improving the plating process to grow finer grains.
3. Test the creep relaxation behaviours of sub-micron pillars using the compression test to verify if the indium mechanical behavior deviates from the bulk.
4. Depositing other materials, such as cobalt and nickel, in the micro-mold chips via electroplating to create sub-micron pillar samples for compression test.

REFERENCES

- [1] Dieter, G. E. 1988. Mechanical metallurgy. 6th ed. New York: McGraw-Hill.
- [2] Courtney, Thomas H. 1990. Mechanical behavior of materials. New York; Montreal: McGraw-Hill.
- [3] Shackelford, James F. 2005. Introduction to materials science for engineers. 6th ed. Upper Saddle River, NJ: Pearson Education Inc.
- [4] Nix, William D., and Huajian Gao. 1998. Indentation size effects in crystalline materials: A law for strain gradient plasticity. *Journal of the Mechanics and Physics of Solids* 46, (3) (3): 411-25.
- [5] Ma, Q., Clarke. D.R., 1995. Size-Dependent Hardness Of Silver Single-Crystals. *Journal Of Materials Research*, 10 (4), 853-863
- [6] Poole, W. J., M. F. Ashby, and N. A. Fleck. 1996. Micro-hardness of annealed and work-hardened copper polycrystals. *Scripta Materialia* 34, (4, pp. 559-564): February.
- [7] Gerberich, W. W., N. I. Tymiak, J. C. Grunlan, M. F. Horstemeyer, and M. I. Baskes. 2002. Interpretations of indentation size effects. *Journal of Applied Mechanics* 69, (4): 433 (10) - 443.
- [8] Atkinson, M. 1995. Further analysis of the size effect in indentation hardness tests of some metals. *Journal of Materials Research* 10, (11) (11): 2908-15.
- [9] Penn state Innovation Report: "Tiny Tools Carve Glass." Report 2004; 35711.

- [10] Fleck, N. A., G. M. Muller, M. F. Ashby, and J. W. Hutchinson. 1994. Strain gradient plasticity: Theory and experiment. *Acta Metallurgica Et Materialia* 42, (2) (02): 475-87.
- [11] Voskerician, Gabriela(1), Matthew S. (1) Shive, Rebecca S. (2) Shawgo, Horst von(3) Recum, James M. (1) Anderson, Michael J. (2) Cima, and Robert(4) Langer. 2003. Biocompatibility and biofouling of MEMS drug delivery devices. *Biomaterials* 24, (11): 1959-67.
- [12] McAllister, D. V., M. G. Allen, and M. R. Prausnitz. 2000. Microfabricated microneedles for gene and drug delivery. *Annual Review of Biomedical Engineering* 2, : 289-313.
- [13] Huynh, Wendy U., Janke J. Dittmer, and A. Paul Alivisatos. 2002. Hybrid nanorod-polymer solar cells. *Science* 295, (5564) (March 29): 2425-7.
- [14] Tabor, D. 1951. *The hardness of metals*. Oxford, London; UK: Clarendon Press.
- [15] Pethica, J. B., R. Hutchings, and W. C. Oliver. 1983. Hardness measurement at penetration depths as small as 20 nm. *Philosophical Magazine A: Physics of Condensed Matter* 48, (4): 593-606.
- [16] Doucet, L., and G. Carlotti. 1995. Elastic properties of silicate glass and spin-on glass thin films. Paper presented at Proceedings of the 1994 MRS Fall Meeting, start date 19941128-enddate 19941201.
- [17] Atkins, A. G., A. Silvero, and D. Tabor. 1966. Indentation hardness and the creep of solids. *Inst Metals J* 94, (1) (Nov.): 369-78.
- [18] Mayo, M. J., and W. D. Nix. 1988. A micro-indentation study of super plasticity in Pb, Sn, and Sn-38 wt% pb. *Acta Metallurgica* 36, (8, pp. 2183-2192): August.

[19] Lucas, B. N., W. C. Oliver, G. M. Pharr, and J. -L Loubet. 1996. Time dependent deformation during indentation testing. Paper presented at Materials Research Society Symposium - Proceedings, vol. 436, 1996; Proceedings of the 1996 MRS Spring Meeting, start date 19960408-enddate 19960412.

[20] Baker, S. P., W. D. Nix, and T. W. Jr Barbee. 1992. Time-dependent deformation in room-temperature indentation experiments using a nanoindenter. Paper presented at Thin Films: Stresses and Mechanical Properties. III; Boston, Massachusetts; USA; 2-5 Dec. 1991; Thin Films: Stresses and Mechanical Properties. III, Boston, Massachusetts; USA.

[21] Yoder, K. B., D. S. Stone, J. C. Lin, and R. A. Hoffman. 1995. Indentation creep of molybdenum: Comparison between thin film and bulk material. Paper presented at Thin Films: Stresses and Mechanical Properties V; Boston, MA; USA; 28 Nov.-2 Dec. 1994; Thin Films: Stresses and Mechanical Properties V, Boston, MA; USA.

[22] Chu, S .N. G and Li, J .C .M .1977. Impression creep, new creep tests *J. Mater. Sci.* 12 2200–8.

[23] Chu, S. N. G., and J. C. M. Li. 1979. Impression creep of β -tin single crystals. *Materials Science and Engineering* 39, (1, pp. 1-10): July.

[24] Feng, G., and A. H. W. Ngan. 2001. Creep and strain burst in indium and aluminum during nanoindentation. *Scripta Materialia* 45, (8, pp. 971-976): October.

[25] Lucas, B. N., and W. C. Oliver. 1995. Time dependent indentation testing at non-ambient temperatures utilizing the high temperature mechanical properties microprobe. Paper presented at Proceedings of the 1994 MRS Fall Meeting, start date 19941128-enddate 19941201.

- [26] Syed Asif, S. A., and J. B. Pethica. 1997. Nanoindentation creep of single-crystal tungsten and gallium arsenide. *Philosophical Magazine A (Physics of Condensed Matter: Structure 76*, (6) (12): 1105-18.
- [27] Alfantazi, A. M., and R. R. Moskalyk. 2003. Processing of indium: A review. *Minerals Engineering* 16, (8): 687-94.
- [28] Indium Corporation, solder and solder paste. Retrieved Feb 20, 2008, from Web site: <http://www.indium.com/>
- [29] Swadener, J.G., E.P. George, and G.M. Pharr, 2002. The correlation of the indentation size effect measured with indenters of various shapes. *Journal of the Mechanics and Physics of Solids*, 50:681:694.
- [30] Ashby, M. F. (1). 1970. The deformation of plastically non-homogeneous materials. *Philosophical Magazine* 21, (170) (02): 399-424.
- [31] Page, T. F., W. C. Oliver, and C. J. McHargue. 1992. The deformation behavior of ceramic crystals subjected to very low load (nano) indentations. *Journal of Materials Research* 7, (2) (02): 450-73.
- [32] Gerberich, W. W., N. I. Tymiak, J. C. Grunlan, M. F. Horstemeyer, and M. I. Baskes. 2002. Interpretations of indentation size effects. *Journal of Applied Mechanics* 69, (4): 433(10) - 443.
- [33] Mann, A. B., and J. B. Pethica. 1996. Dislocation nucleation and multiplication during nanoindentation testing. Paper presented at Materials Research Society Symposium-Proceedings, vol. 436, 1996; Proceedings of the 1996 MRS Spring Meeting, start date 19960408-enddate 19960412.

- [34] Corcoran, S. G. (1), R. J. (1) Colton, E. T. Lilleodden, and W. W. Gerberich. 1997. Anomalous plastic deformation at surfaces: Nanoindentation of gold single crystals. *Physical Review B (Condensed Matter)* 55, (24) (06): R16057-60.
- [35] Jarausch, K. F., J. D. Kiely, J. E. Houston, and P. E. Russell. 2000. Defect-dependent elasticity: Nanoindentation as a probe of stress state. *Journal of Materials Research* 15, (8): 1693-701.
- [36] Suresh, S., T. G. Nieh, and B. W. Choi -. 1999. Nano-indentation of copper thin films on silicon substrates. *Scripta Materialia (USA)* 41, (9) (8 Oct.): 951-7.
- [37] Van der Merwe, J. H., and F. C. Frank. 1949. Misfitting monolayers. *Proceedings of the Physical Society. Section A* 62, (May): 315-6.
- [38] Matthews, J. W. (1), and A. E. (1) Blakeslee. 1975. Defects in epitaxial multilayers: II. Dislocation pile-ups, threading dislocations, slip lines and cracks. *Journal of Crystal Growth* 29, (3): 273-80.
- [39] Matthews, J. W., and A. E. Blakeslee. 1974. Defects in epitaxial multilayers. *Journal of Crystal Growth* 27: 118-25.
- [40] Freund, L. B. (1). 1987. The stability of a dislocation threading a strained layer on a substrate. *Transactions of the ASME. Journal of Applied Mechanics* 54, (3) (09): 553-7.
- [41] Nix, W. D. 1998. Yielding and strain hardening of thin metal films on substrates. Paper presented at Scripta Materialia, vol.39, no.4-5, pp.545-554, 4 Aug. 1998; Defects in Crystals: A Symposium Honoring the Contributions of John P Hirth. Held at the TMS Annual Meeting, 16-19 Feb. 1998, San Antonio, TX, USA. TMS,

- [42] Greer, J. R. (1), and W. D. (1) Nix. 2005. Size dependence of mechanical properties of gold at the sub-micron scale. *Applied Physics A (Materials Science Processing)* A80, (8) (05): 1625
- [43] Greer, J. R., W. C. Oliver, and W. D. Nix. 2005. Size dependence of mechanical properties of gold at the micron scale in the absence of strain gradients. *Acta Materialia* 53, (6): 1821-30.
- [44] Greer, J. R., W. C. Oliver, and W. D. Nix. 2006. Corrigendum to "size dependence in mechanical properties of gold at the micron scale in the absence of strain gradients" [acta mater 53 (6) (2005) 1821-1830]. *Acta Materialia* 54, (6) (Apr): 1705.
- [45] Greer, J. R. (1), and W. D. (1) Nix. 2006. Nanoscale gold pillars strengthened through dislocation starvation. *Physical Review B (Condensed Matter and Materials Physics)* 73, (24) (06): 245410, 2451-6.
- [46] Uchic, M. D. (1), D. M. (1) Dimiduk, J. N. Florando, and W. D. Nix. 2004. Sample dimensions influence strength and crystal plasticity. *Science* 305, (5686) (08): 986-9.
- [47] Uchic, M. D. (1), and D. M. (1) Dimiduk. 2005. A methodology to investigate size scale effects in crystalline plasticity using uniaxial compression testing. *Materials Science & Engineering A (Structural Materials: Properties)* 400-401, (07): 268-78.
- [48] Dimiduk, D. M., M. D. Uchic, and T. A. Parthasarathy. 2005. Size-affected single-slip behavior of pure nickel microcrystals. *Acta Materialia* 53, (15) (09): 4065-77.
- [49] Dimiduk, D. M., C. Woodward, R. Lesar, and M. D. Uchic. 2006. Scale-free intermittent flow in crystal plasticity. *Science* 312, (5777) (05): 1188-90.
- [50] Volkert, C. A., and E. T. Lilleodden. 2006. Size effects in the deformation of sub-micron au columns. *Philosophical Magazine* 86, (33-35) (11): 5567-79.

- [51] Brinckmann, S., Ju-Young Kim, and J. R. Greer. 2008. Fundamental differences in mechanical behavior between two types of crystals at the nano scale. *Physical Review Letters* 100, (15) (04): 155502, 1551-4.
- [52] Shan, Z. W., J. Li, Y. Q. Cheng, A. M. Minor, S. A. S. Asif, O. L. Warren, and E. Ma. 2008. Plastic flow and failure resistance of metallic glass: Insight from in situ compression of nanopillars.
- [53] Van Der Biest, O., and J. Van Der Planken. 1973. The plastic deformation of indium single crystals. *Acta Metallurgica* 21, (12, pp. 1629-1639): December..
- [54] Giannuzzi, L. A. and Stevie, F. A. 2005, "Introduction to Focused Ion Beams: Instrumentation, Theory, Techniques and Practice", Springer, New York.
- [55] Andricacos, P. C., and M. Datta. 1987. [Theory and practice of pulse plating (book review)]. *Plating and Surface Finishing* 74, (March): 80-1.
- [56] Tang, Peter Torben, Henrik Dylmer, and Per Mo slashedlller. *Electroplating method of forming platings of nickel*. Patent USA 6036833.
- [57] Jernstedt, G. W. 1947. PR plating, a new tool for electroplaters. *Westinghouse Engineer* 7, (May): 89-92.
- [58] Sverdlov, Y., Y. Rosenberg, Y. I. Rozenberg, R. Zmood, R. Erlich, S. Natan, and Y. Shacham-Diamand. 2004. The electrodeposition of cobalt-nickel-iron high aspect ratio thick film structures for magnetic MEMS applications. *Microelectronic Engineering* 76, (1-4): 258-65.

- [59] Gomez, E., E. Pellicer, and E. Valles. 2005. Electrodeposition of cobalt based alloys for MEMS applications. *Transactions of the Institute of Metal Finishing* 83, (5): 248-54.
- [60] Gomez, E., E. Pellicer, and E. Valles. 2005. Electrodeposition of cobalt based alloys for MEMS applications. *Transactions of the Institute of Metal Finishing* 83, (5): 248-54
- [61] Brener, A. 1965. Electrodeposition of alloys, past, present, and future. *Plating* 52, (12) (Dec.): 1249-57.
- [62] Bard.A.J., and Faulkner.L.R. 2001. *Electrochemical Methods: Fundamentals and Applications*. 2nd ed., John Wiley & Sons, New York.
- [63] Kim, J., H. Schoeller, J. Cho, and S. Park. 2008. Effect of oxidation on indium solders ability.
- [64] Kern, W., and Puotinen D. A. 1970. Cleaning solutions based on hydrogen peroxide for use in silicon semiconductor technology, *RCA Review*, vol. 31, 187.
- [65] MicroChem Corporation,. Data sheet SU-8 2-25. Retrieved May 20, 2008, from Photoresistes formulations SU-8 2-25
Website:http://mems.gatech.edu/msmawebiste/members/processes/processes_files/SU8/Data%20Sheet%202-25.pdf
- [66] MicroChem Corporation, SU-8-material data sheet. Retrieved July 6, 2008, from Material Saftey Data Sheet Web site: <http://www.bioeng.nus.edu.sg/biofluids/intranet/MSDS/su-8-dev.pdf>
- [67] MicroChem Corporation, Newton, Ma, PMMA product information sheet. Retrieved Sep, 2008, from PMMA &Copolymer Web site: “PMMA product information sheet “MicroChem

Corporation, Newton, Ma, [online]

Available:http://www.microchem.com/products/pdf/PMMA_Data_Sheet.pdf.

[68] Popov, K. I., M. D. Maksimović, B. M. Ocokoljić, and B. J. Lazarević. 1980. Fundamental aspects of pulsating current metal electrodeposition I: The effect of the pulsating current on the surface roughness and the porosity of metal deposits. *Surface Technology* 11, (2): 99-109.

[69] Chuang, Y. J, F.G Tseng, and W. -K Lin. 2002. Reduction of diffraction effect of UV exposure on SU-8 negative thick photoresist by air gap elimination. *Microsystem Technologies* 8, (4-5): 308-13.

Appendix A

Best Known Method for Fabricating 0.25 μ m Pillars

1. Cleaning Silicon wafers (Section 3.2.3.1, Page 46)

- Dice the samples to 2.54 x 2.54 cm
- Solution: 5:1:1 H₂O/H₂O₂/NH₄OH solution at 75°C
- Time: submerge the wafers for 15 minutes
- Solution: 700ml of DI water at 80-90 °C hot water
- Time: submerge the wafer for 15 minutes in hot water
- Wash the wafer under running DI water and dry with nitrogen gas

2. Cr/Au Deposition (Section 3.2.3.2, Page 47)

- Instrument: Nanochrome™ DC sputtering system (Intelvac, Canada)
- Vacuum chamber for 45 minutes to reach 3.26E-6 Torr pressure
- Chamber temperature: 10.9°K
- Set chromium thickness: 40nm
- Set gold thickness: 60nm

3. AZ Photo Resist Coating (Section 3.2.3.3.2.2, Page 67)

- Photo resist type: AZ 3330 positive photo resist, (AZ Electronic Materials, USA)
- Instrument: Ws-400A-6Npp/Lit Spin coater (Laurell Technologies Corporation, USA)
- Spin speed: 4000 rpm
- Acceleration rate: 1215 ramp/sec
- Time: 45 seconds
- Soft-baked at 90°C for 5 minutes on EMS Precision Electronic Hot Plate

4. Patterning with Emulsion Mask (Section 3.2.3.3.2.2, Page 70)

- Instrument: Oriel mask aligner (Newport Corporation, USA)
- Power density: 41mW/Cm²
- Expose time: 20 second
- Post exposure bake at 110°C for 1 min on EMS Precision Electronic Hot Plate

5. Developing AZ–Photo Resist (Section 3.2.3.3.2.2, Page 70)

- Developer: AZ MIF 300 developer (AZ Electronic Materials, USA)
- Developing time 80-90 seconds
- Submerge in DI water for 5-10 seconds

6. Gold Etch (Section 3.2.3.3.2.2, Page 70)

- Etchant: Gold etchant type TFA (Transene Company, USA)
- Time: ~10 second.
- Temperature: room temperature
- Submerge in DI water for 5-10 seconds

7. Chromium Etch (Section 3.2.3.3.2.2, Page 70)

- Chromium Etchant Type 1020 (Transene Company, USA)
- Time:~ 20-25 seconds
- Temperature: room temperature
- Submerge in DI water for 5-10 seconds

8. Stripping AZ resist (Section 3.2.3.3.2.2, Page 70)

- AZ stripper: Kwik stripper (AZ Electronic Materials, USA)
- Time: ~15 minutes
- Temperature: 60°C
- DI water washing / nitrogen blow drying

9. Oxygen Plasma Etch the Wafers (Section 3.2.3.3.2.3, Page 70)

- Instrument: Trion Orion Plasma-Enhance Chemical Vapor Deposition (PECVD) System (Trion Technology, USA)
- Conditions:

Table 5.1 Oxygen etch condition for removing AZ residues

Set P (mT)	Read P(mT)	RIE (W)	RIE Read(w)	RIE Ref	ICP (W)	ICP Read(w)	ICP Ref	Oxygen Flow(sccm)
20	19~20	50	52	4	50	52	4	40

- Time: 3 minutes
- Tape the controlling area surface

10. PMMA Coating (Section 3.2.3.3.2.3, Page 70)

- Photo resists: Poly methyl methacrylate (PMMA) 950KMW A4 (MicroChem Corporation, USA)
- Spin coating the second layer of PMMA, Speed: 500rpm for 3 seconds, speed ramp to 1500 rpm and hold for 1 minute

- Soft bake at 50°C for 10 minutes on vacuum hotplate
- Spin coating second layer of PMMA, Speed: 500 rpm for 3 seconds, speed ramp to 1500 rpm and hold for 1 minute
- Soft bake at 50°C for 10 minutes on vacuum hotplate
- PMMA Thickness: 750nm

11. E-Beam Lithography (Section 3.2.3.3.2.4, Page 71)

- Applied dosage for fabricating the 250 nm pillar site in 15 x15 regions, was 50%-254% of 500 mC /cm² with increment of 0.9% in the serpentine pattern. As it is demonstrated in Figure 4.19.

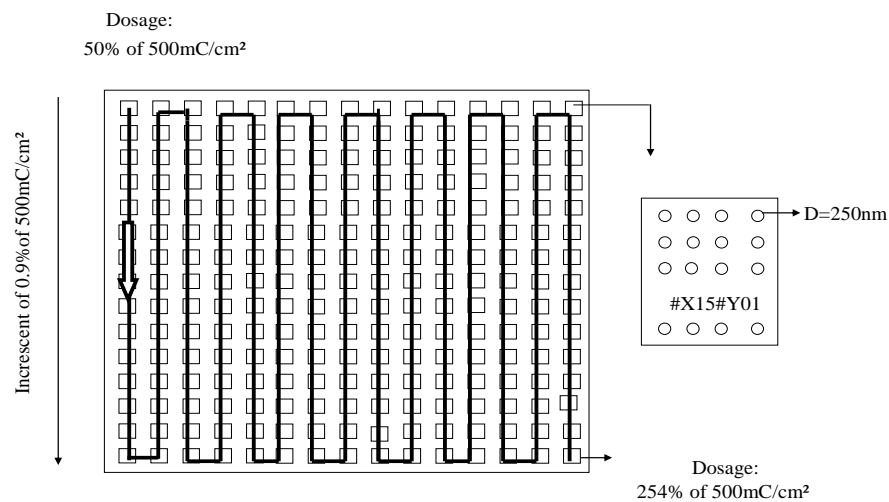


Figure 5.1 E-Beam write map with the applied dosage in each section.

- Remove tapes
- Wafers baked at 180 °C for 90 seconds

12. Developing PMMA (Section 3.2.3.3.2.4, Page 72)

- PMMA was developed in three steps: while the wafers were spun at 500 rpm, the resist was developed in 1:3 MIBK:IPA in an atomized spray developer for 90 seconds, rinsed with IPA spray for 60 seconds, and then blow dried with nitrogen gas

13. Cleaning the Controlling Surface (Section 3.2.3.3.2.4, Page 74)

- Use a cotton swab to clean the edges and eliminate any tape residue.
- First, apply acetone on a cotton swab and clean all four controlling surfaces.
- Second, apply isopropyl alcohol on cotton swab and clean all four controlling surfaces

14. Oxygen Plasma Etch (Section 3.2.3.3.2.5, Page 75)

- Instrument: Trion Orion Plasma-Enhance Chemical Vapor Deposition (PECVD) System (Trion Technology, USA)
- Conditions:

Table 5.2 Oxygen Etch condition for removing PMMA residues

Set P (mT)	Read P(mT)	RIE (W)	RIE Read(w)	RIE Ref(W)	ICP (W)	ICP Read(W)	ICP Ref(W)	Oxygen Flow(sccm)
102	100	20	22	1	0	1	2	40

- Time: 15 seconds

15. Electroplating (Section 3.2.3.3.2.6, Page 77)

- Solution: 200 ml Indium sulfamate solution (Indium Corporation, USA).
- Instrument: Bk Precision power supply (Test Path, USA)
- Place the indium solution beaker while the chip is inside it into a sonicator and apply sonication at least for 5 minutes
- Plating conditions:
 - Voltage: 1.56 V
 - Current density: 1.041 mA/cm²
 - Anode: indium bar size 4 cm x 15 cm
 - Cathode: micro-mold chip size 2.54 cm x 2.54 cm
 - Duration: 3.5 seconds At 10.41 mA/cm² current density
 - Duration: 8.5 minutes 1.041 mA/cm² current density
 - Deposition rate: 83 nm/minute
 - Place the sample in water for 5 minutes and then blow dry it

16. Stripping PMMA photo Resist (Section 3.2.3.3.2.7, Page 80)

- PMMA stripper: Kwik stripper (AZ Electronic Materials, CA)
- Pour solution into Petri dish and leave the samples in it for 48 hours
- Temperature: room temperature
- Pour isopropyl alcohol into a Petri dish and place the sample into it very carefully. Leave it there for at least 5 minutes.
- Remove the sample carefully and allow it to air dry.